ALMA MATER STUDIORUM – UNIVERSITA' DEGLI STUDI DI BOLOGNA

Dottorato di Ricerca in Geofisica

XXVI Ciclo

Settore Concorsuale di afferenza: 04/A4

Settore Scientifico disciplinare : Geo /10

SEISMIC SEQUENCES ANALYSIS FOR ESTIMATION OF EARTHQUAKE SOURCE PARAMETERS: CORNER FREQUENCY, STRESS DROP, AND SEISMIC MOMENT OBSERVATIONS.

Candidata
Irene Munafò

Relatore
Dr. Luca Malagnini

Coordinatore Dottorato
Prof. Michele Dragoni

Esame Finale Anno 2014

To my Grandma

Abstract

The present study has been carried out with the following objectives: i) To investigate the attributes of source parameters of local and regional earthquakes; ii) To estimate, as accurately as possible, M_0, f_c, $\Delta\sigma$ and their standard errors to infer their relationship with source size; iii) To quantify high-frequency earthquake ground motion and to study the source scaling. This work is based on observational data of micro, small and moderate -earthquakes for three selected seismic sequences, namely Parkfield (CA, USA), Maule (Chile) and Ferrara (Italy).

For the Parkfield seismic sequence (CA), a data set of 757 (42 clusters) repeating micro-earthquakes ($0 \leq M_W \leq 2$), collected using borehole High Resolution Seismic Network (*HRSN*), have been analyzed and interpreted. We used the coda methodology to compute spectral ratios to obtain accurate values of f_c, $\Delta\sigma$, and M_0 for three target clusters (San Francisco, Los Angeles, and Hawaii) of our data. We also performed a general regression on peak ground velocities to obtain reliable seismic spectra of all earthquakes.

For the Maule seismic sequence, a data set of 172 aftershocks of the 2010 M_W 8.8 earthquake ($3.7 \leq M_W \leq 6.2$), recorded by more than 100 temporary broadband stations, have been analyzed and interpreted to quantify high-frequency earthquake ground motion in this subduction zone. We completely calibrated the excitation and attenuation of the ground motion in Central Chile.

For the Ferrara sequence, we calculated moment tensor solutions for 20 events from M_W 5.63 (the largest main event occurred on May 20 2012), down to M_W 3.2 by a 1-D velocity model for the crust beneath the Pianura Padana, using all the geophysical and geological information available for the area. The PADANIA model allowed a numerical study on the characteristics of the ground motion in the thick sediments of the flood plain.

Acknowledgements

I am extremely thankful to my advisor, Dr. Luca Malagnini, for his guidance and supervision from the very early stage of this research as well as giving me extraordinary experiences throughout the work. Above all and the most need, he provided me encouragement and support in various ways. His truly scientist intuition has made him as a constant oasis of ideas and passion in science, which inspire and enrich my growth as a student, a researcher and a scientist want to be. I am indebted to him more than he knows.

Special thank goes to Prof. Douglas Dreger, for the stimulating discussion and for supportive during my time at the Berkeley Seismological Laboratory, University of California, Berkeley. I want to thank Prof. Robert B. Herrmann for his constructive comments and suggestions that helped to improve this thesis. I thank Dr. Kevin Mayeda for some useful discussions. I thank also Dr. Seung Hoon Yoo for providing me his code and help me during my work.

During these three years of my Ph.D studies, I had the opportunity to met very special collaborators. I express my gratitude to all my INGV collegues who supported me in any aspect during the completation of this project. I am also grateful to other Ph.D student and researcher who shared study and laughter in the "Pollaio": Leda, Luigi, Riccardo, Debora, Michele Mariagrazia, Matteo, Giovanna, Javier, Anita and Catalina.

Six months of this research were spent in the University of California, Department of Earth and Planetary Science, Berkeley Seismological Laboratory (BSL). Thank to all my collegues of Berkeley for making me feel at home.

I wish to express my love and gratitude to all my family and friends. I'd particularly like to thank my mother, my brother, my grandma and my aunt. They had more faith in me than could ever be justified by logical argument. This page wouldn't be sufficient to mention their enormous support, encouragement and especially invaluable untiring patience displayed.

Lastly, I wish to thank all those whose names have not figured above but have helped me directly or indirectly during the course of my research work.

Table of contents

Table of contents

I.1 Preamble

Earthquake source parameters can give information on the source properties of individual shocks. The seismic waves produced by the earthquakes are used to study the structure and composition of the earth's interior, and the properties of earthquake source. However, to understand how the wave field is radiated from the earthquake source it is important to deduce the properties of the earthquake source as the resolution of the earth's structure requires precise knowledge of the parameters of earthquake source (Shearer, 1999). Our understanding about the occurrence of earthquakes has largely developed in last about 50 years. To understand the state of stress in the earth's crust leading to earthquakes, it is important to study the properties of earthquakes from the measurements of amplitudes and frequencies of the seismic waves recorded on seismograms. Usually the sources of small to moderate earthquakes are inaccessible to direct observation and our understanding about their source properties primarily based on the records of the seismic waves. As shown graphically in Figure I.1, at source the radiated wave-field in the form of a pulse is modified by geometrical spreading *g(r)*, attenuation, scattering, site effects and the response of the instrument (Lenhardt, 2006).

Major part of seismology deals with extracting information on the above factors from the seismogram by employing various types of techniques. The instrument response is either known or can be computed. The observed spectra after removing the instrument response are decomposed to study the properties of earthquake source, path and site.

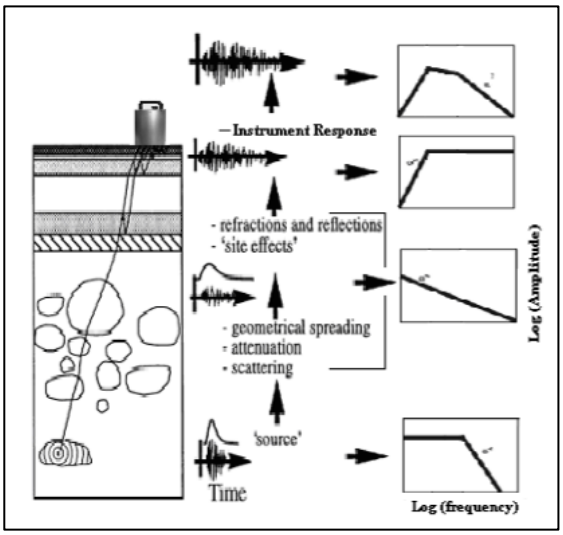

Figure I.1: A schematic representation of an earthquake in time and frequency domain at source and the effects -path, site and instrument that modifies its shapes (modified after Lenhardt, 2006).

In the early 1930's Richter introduced the magnitude parameter to measure the size of an earthquake using the amplitude of seismic waves. The seminal work of Aki (1967) and Brune (1970) laid a strong foundation to develop the scaling laws and to compute the source parameters using the spectra of seismic waves. These parameters provide a great deal of information about the properties of the earthquake source, and find a large number of applications in Seismology. Some of the important applications include: understanding earthquake rupture processes and quantifying the excitation of high frequency ground motion produced by large earthquakes.

I.2 Objectives of the Study

In view of above considerations the present study is an attempt to estimate and interpret source parameters from the digital data for three selected sequences: i) Parkfield, CA, USA; ii) Maule, Chile; and iii) Ferrara, Italy. The selection of these seismic sequences is guided by both the availability of seismological data and their tectonic settings. The study has been carried out with the following objectives:

1. To investigate the attributes of source parameters of local and regional earthquakes;
2. To estimate, in a manner as accurate, M_0, f_c, $\Delta\sigma$ and their standard errors to infer their relationship with source size;
3. To quantify high-frequency earthquake ground motion and to study the source scaling.

For the Parkfield seismic sequence we investigate source parameters and scaling of 757 repeating micro-earthquakes occurring on the Parkfield segment of the San Andreas Fault (SAF) taking into account model (epistemic) variability due to method. We will compute source corner frequency and stress drop using multi-taper spectral analysis of P and S waves (Yoo et al., 2012), coda method (Mayeda et al., 2007) and inversion for source, path and site (e.g., Malagnini et al., 2007) using data from the borehole High Resolution Seismic Network (HRSN).

The results of this analysis will be compared to estimates obtained from the Nadeau and Johnson (1998) asperity loading model, as well as finite-source models of earthquakes from M 1.8 to 6.0 (Dreger et al., 2007; Uchide and Ide, 2010). The aim of this work is to investigate the scaling of Parkfield seismicity where studies have suggested self-similar (Baltay et al., 2010), and non- self-similar scaling (Nadeau and Johnson, 1998). We also calculated an accurate moment magnitudes

for most of the 757 events of our data set, between $M_W \sim 0$ and $M_W \sim 1.9$. The results of such analyses give us insights into the underlying mechanics of faulting and the earthquake process.

For the Maule seismic sequence, a data set of 172 aftershocks of the 2010 M_W 8.8 earthquake ($3.7 \leq M_W \leq 6.2$), have been analyzed and interpreted. They were recorded by more than 100 temporary broadband stations, deployed between March 2010 and January 2011. All of the earthquakes occurred off the west coast of Chile at or near the plate interface, typically in the depth range of 20-35 km. This data set provided a unique opportunity to quantify high-frequency earthquake ground motion in a subduction zone due to the quality and quantity of observations in the frequency and distance ranges of 0.2-30 Hz and 40-500 km.

The analysis was done using a two-step modeling procedure: i) a regression was performed to characterize source duration and excitation, source-receiver distance dependence, and station site effects; ii) a point-source forward model is constructed in terms of geometrical spreading, observed duration, site effects, and source scaling, in order to match the regression results.

The outlined procedure provides the necessary point source parameters for a stochastic finite-fault modeling of the ground motions for future large earthquakes in this subduction zone. Numerous studies were published by Malagnini, Mayeda, and co-workers on all tectonic environments (normal, strike-slip, and reverse), but no data have yet been analyzed on subduction earthquakes; for this reason, the present data set will be of special interest.

For the Ferrara sequence, a total of 2100 events were located between May 19 and June 25 2012 by the INGV National Seismic Network. 80 of them (whose waveforms were gathered and used for this study) had $M_L > 3.5$. The main shock, in fact, started a complex seismic sequence, in which six more earthquakes with $M_L > 5$ struck the area.

We calculated moment tensor solutions for 20 events from M_W 5.63 (the largest main event occurred on May 20 2012), down to M_W 3.2 by a 1-D velocity model for the crust beneath the Pianura Padana, using all the geophysical and geological information available for the area. PADANIA model developed in order to perform a numerical study on the characteristics of the ground motion in the thick sediments of the flood plain.

I.3 Plan of the Thesis

Chapter II gives a brief outline of basic concept of source parameters (stress drop, moment magnitude, seismic source spectrum, seismic moment and size of the source area); moment tensor solutions; important earthquake source models and methods adopted to compute earthquake source parameters from observational data.

Chapter III contains comprehensive assessments of Parkfield earthquake source estimates.

Chapter IV contains the characteristic of high frequency ground motions in the Maule region (Chile), obtained from the aftershocks of the 2010 M_W 8.8 earthquake.

Chapter V contains the description of the 2012 Ferrara seismic sequence: regional crustal structure, earthquake sources, and seismic hazard.

Supplemental Material Chapter V contains 20 figures describing the moment tensor solutions for events of the Ferrara sequence (the foreshock, occurred on 2012/05/19 at 23:13:27, the main event, occurred on 2012/05/20 at 02:03:53, and the other 18 aftershocks of the sequence).

Appendix A contains a brief description of the Random Vibration Theory.

II.1 Introduction

Since the dawn of seismology, attempts have been made to study the attributes of earthquake source. As the earthquakes were perceived as the sudden shaking of the ground, early efforts were to locate the source of the shaking and to look for the causes that produced the shaking. After the advent of seismographs, efforts were made to locate earthquakes from the arrival times of seismic waves using primarily graphical methods.

However, after the advent of computers that allowed fast computing, several computer programs have been developed after 1960's to estimate the hypocenter parameters of an earthquake (e.g., Lienert et al., 1986). Richter (1935) gave the magnitude parameter to quantify the size of an earthquake from the measurements of amplitudes of local earthquakes recorded using a network of short period Wood Anderson seismographs in Southern California.

The latter was a major breakthrough in seismology, which allowed the ranking of earthquakes according to their size. This local magnitude scale was extended to surface wave magnitude (M_S) and body wave magnitude (m_b) to allow computing the size of the teleseismic earthquakes. However, it was not very clear as to how the amplitudes of the seismic waves vary with magnitude over a whole range of frequency bands, although some work in this direction was carried out by Berkmhemer (1962), who showed an increase in predominant period of an earthquake with increasing magnitude.

Aki (1967) developed scaling law for the seismic spectrum, marking the beginning of an important field to understand the variation of spectrum with the size of an earthquake. Brune (1970) derived an earthquake model by considering the effective stress available to accelerate the two sides of the fault. This model successfully explained the observed near- and far-field spectra of earthquakes and many researchers have been adopting this model for the last four decades, in order to compute the earthquake source parameters.

The detailed understanding and quantification of the physical processes and geometry of seismic sources is one of the ultimate goals of seismology, which is also needed for the understanding of tectonics, improving the seismic hazard assessment, or discriminating between natural and anthropogenic events. Earthquakes can be quantified with respect to various geometrical and physical parameters, such as time and location of the (initial) rupture and orientation of the fault plane and slip, fault length, rupture area, amount of slip, magnitude, seismic moment, radiated energy, stress drop, duration and time-history (complexity) of faulting, particle velocity,

acceleration of fault motion etc. It is impossible to represent this complexity with just a single number, or with just a few parameters.

There are different approaches to tackle the problem. One aims at the detailed analysis of a given event, both in the near-field and in the far-field, analyzing waveforms and spectra of various kinds of seismic waves in a broad frequency range up to the static displacement field as well as looking into macroseismic data. Such a detailed and complex investigation requires a lot of time and effort. It is feasible only for selected important events.

The second simplified approach describes the seismic source only by a limited number of parameters such as the origin time (initial rupture), location, magnitude, intensity or acceleration of observed/measured ground shaking, and fault-plane solution. Most of these parameters can easily be obtained and have the advantage of rough but quick information being given to the public, and to the concerned authorities. Furthermore, this approach provides standardized data for comprehensive earthquake catalogs, which are fundamental for other kinds of research such as earthquake statistics and seismic hazard assessment. But we need to be aware that these simplified, often purely empirical parameters can not give a full description of the true nature of a seismic source: its geometry, time history, or energy release.

II.2 Source Parameters: basic concepts

II.2.1 Stress drop

Accumulated stress acts as a fuel that provides the energy to propel earthquake faulting. Moreover, the amount of accumulated stress plays an important role in controlling the size of an earthquake. The causes of these stresses are attributed to several factors: ambient tectonic forces, uplifts, changes of the orientation of principal stresses, pore water pressure changes, impacts and intrusions. When an earthquake occurs in a stressed medium, a drop in the level of stress occurs. Therefore, in case we know the stress drop distribution due to past earthquakes, this information forms an important ingredient to model the underlying dynamic processes that drive the rupture.

As a consequence, the stress drop is one of the most important parameters that can be estimated from the spectrum of the earthquake source. Earthquakes occur when the local shear stress on a fault plane increases beyond its frictional strength. The stress drop represents the part of the stress acting along the fault surface during the faulting process producing the slip. Study of stress-

dependent material properties provides an understanding of the physical processes occurring in the source region. Such studies allows investigating the way in which material failure nucleates and spreads along a fault surface rapidly relieving stresses that had slowly accumulated due to long-term tectonic processes (Aki & Richards, 1980).

The relationship between the slip in an earthquake, its fault dimensions, and its seismic moment is closely tied to magnitude of stress released by the earthquake, or stress drop. We assume that the earthquake's slip averaged over the fault plane, $\overline{D}$, occurs on a fault with characteristic L, so the stress drop averaged over the fault is approximately

$$\Delta\sigma = \mu\overline{D}/L \tag{1}$$

For example (Eshelby, 1957), the stress drop on a circular fault with radius R is

$$\Delta\sigma = \frac{7}{16}\frac{M_0}{R^3} \tag{2}$$

This equation let us estimate the stress drop from an observed seismic moment and inferred fault dimension.

II.2.2 Seismic Moment, Seismic Source Spectrum and size of the source area

A moment of a force system is the vector product of the force with the position vector of the point of application. Two parallel forces form a couple with a definite moment. The fundamental equivalence theorem proved by Steketee (1958) stated that "a displacement field produced by the dislocation Δu on plane element δS in an elastic body equals that produced by a double couple applied at δS ". This concept has been applied in seismology to compute the seismic moment, M_0, of an earthquake because the crustal earthquakes are caused by shear fractures in the Earth's crust. Seismic moment is a scalar quantitative measure of the size and strength of a seismic shear source. For a homogeneous and isotropic medium Aki (1966) derived the following expression to compute the seismic moment of an earthquake:

$$M_0 = \mu\overline{D}A \tag{3}$$

with μ is the rigidity or shear modulus of the medium, $\bar{D}$ is the average final displacement after the rupture and A is the surface area of the rupture. The value of μ is normally taken as $3x10^{11}$dyne cm^{-2} for the crustal rocks. On the basis of reasonable average assumptions about μ and the stress drop $\Delta\sigma$ (i.e., with $\Delta\sigma/\mu$ = constant) Kanamori (1977) derives the relationship $E_S = 5\times10^{-5}\ M_0$ (in J). Its determination is now standard in the routine analysis of strong earthquakes by means of waveform inversion of long-period digital records.

In a homogeneous half-space, M_0 can be determined from the spectra of seismic waves observed at the Earth's surface by using the relationship (Keiles-Borok, 1959):

$$M_0 = \frac{4\pi d\rho v_{p,s}^3 u_0}{R_{\theta,\varphi}^{p,s}} \tag{4}$$

where d is the hypocentral distance between the event and the seismic station; ρ is the average density of the rock; $v_{p,s}$ is the velocity of the P or S waves around the source; $R_{\theta,\varphi}^{p,s}$ is a factor correcting the observed seismic amplitudes for the influence of the radiation pattern of the seismic source, which is different for P and S waves; u_0 is the the low- frequency amplitude level as derived from the seismic spectrum of P or S waves, corrected for the instrument response, wave attenuation and surface amplification.

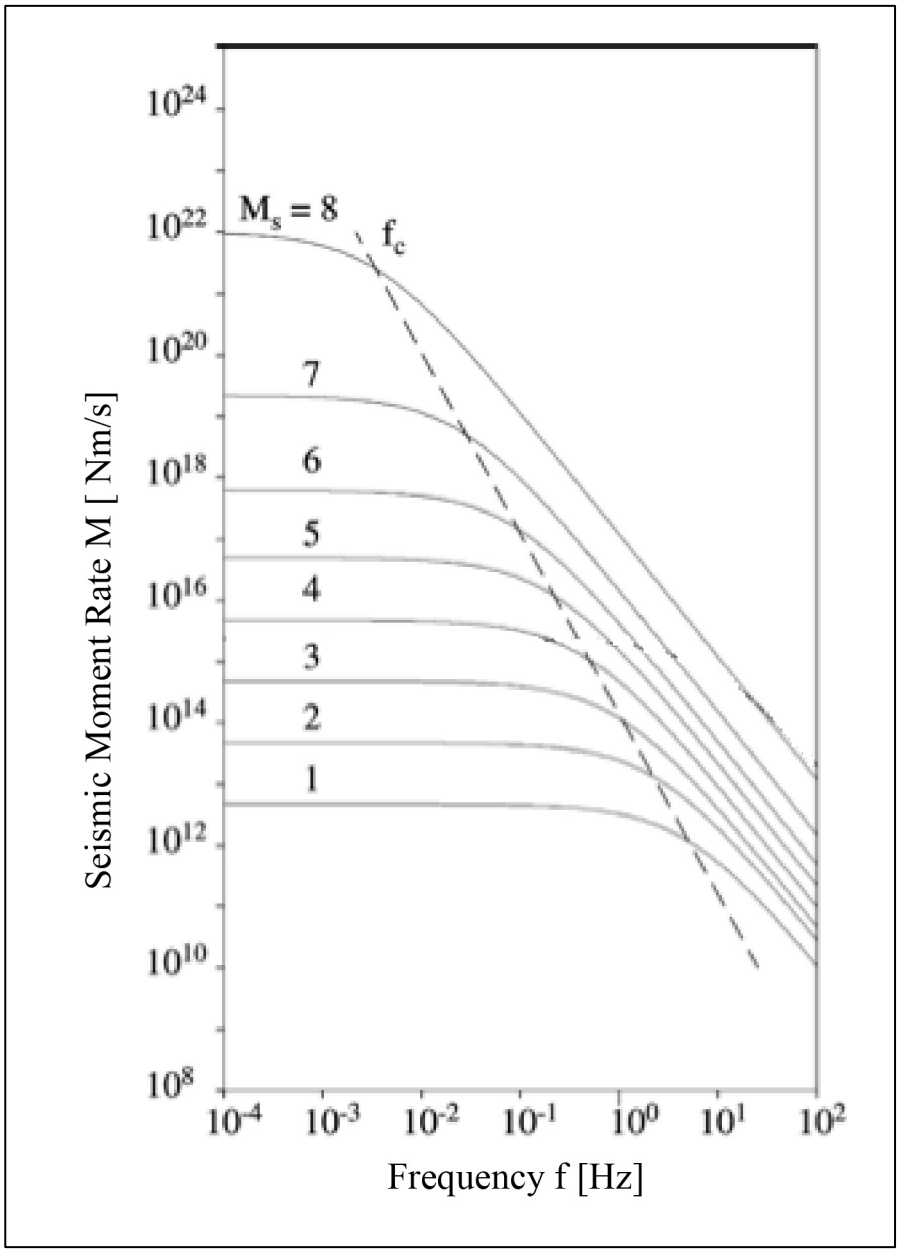

Figure II.1: Source spectra of ground displacement for a seismic shear source. Source spectrum means here the attenuation-corrected ground displacement *u(f)* or ground velocity $\dot{\boldsymbol{u}}$ *(f)* respectively, multiplied by the factor $\boldsymbol{4\pi d\rho v^3_{p,s}/R^{p,s}_{\theta,\varphi}}$. The ordinates do not relate to the frequency-dependent spectra proper but rather to the low- frequency scalar seismic moments or moment rates that correspond to the depicted spectra. The broken line (long dashes) shows the increase of corner frequency f_c with decreasing seismic moment of the event**.** Note the plateau (u_o = const.) in the displacement spectrum towards low frequencies ($f < f_c$) and the high-frequency decay $\sim f^2$ for frequencies $f > f_c$.

According to Aki (1967) a simple seismic shear source with linear rupture propagation shows in the far-field smooth displacement and velocity spectra. When corrected for the effects of geometrical spreading and attenuation we get source spectra similar to the generalized ones shown in Figure II.1. The given magnitude values M_S correspond to a non-linear M_S-log M_0 relationship which is based on work published by Berckhemer (1962) and Purcaru and Berckhemer (1978). Note that the 1960 Chile earthquake had a seismic moment M_0 of about $3 \cdot 10^{23}$ Nm and a "saturated" magnitude of M_S = 8.5. This corresponds well with Figure II.1. There exist also other, non-linear empirical M_S-log M_0 relationships (e.g., Geller, 1976). The following general features are obvious from Figure II.1:

- source spectra are characterized by a plateau of constant displacement for frequencies smaller than the corner frequency f_c which is inversely proportional to the source dimension, i.e., $f_c \sim 1/L$;
- the decay of spectral displacement amplitude beyond $f > f_c$ is proportional to f^{-2} ;
- the plateau amplitude increases with seismic moment M_0 and magnitude, while at the same time f_c decreases proportional to M_0^{-3} (see Aki, 1967);

Details of theoretical source spectra depend on the assumptions in the model of the rupture process, e.g., when the rupture is - more realistically - bilateral, the displacement spectrum of the source-time function is for $f >> f_c$ proportional to f^{-2}, whereas this high- frequency decay is proportional f^{-3} for an unilateral rupture. On the other hand, when the linear dimensions of the fault rupture differ in length and width then two corner frequencies will occur. Another factor is related to the details of the source time function. Whether the two or three corner frequencies are resolvable will depend on their separation. In the case of real spectra derived from data limited in both time and frequency domain, resolvability will depend on the signal-to-noise ratio. Normally, real data are too noisy to allow the discrimination between different types of rupture propagation and geometry.

The general shape of the seismic source spectra can be understood as follows: we know from optics that under a microscope no objects can be resolved which are smaller than the wavelength λ of the light with which it is observed. In this case the objects appear as a blurred point or dot. In order to resolve more details, electron microscopes are used which operate with much smaller wavelengths. The same holds true in seismology. When observing a seismic source of radius r with wavelengths $\lambda >> r$ at a great distance, one cannot see any information about the details of the source process. One can only see the overall (integral) source process, i.e., one "sees" a point source. Accordingly, spectral amplitudes with these wavelengths are constant and form a spectral plateau (if the source

duration can be neglected). On the other hand, wavelengths that have $\lambda << r$ can resolve internal details of the rupture process. In the case of an earthquake they correspond to smaller and smaller elements of the rupture processes or of the fault roughness (asperities and barriers). Therefore, their spectral amplitudes decay rapidly with higher frequencies. The corner frequency, f_c, marks a critical position in the spectrum which is obviously related to the size of the source. According to Brune (1970) and Madariaga (1976), both of whom modeled a circular fault, the corner frequency in the P- or S-wave spectrum, respectively, is $f_{c\ p/s} = c_m v_{p,s} / \pi r$. In contrast, assuming a rectangular fault, Haskell (1964) gives the relationship $f_{c\ p/s} = c_m v_{p,s} /(L \times W)^{1/2}$ with L the length and W the width of the fault. The values c_m are model dependent constants. Accordingly, the critical wavelength $\lambda_c = v/f_c$, beyond which the source can be realized as a point source only, is $\lambda_c = c_m \pi r$ or $\lambda_c = c_m (L \times W)^{1/2}$, respectively.

Thus, from both the source area (which, of course, is based on model assumptions of the shape of the rupture) and the seismic moment from seismic spectra, one can estimate from Eq. (1) the average total displacement, $\bar{D}$. Knowing $\bar{D}$, other parameters such as the stress drop in the source area can be inferred. Stress drop means the difference in acting stress at the source region before and after the earthquake.

II.2.3 Magnitude of seismic events

Magnitude is a logarithmic measure of the size of an earthquake or explosion based on instrumental measurements. The earliest magnitude concept (local magnitude, M_L) was first proposed by Charles Richter (1935) for southern California earthquakes.

Magnitudes are derived from ground motions amplitudes and periods or from signal duration measures from instrumental records. There is no *a priori* scale limitation to magnitudes as exist for macro-seismic intensity scales. Magnitudes are often misleadingly referred to in the press as "... according to the open-ended RICHTER scale...". In fact, the maximum size of tectonic earthquakes is limited by nature, i.e., by the maximum size of a brittle fracture in a finite and heterogeneous lithospheric plate. The largest moment magnitude, M_w, observed so far was that of the Chile earthquake in 1960 (Mw ≈ 9.5; Kanamori 1977). On the other hand, the magnitude scale is open at the lower end. Nowadays, highly sensitive instrumentation close to the sources may record events with magnitude much smaller than zero. According to Richter´s original definition these magnitude values become negative.

II.2.3.1 Moment Magnitude M_W

According to Eq. (4) and Figure II.1 the scalar seismic moment $M_0 = \mu \overline{D} A$ is determined from the asymptote of the displacement amplitude spectrum as frequency f $\rightarrow$ 0 Hz and it does not saturate. Kanamori (1977) proposed, therefore, a moment magnitude, M_W, which is tied to M_S but which would not saturate. He reasoned as follows: According to Kostrov (1974) the radiated seismic strain energy is proportional to the stress drop $\Delta\sigma$, namely $E_S \approx \Delta\sigma \overline{D} A / 2$. With Eq. (4) one can write $E_S \approx (\Delta\sigma / 2\mu) M_0$. Assuming a reasonable value for the shear modulus μ in the crust and upper mantle (about 3-6 × 10^4 MPa) and assuming that, according to Kanamori and Anderson (1975) and Abe (1975), the stress drop of large earthquakes is remarkably constant (ranging between about 2 and 6 MPa), one gets as an average $E_S \approx M_0 / 2 \times 10^4$. Inserting this into the relationship proposed by Gutenberg and Richter (1956c) between the released seismic strain energy E_S and M_S, namely

$$\log E_S = 4.8 + 1.5 M_S \tag{5}$$

it follows:

$$\log M_0 = 1.5 M_S + 9.1 \tag{6}$$

Solving (4) for the magnitude and replacing M_S with M_W one gets

$$M_W = 2/3 (\log M_0 - 9.1) \tag{7}$$

Note that M_W scales well with the logarithm of the rupture area. The determination of M_0 on the basis of digital broadband records is becoming increasingly standard at modern observatories and network centers. This applies not only to very strong and teleseismic events but also to comparable scaling of moderate and weak events, both in the teleseismic and the local/regional range. The computed M_0, however, depends on details of the individual inversion methodologies and thus the related M_W may differ.

II.2.4 Orientation of the fault plane and the fault slip

Assuming that the earthquake rupture occurs along a planar fault surface, the orientation of this plane in space can be described by three angles (Figure II.2): strike ϕ is measured clockwise against North (0° to 360°), dip δ describes the inclination of the hanging wall against the horizontal (0° to 90°) and the rake angle λ describes the displacement of the hanging wall relative to the footwall (-180° to 180°).

Note that in the case of a shear model the fault-plane solution (i.e., the information about the orientation of the fault plane and of the fault slip in space) forms, together with the information about the static seismic moment M_0, the seismic moment tensor M_{ij}. Its principal axes coincide with the direction of the pressure axis, P, and the tension axis, T, associated with fault-plane solutions. They should not be mistaken for the principal axes σ_1, σ_2 and σ_3 (with $\sigma_1 > \sigma_2 > \sigma_3$) of the acting stress field in the Earth which are described by the stress tensor. Only in the case of a fresh crack in a homogeneous isotropic medium in a whole space with no pre-existing faults and vanishing internal friction is P in the direction of σ_1 while T has the opposite sense of σ_3. P and T are perpendicular to each other and each one forms, under the above conditions, an angle of 45° with the two possible conjugate fault planes (45°-hypothesis) which are in this case perpendicular to each other. The orientation of P and T is also described by two angles each: azimuth and plunge. They can be determined by knowing the respective angles of the fault plane. If the above model assumptions hold true, knowing the orientation of P and T in space, one can estimate the orientations of σ_1 and σ_3. Most of the data used for compiling the global stress map (Zoback 1992) come from earthquake fault-plane solutions calculated under these assumptions.

In reality, the internal friction of rocks is not zero. For most rocks this results, according to Andersons´s theory of faulting (1951), in the formation of conjugate pairs of faults which are oriented at about $\pm$ 30° to σ_1. In this case, the directions of P and T, as derived from fault- plane solutions, will not coincide with the principal stress directions. Near the surface of the Earth one of the principal stresses is almost always vertical. In the case of a horizontal compressive regime, the minimum stress σ_3 is vertical while σ_1 is horizontal. This results, when fresh faults are formed in unbroken rock, in thrust faults dipping about 30° and striking parallel or anti-parallel to σ_2. In an extensional environment, σ_1 is vertical and the resulting dip of fresh normal faults is about 60°. When both σ_1 and σ_3 are horizontal, vertical strike-slip faults will develop, striking with $\pm$ 30° to σ_1. But most earthquakes are associated with the reactivation of pre-existing faults rather than

occurring on fresh ones. Since the frictional strength of faults is generally less than that of unbroken rock, faults may be reactivated at angles between σ_1 and fault strike that are different from 30°. In a pre-faulted medium this tends to prevent failure on a new fault. Accordingly, there is no straightforward way to infer from the P and T directions determined for an individual earthquake the directions of the acting principal stress. On the other hand, it is possible to infer the regional stress based on the analysis of many earthquakes in that region since the possible suite of rupture mechanisms activated by a given stress regime is constrained. This method aims at finding an orientation for σ_1 and σ_3 which is consistent with as many as possible of the actually observed fault-plane solutions (e.g., Gephart and Forsyth, 1984; Reches, 1987; Rivera, 1989).

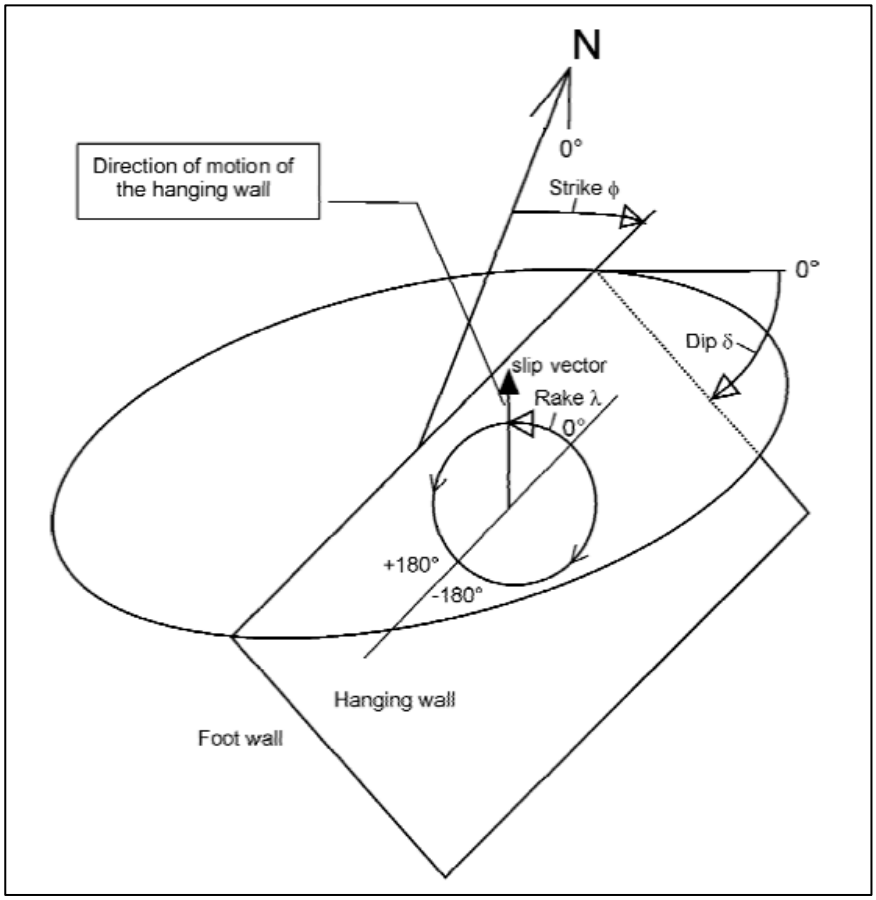

Figure II.2: Angels describing the orientation and motion of the faults (Encyclopedia of Earth Sciences Series 2011)

II.2.4.1 Fault plane solutions

Figure II.3 and II.4 depict several basic types of earthquake faulting and their related fault-plane solutions in so-called "beach-ball" presentations of the net projections.

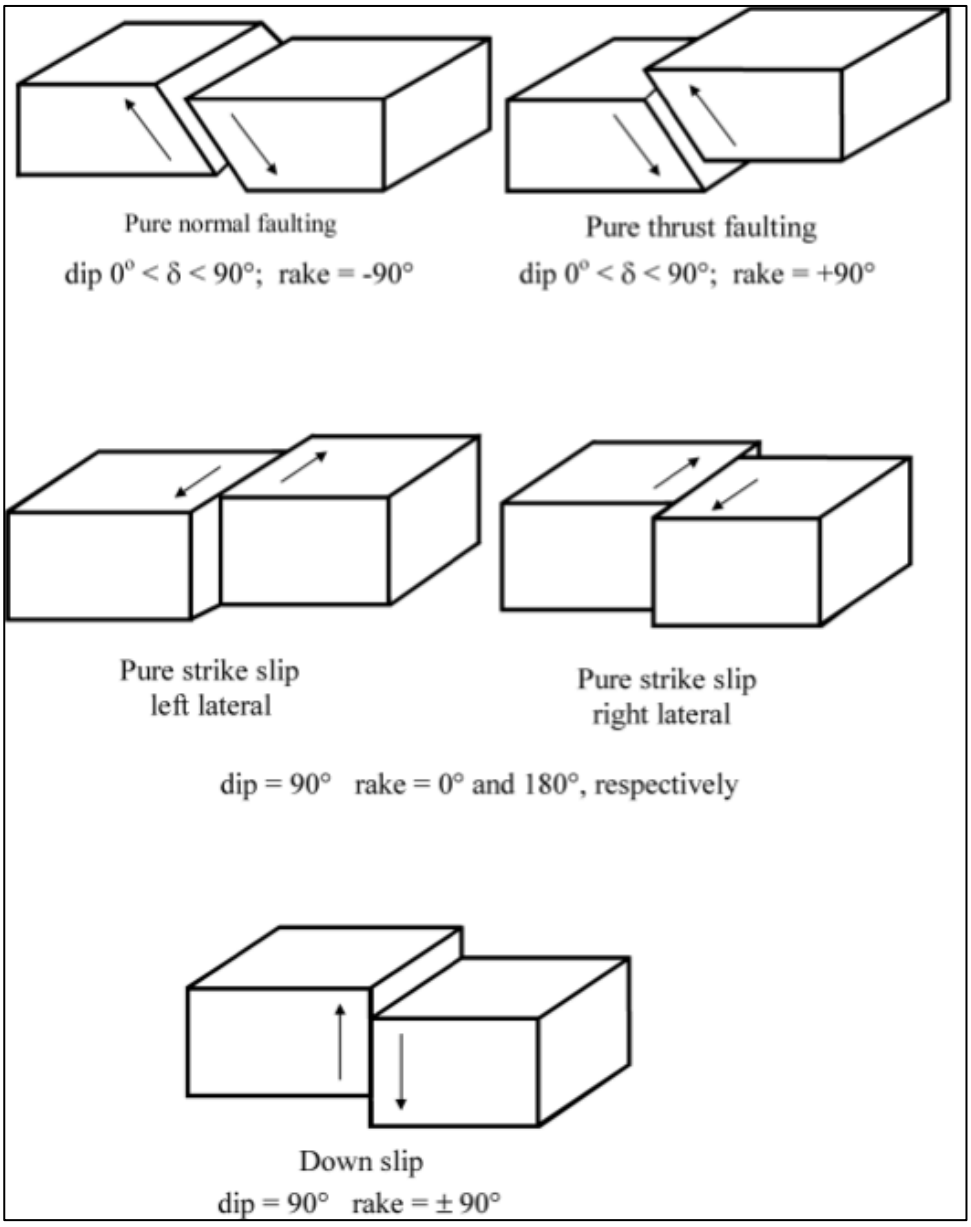

Figure II.3: Basic types of earthquake faulting for some selected dip and rake angles. Note that mixed types of faulting occur when $\lambda \neq 0$, 180^{o} or $\pm\ 90^{o}$, e.g., normal faulting with strike-slip component or strike-slip with thrust component. Also, dip angles may vary between $0^{o} < \delta \leq 90^{o}$. For fault plane traces and polarity distributions of these faulting types in their "beach-ball presentation" see Figure II.4 (U.S Geological Survey image).

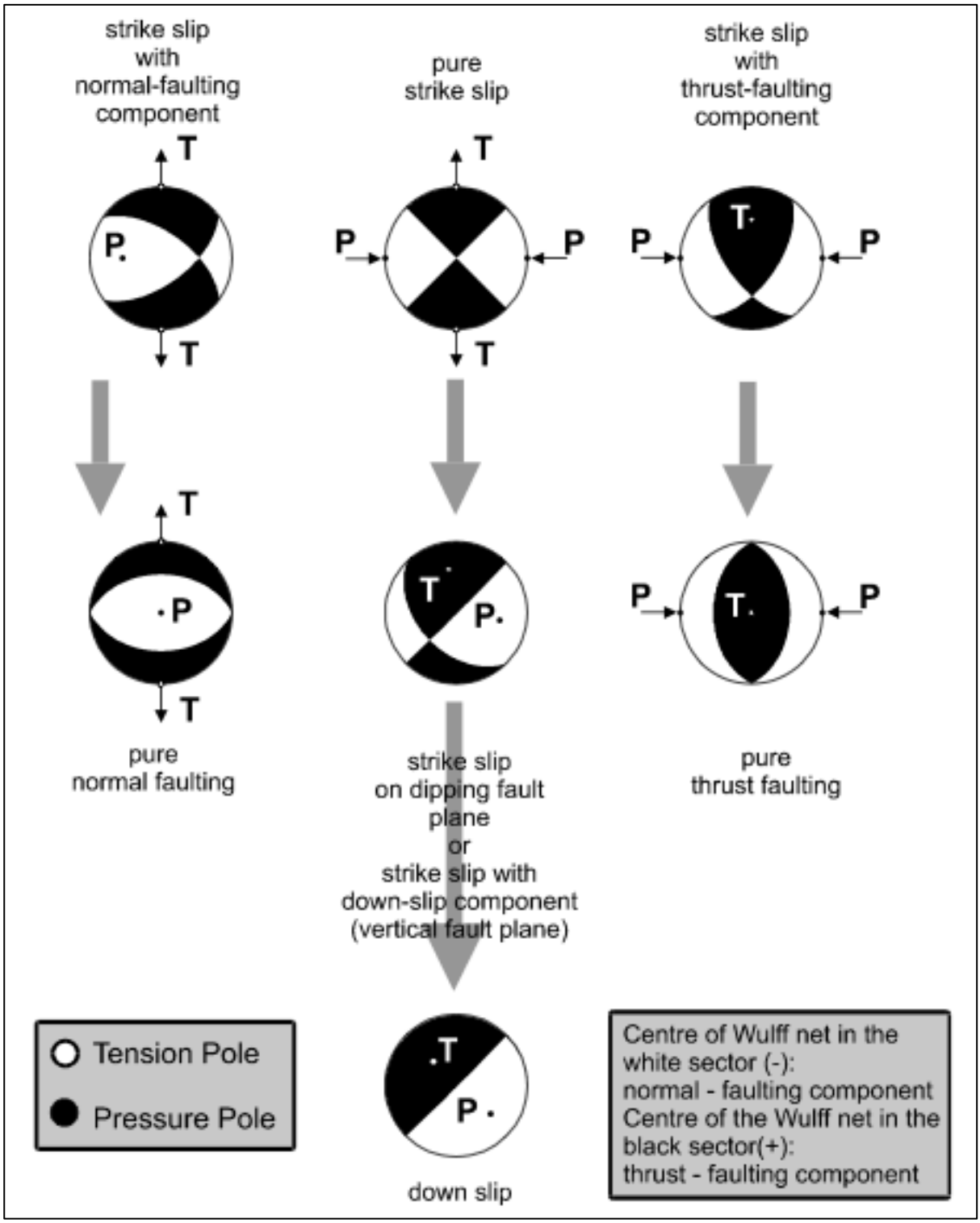

Figure II.4: Beach ball presentation of the net projections of the fault plane cut-traces and of the penetration points (poles) of the P- and T-axes through the lower focal hemisphere for different faulting mechanisms. White sector correspond to negative and black sector to positive firts-motion polarities (from Stein and Wysession, 2003).

II.3 Moment tensor solutions

The concept of first order moment tensor provides a complete description of equivalent body forces of a general seismic point source (Figure II.5). A source can be considered a point source if both the distance D of the observer from the source and the wavelength λ of the data are much greater than the linear dimension of the source. Thus, moment-tensor solutions are generally derived from low-frequency data and they are representative of the gross properties of the rupture process averaged over tens of seconds or more. The double-couple source model describes the special case of shear dislocation along a planar fault. This model has proven to be very effective in explaining the amplitude and polarity pattern of P, S and surface waves radiated by tectonic earthquakes. In the following, we briefly outline the relevant relations (in a first-order approximation) between the moment tensor of a seismic source and the observed seismogram. The latter may be either the complete seismogram, one of its main groups (P, S or surface waves), or specific features of seismograms such as peak-to-peak amplitudes of body waves, amplitude ratios or spectral amplitudes. Then we outline a linear inversion scheme for obtaining the moment tensor using waveform data in the time domain. Finally, we will give an overview of some useful programs for moment-tensor analysis. Applications of moment-tensor inversions to the rapid determination of source parameters after significant earthquakes will also be described.

II.3.1 Basic relations

Following Jost and Herrmann (1989), the displacement d on the Earth's surface at a station can be expressed, in case of a point source, as a linear combination of time-dependent moment-tensor elements M_{kj} (ξ,t) that are assumed to have the same time dependence convolved (indicated by the star symbol) with the derivative G_{skj} (x,ξ,t) of the Green's functions with regard to the spatial j-coordinate:

$$u_S(x,t) = M_{kj}(\xi,t) * G_{sk,j}(x,\xi,t) \tag{8}$$

where u_S (x,t) is the s component of ground displacement at position x and time t; M_{kj} (ξ,t) are the components of 2nd order, symmetrical seismic moment tensor M; $G_{sk,j}$ (x,ξ,t) is the derivative of the

Green's function with regard to source coordinate ξ_j ; x is the position vector of station with coordinates x_1 , x_2 , x_3 for north, east and down; ξ is the position vector of point source with coordinates ξ_1 , ξ_2 , ξ_3 for north, east and down. Eq. (8) follows from the representation theorem in terms of the Green´s function. The Green's function represents the impulse response of the medium between source and receiver and thus contains the various wave propagation effects through the medium from source to receiver. These include energy losses through reflection and transmission at seismic discontinuities, anelastic absorption and geometrical spreading. The M_{kj} (ξ,t) from Eq.(8) completely describes the forces acting in the source and their time dependence. The Einstein summation notation is applied in Eq. (8) and below, i.e., the repeated indices k and j = 1, 2, 3 imply summation over x_1, x_2 and x_3. In Eq. (8) the higher order terms of the Taylor expansion around the source point of the Green's functions $G_{sk,j}$ (x,ξ,t) have been neglected. If we assume that all the components of M_{kj} (ξ,t) have the same time dependence s(t) (i.e., the same source-time history), the equation which describes the time dependence of moment released at the source, can be written as:

$$u_S(x,t) = M_{kj}\left[G_{sk,j}(x,\xi,t) * s(t)\right] \tag{9}$$

When determining M_{kj} (ξ,t) from seismic records, u_s(x, t) is calculated by convolution of the observed seismogram components y_s(x, t) with the inverse of the seismograph's displacement response function i(t):

$$u_S(x,t) = y_S(x,t) * Inv\{i(t)\} \tag{10}$$

In the frequency domain convolution is replaced by multiplication:

$$D_S(x,\omega) = Y_S(x,\omega)\, I(\omega)^{-1} \tag{11}$$

where ω is circular frequency. The D_s(x, ω), Y_s (x, ω), and $I(\omega)^{-1}$ are the respective Fourier transforms of the time series d_s(x, t), y_s(x, t), and $i(t)^{-1}$.

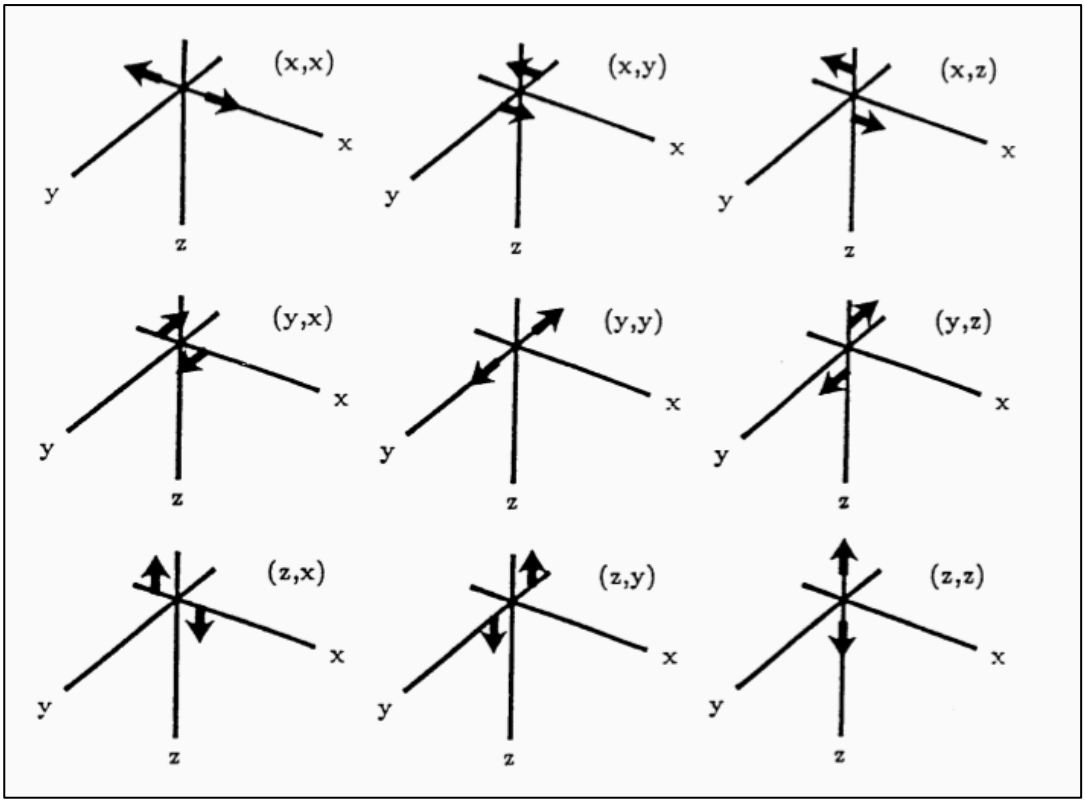

Figure II.5: The nine generalized couples representing $G_{sk,j}(x, \xi, t)$ in Eq. (8). Note that force couples acting on the y axis in x direction or vice versa (i.e., (x,y) or (y,x)) will cause shear faulting in the x and y direction, respectively. Superimposition of vector dipoles in x and y direction with opposite sign, e.g., (x,x) + (-y,-y) will also cause shear faulting but 45° off the x and y direction, respectively. Both representations are equivalent (reproduced from Jost and Herrmann, A student's guide to and review of moment tensors. *Seismol. Res. Lett.*, 60, 2, 1989, Fig. 2, p. 39; ©Seismological Society of America).

In the following we assume that the source-time function s(t) is a delta function (i.e., a "needle" impulse). Then, $M_{kj}(\xi, t) = M_{kj}(\xi)\delta(t)$, and the right side of Eq.(9) simplifies to $M_{kj}(\xi)G_{sk,j}(t)$. The seismogram recorded at x can be regarded as product of $G_{sk,j}$ and M_{kj}. (e.g., Aki and Richards, 1980, Lay and Wallace, 1995; Udias, 1999). Thus, the derivative of G_{skj} with regard to the source coordinate ξ_i describes the response to a single couple with its lever arm pointing in the ξ_j direction (Figure II.5). For k = j we obtain a vector dipole; these are the couples (x,x), (y,y), and (z,z) in Figure II.5. A double-couple source is characterized by a moment tensor where one eigenvalue of the moment tensor vanishes (equivalent to the Null or B axis), and the sum of eigenvalues vanishes, i.e., the trace of the moment tensor is zero. Physically, this is a representation of a shear dislocation source without any volume changes. Using the notation of Figure II.3, double-couple displacement

fields are represented by the sum of two couples such as (x,y)+(y,x), (x,x)+(y,y), (y,y)+(z,z), (y,z)+(z,y) etc.

The seismic moment tensor M_0 has, in general, six independent components that follow from the condition that the total angular momentum for the equivalent forces in the source must vanish. For vanishing trace, i.e., without volume change, we have five independent components that describe the deviatoric moment tensor. The double-couple source is a special case of the deviatoric moment tensor with the constraint that the determinant of M_0 is zero, i.e., that the stress field is two-dimensional.

In general, M can be decomposed into an isotropic and a deviatoric part:

$$M=M^{isotropic}+M^{deviatoric} \tag{12}$$

The decomposition of M is unique while further decomposition of $M^{deviatoric}$ is not. Commonly, $M^{deviatoric}$ is decomposed into a double couple and CLVD:

$$M^{deviatoric}=M^{DC}+M^{CLVD} \tag{13}$$

For a double-couple source, the Cartesian components of the moment tensor can be expressed in terms of strike φ, dip δ and rake λ of the shear dislocation source (fault plane), and the scalar seismic moment M_0 (Aki and Richards, 1980).

As the tensor is always symmetric it can be rotated into a principal axis system such that all non-diagonal elements vanish and only the diagonal elements are non-zero. The diagonal elements are the eigenvalues of M; the associated directions are the eigenvectors (i.e., the principal axes). A linear combination of the principal moment-tensor elements completely describes the radiation from a seismic source. In the case of a double-couple source, for example, the diagonal elements of M in the principal axis system have two non-zero eigenvalues M_0 and $-M_0$ (with M_0 the scalar seismic moment) whose eigenvectors give the direction at the source of the tensional (positive) T axis and compressional (negative) P axis, respectively, while the zero eigenvalue is in the direction of the B (or Null) axis of the double couple.

Eq. (9) describes the relation between seismic displacement and moment tensor in the time domain. If the source-time function is not known or the assumption of time-independent moment-tensor elements is dropped, e.g., for reasons of source complexity, the frequency- domain approach is chosen:

$$u_S(x,t) = M_{kj}(f) G_{sk,j}(x,\xi,f) \tag{14}$$

where f denotes frequency. Procedures for the linear moment-tensor inversion can be designed in both the time and frequency domain using Eq. (9) or (14). We can write (9) or (14) in matrix form:

$$u = G\overline{m} \tag{15}$$

In the time domain, the u is a vector containing n sampled values of observed ground displacement at various times, stations and sensor components, while G is a 6 × n matrix and the vector m contains the six independent moment-tensor elements to be determined. In the frequency domain, u contains k complex values of the displacement spectra determined for a given frequency f at various stations and sensor components. G is a 6 × k matrix and is generally complex like m. For more details on the inversion problem in Eq. (16) the reader is referred to Chapter 6 in Lay and Wallace (1995), Chapter 12 in Aki and Richards (1980), or Chapter 19 of Udias (1999). To invert Eq. (16) for the unknown m, one has to calculate the derivatives of the Green's functions. The calculation of the Green's functions constitutes the most important part of any moment-tensor inversion scheme. A variety of methods exists to calculate synthetic seismograms (e.g., Müller, 1985; Doornbos, 1988; Kennett, 1988). Some of the synthetic seismogram codes allow calculations for the moment-tensor elements as input source while others allow input for double-couple and explosive point sources. The general moment tensor can be decomposed in various ways using moment-tensor elements of double-couple and explosive sources so that synthetic seismogram codes employing these source parameterizations can also be used in the inversion of (16).

II.3.2 Decomposition of the moment tensor

Except for the volumetric and deviatoric components, the decomposition of the moment tensor is not unique. Useful computer programs for decomposition were written by Jost and distributed in Volume VIII of the Computer Programs in Seismology by Herrmann of Saint Louis University (http://www.eas.slu.edu/People/RBHerrmann/ComputerPrograms.html). The first step in the decomposition is the calculation of eigenvalues and eigenvectors of the seismic moment tensor. It performs rotation of the moment tensor M into the principal axis system. The eigenvector of the largest eigenvalue gives the T (or tensional) axis; the eigenvector of the smallest eigenvalue gives

the direction of the P (or compressional) axis, while the eigenvector associated with the intermediate eigenvalue gives the direction of the Null axis. The output is the diagonalized moment tensor

$$M = \begin{bmatrix} m_1 & 0 & 0 \\ 0 & m_2 & 0 \\ 0 & 0 & m_3 \end{bmatrix} \tag{16}$$

First, the moment tensor is decomposed into an isotropic and a deviatoric part (Eq. 12):

$$M = \frac{1}{3}\begin{bmatrix} tr(M) & 0 & 0 \\ 0 & tr(M) & 0 \\ 0 & 0 & tr(M) \end{bmatrix} + \begin{bmatrix} m_1^1 & 0 & 0 \\ 0 & m_2^1 & 0 \\ 0 & 0 & m_3^1 \end{bmatrix} \tag{17}$$

with $tr(M) = m_1 + m_2 + m_3$ being the trace of M. The isotropic part of M is important in quantifying volume changes of the source, but it is usually difficult to resolve so that isotropic parts of less than 10% are often not considered to be significant. The deviatoric part of the moment tensor can be further decomposed. Options include decompositions into three vector dipoles, into three double couples, into 3 CLVD sources, into a major and minor double couple, and into a best double couple and a CLVD having the same principal axis system. The source mechanisms reported by Harvard and USGS are based on the decomposition of the moment tensor into a best double couple and a CLVD. In addition to the best double couple they also provide the moment-tensor elements. To estimate the double-couple contribution to the deviatoric moment tensor, the parameter

$$\varepsilon = \frac{|m_{\min}|}{|m_{\max}|} \tag{18}$$

is used (Dziewonski et al., 1981) where m_{min} and m_{max} are the smallest and largest eigenvalues of the deviatoric part of M, respectively, both in absolute terms. For a pure double-couple source, $\varepsilon = 0$ because $m_{min} = 0$; for a pure CLVD, $\varepsilon = 0.5$. The percentage double-couple contribution can be expressed as $(1-2\varepsilon)\times 100$. Significant CLVD components are often reported for large intermediate-depth and very deep earthquakes. In many cases, however, it can be shown that these are caused by

superposition of several rupture events with different double-couple mechanisms (Kuge and Kawakatsu, 1990; Frohlich, 1995; Tibi et al., 1999).

Generally, the quality of moment-tensor inversion depends to a large extent on the number of data available and the azimuthal distribution of stations about the source. Dufumier (1996) gives a systematic overview for the effects caused by differences in the azimuthal coverage and the effects caused due to the use of only P waves, P plus SH waves or P and SH and SV waves for the inversion with body waves. A systematic overview with respect to the effects caused by an erroneous velocity model for the Green function calculation and the effects due to wrong hypocenter coordinates can be found in Šílený et al. (1992), Šílený and Pšenčik (1995), Šílený et al. (1996) and Kravanja et al. (1999). The following is a general outline of the various steps to be taken in a moment-tensor inversion using waveform data:

1) Data acquisition and pre-processing
   - good signal-to-noise ratio;
   - unclipped signals;
   - good azimuthal coverage;
   - removing mean value and linear trends;
   - correcting for instrument response, converting seismograms to displacement low-pass filtering to remove high-frequency noise and to satisfy the point source approximation.

2) Calculation of synthetic Green's functions dependent on
   - Earth model;
   - location of the source;
   - receiver position.

3) Inversion
   - selection of waveforms;
   - taking care to match waveforms with corresponding synthetics;
   - decomposition of moment tensor, e.g., into best double couple.

Care must be taken to match the synthetic and observed seismograms. The inversion is done for a range of focal depths and as best solution one takes that with the minimum variance of the estimate.

II.4 Developments of Earthquake Source Models

Several field evidences suggested that earthquakes are caused by faulting (e.g., Richter, 1958). On account of this, dislocation models were developed to model an earthquake as a slip on the fault. Brief description of some of the early models is mentioned below:

Burridge and Knopof (1964) derived expression for the body force to be applied to represent a dislocation and produces radiation pattern identical to that of the dislocation. This equivalent body force depends only upon the source and the elastic properties of the medium in the vicinity of the source. The study demonstrated that a displacement discontinuity is represented as an equivalent double couple body force. Haskell (1964) proposed a rectangular fault model to represent a propagating displacement discontinuity. This model considered a uniform displacement discontinuity moving at a constant rupture velocity along a thin fault of length L and width W. At wavelengths much longer than the size of the fault, this model is a reasonable approximation of a simple seismic rupture propagating along a strike slip fault. Haskell's model has been extensively used to invert for seismic source parameters in the near and far-field using seismic and geodetic data. Madariaga (1978) computed the seismic radiation of Haskell's model and showed that due to the stress singularities around the edges, this model fails at high frequencies. All dislocation models with constant slip suffer from this problem and Sato and Hirasawa (1973) proposed tapering the slip discontinuity near the edges of the fault to reduce this problem. Savage (1966) proposed an elliptical fault model and studied the effects on the spectra of body and surface waves. The spectra of the pulses from Savage's model exhibited two band-limitated components which may be associated with two intervals in the time domain; the first is associated with the time interval preceding the first stopping phase, and the interval over which the first and final stopping phase occur. The second is associated with the time interval between the stopping phases. The pulse can be approximated by the convolution of two boxcar functions having these intervals (τ_1,τ_2). The amplitude spectrum of the pulse is the product of two sinc-functions for which the first zeros occur at frequencies that are inversely proportional to the time intervals. Thus the spectrum have a ω^1 roll-off at a frequency of $1/\tau_1$ Hz, and a ω^2 roll-off at a frequency $1/\tau_2$ Hz.

Aki (1967) developed scaling law that depicted the dependence of the amplitude spectrum of seismic waves with magnitude. Two source models of an earthquake were considered in the study ω^3 model after Haskell and the other ω^2 model obtained by fitting an exponentially decaying function to the autocorrelation function of dislocation velocity. The theoretical curves were

calibrated with observations by comparing the ratios of the theoretical spectra with the observed spectra of seismic waves from earthquakes having same propagation path. The theory was also checked with the empirical relations between different magnitude scales and spectra were calibrated with surface wave magnitude (M_S). The study concluded that the ω^2 model is in agreement with observations on the assumption of similarity.

Brune (1970, 1971) modeled an earthquake dislocation as a tangential stress pulse applied to the interior of a dislocation surface. The stress pulse sends a shear-stress wave perpendicular to the dislocation surface. This model describes near and far-field displacement time functions and spectra and takes into accounts the effects of fractional stress drop. The model successfully explained the near and far-field spectra observed for earthquakes and has been extensively used to compute source parameters from observational data.

Boatwright (1980) developed a spectral theory for circular seismic sources and derived expressions to estimate source dimension, dynamic stress drop, and radiated seismic energy. Far-field body wave radiation from this model as a function of takeoff angle, rupture velocity, and stopping behavior was investigated and the variation of spectral shape, pulse shape, and energy flux over the focal sphere was quantified. The study provided two new methods for estimating the source dimension, the first through the inversion of a characteristic frequency, and the second using the rise time of the displacement pulse shape. The model also allowed a direct estimate of the dynamic stress drop from the shape of velocity pulse. A new spectral parameter , the integral of the square of the ground velocity was given to calculate total radiated energy. The proposed theory includes directivity and found this valid for a range of subsonic rupture velocities.

The above mentioned theoretical source models (e.g., ω -square or ω –cube source models) and many other source models developed subsequently demonstrated the frequency dependent behavior of seismic spectra with increasing earthquake size. Using these models, a large number of studies have been carried out to estimate earthquake source parameters and develop scaling laws from observational data collected from various parts of the world.

II.5 Methods to Compute Earthquake Source Parameters

The methods to compute earthquake source parameters can be broadly classified into two categories: the time domain methods and frequency domain methods. These methods are described in the following sections.

II.5.1 Time Domain Methods

O'Neel and Healy (1973) gave a simple method to estimate source dimensions and stress drops of small earthquakes. This method is based on the measurement of time from the first break to the first zero crossing on short-period seismograms. This time is related to rise-time as a function of Q and instrument response and simple expressions were given to estimate the source parameters. The method was applied on data collected from Rangely, Colorado and Hollister, California and gave reasonable results. The need to develop this method aroused because the short period seismographs used to record local earthquakes have limited dynamic range both in amplitude and frequency, and clipping of records occurred when the seismographs were operated at high gain to detect events up to zero magnitude. Further, the limited high frequency response obscured the corner frequencies of the events that can be recorded within the dynamic range of the recording system. It was argued that the ideal data for computing source parameters should be recorded on instruments having a wide dynamic range and broadband frequency response. However, earlier such instruments were expensive and were not usually operated for microearthquake studies (Tucker and Brune, 1973).

Chung and Kanamori (1980) estimated the source dimensions, modes of rupture propagation, seismic moments, and stress drops from body wave pulse-widths of 17 intermediate and deep focus earthquakes that occurred in the Tonga-Kermadec region. These source parameters were interpreted to investigate variations in source properties and the state of stress within the descending slab. Stress drops of the 17 events vary from 2 MPa to about 460 MPa, and varied significantly with depth. It was interpreted that the change in stress drop at about 220 km in depth seems to reflect a change in material properties both in the mantle and within the slab. Two regions of high stress drop at depths of about 360 and 640 km and minimum stress drop at about 450–560 km (where the earthquake frequency is particularly high) were observed. The study brought out that earthquakes in regions of low seismicity appear to have higher stress drops than those in regions of high seismicity and the upper bound of seismic efficiency decreases with depth, implying an increase of frictional force with depth at the earthquake source.

Frankel and Kanamori (1983) developed a simple technique to determine the rupture duration and stress drop of earthquakes between magnitudes 3.5 and 4.0 using the time between the P-wave onset and the first zero crossing on seismograms from local seismic networks. This technique was applied to ten main shocks in southern California to investigate regional variations in stress drop. The measured pulse widths ($\tau_{1/2}$) of 65 foreshocks or aftershocks showed that $\tau_{1/2}$ for small

earthquakes below about magnitude 2.2 remain constant with decreasing magnitude in four sequences. It was found the relative pulse width of a main shock at a given station can be correlated with the relative pulse width of its aftershocks recorded at that station. From these observations it was interpreted that the waveforms of small events (M ~ 2.2) are essentially the impulse response of the path between the source and receiver. To allow path correction $\tau_{1/2}$ of small foreshocks and aftershocks were subtracted from the pulse widths of main shocks. The corrected pulse widths were used to estimate rupture duration and stress drop. The study brought out significant variations in rupture durations and stress drops of the main shocks. The observed variation in $\tau_{1/2}$ with aftershock locations and azimuths showed that the rupture zone of one earthquake expanded unilaterally. It was observed that the stress drop vary by a factor of 10 for two adjacent events of similar seismic moments occurring 1 hour apart on the San Jacinto fault system and an event having the highest stress drop (86 MPa) was followed within 8 months by a magnitude 5.5 earthquake.

O'Neill (1984) estimated source dimensions and stress drops of 30 small Parkfield, California, earthquakes ($1.2 \leq M_D \leq 3.9$) from the measurements of the times from the initial P-onset to the first zero crossing. These times, corrected for attenuation and instrument response, were interpreted adopting a circular source model in which rupture expands radially outward from the center point until it stops abruptly. The seismic moments, were estimated from the empirical relation between duration magnitude and seismic moment. Using the values of source radii and seismic moments, static stress drops were estimated. The study showed that source radii systemically increased with magnitudes from about 70 m for events near M_D 1.4 to about 600 m for an event of M_D 3.9. Static stress drop varied from about 0.2 to 3 MPa and had strong correlation with magnitude and the events with stress drops above 2 MPa were concentrated in a small region close to the hypocenter of the 1966 Parkfield earthquake.

Pearce and Stewart (1989) studied earthquake source models, in which a rupture propagates along a fault plane, and observed directivity effect in the duration of radiated signal and suggested the use of spectral corner frequencies to estimate the parameters of an extended source. However, the authors emphasized that in time domain, the measurements of pulse durations of teleseismic body waves recorded on broadband seismograms have certain advantages (e.g., easier estimation of confidence limits and treatment of interfering arrivals). A method is given to test the compatibility of observed pulse durations with possible source geometries derived from a propagating rupture model. The study showed the possibility to discriminate between source directivity and anelastic attenuation, and between the fault and auxiliary planes. Further, an accurate measurement of durations is neither realistic nor essential: a confidence of ± 30% in pulse duration is typical, but

better measurements are possible if the instrument phase response is removed from the observed seismogram.

II.5.2 Empirical Green's Function Method

Empirical green function method, initially given by Hartzell (1978), has been used in many studies to compute the source parameters of earthquakes (e.g., Frankel and Kanamori, 1983; Mueller, 1985; Frankel et al., 1986; Li and Thurber, 1988; Hutchings and Wu, 1990; Hough, 1997; Domanski and Gibowics, 2008). In this method the waveforms of smaller earthquakes are approximated by point sources in time and space and represent the impulse response of the path between the source and the receiver. The smaller event is assumed to have a corner frequency that is higher than the frequency band of interest, so that there is little source contribution to the frequency spectrum, and its waveform can be considered as an impulse response of the path, site and the instrument.

Radulian and Popa (1996) among others used the empirical green function (*EGF*) technique to estimate the source parameters of small earthquakes ($10^{14} < M_0 < 10^{16}$ N-m) from the measurements of first P-wave pulse widths on velocity record. A constant level of pulse width for magnitudes $M_L < M_{min}$ and an increase in pulse width with increasing magnitude beyond M_{min} was observed. In view of this the seismograms of events less than M_{min} were considered as an impulsive response whose pulse width is due to path and instrument response. This impulse response is deconvolved from the waveform of larger earthquake. In this way one can remove the contribution of attenuation, scattering, and site response and other effects. In a sense, the *EGF* method provides a more accurate account of path effects than the attenuation correction. This method is effective if larger event and smaller event have same location as well as focal mechanism. In principle, this method can be applied in the time domain (e.g., Mori et al., 2003) or in the frequency domain (Ide et al., 2003; Prieto et al., 2004; Abercrombie and Rice, 2005).

II.5.3 Frequency Domain Method

For any physical phenomenon that fluctuates in time and/or space, it is important to know its rate of fluctuation (i.e., the frequency or the wave-number). This is achieved by transforming the time domain signal to frequency domain called the spectrum of the signal. The frequency domain

representation in many respects is more attractive than the time domain because many Geophysical phenomena are theoretically represented in frequency domain. Further mathematical operations (e.g., filtering, attenuation, instrument corrections) are easier to apply in the frequency domain than in the time domain because convolved signals in time domain are multiplied signals in frequency domain. Another advantage of spectral analysis is that the whole signal shape is used in the analysis, whereas, normally the time domain measurements on seismograms are point measurements (e.g., the arrival time of the first onset of seismic waves and the direction of first arrival, and the maximum amplitude of the seismic wave). Analysis of the whole waveform obviously provides more information than point measurements in time domain.

The frequency domain methods are based on computing the spectra of different types of waves (e.g., P-waves, S-waves, surface waves and coda waves). Earlier studies were mainly based on computing the spectra of long period waves and the equalization techniques were adopted to isolate source and path effects. This method involves estimating source parameters by converting the time history to frequency domain. Path, site and instrument corrections all are applied in frequency domain.

III Comprehensive Assessments of Parkfield Earthquake Source estimates: a look into model variability.

Abstract

We investigate source parameters and scaling of 757 repeating micro-earthquakes occurring on the Parkfield segment of the San Andreas Fault (SAF) taking into account model (epistemic) variability due to method. We will compute source corner frequency and stress drop using multi-taper spectral analysis of P and S waves (Yoo et al., 2012), coda method (Mayeda et al., 2007) and inversion for source, path and site (e.g., Malagnini et al., 2007) using data from the borehole High Resolution Seismic Network (HRSN). The results of this analysis will be compared to estimates obtained from the Nadeau and Johnson (1998) asperity loading model, as well as finite-source models of earthquakes from M 1.8 to 6.0 (Dreger et al., 2007; Uchide and Ide, 2010). The aim of this work is to investigate the scaling of Parkfield seismicity where studies have suggested self-similar (Baltay et al., 2010), and non- self-similar scaling (Nadeau and Johnson, 1998). We also calculated an accurate moment magnitudes for most of the 757 events of our data set, between $M_W \sim 0$ and $M_W \sim 1.9$. The results of such analyses give us insights into the underlying mechanics of faulting and the earthquake process.

III.1 Introduction

Since 1984, digital seismograms of micro-earthquakes on the San Andreas Fault (SAF) in California have been recorded by the Northern California Seismic Network (NCSN) and borehole High Resolution Seismic Network (HRSN). On the Parkfield segment of the SAF, repeating earthquake seismicity is observed with highly similar waveforms, suggesting that the events occur on the same patch of fault repeatedly (Nadeau et al., 1995). Advanced analyses of these data have revealed the highly systematic nature of seismicity at Parkfield and that over time ~ 40% of the small magnitude seismicity repeats in sequences of characteristic earthquakes (Nadeau and Johnson, 1998; Nadeau and McEvilly, 1999). Other studies in central California, Taiwan and Japan have also reported finding sequences of small characteristic events, indicating that the phenomena is relatively widespread (Vidale et al., 1994; Ellsworth, 1995; Bürgmann et al., 2000; Igarashi et al., 2003; Chen and Rau, 2003; Nadeau and McEvilly, 2004).

The behavior of earthquake source scaling has been the topic of significant debate in the earthquake source community over the past two decades and remains controversial. However, the

records from these repeating micro-earthquakes provided an unprecedented opportunity to take an in-depth look at the source scaling and ground motion. A large number of source studies require substantial corrections for path attenuation, site amplification, and source radiation pattern effects. Generally, corner frequency and stress-drop estimates from conventional direct wave methods show significant scatter from azimuthal variation related to source radiation complexity.

If, on the one hand, these approaches result in corrections that are so large, that the resulting estimates on stress drop are questionable (Ide and Beroza, 2001; Abercrombie et al., 2006), on the other hand, the coda method developed by Mayeda and Walter (1996), and subsequently refined by Mayeda et al. (2003) is a well-evaluated technique that has been widely used in the explosion monitoring community for accurate source spectral estimation using sparse station deployments and for use in magnitude, discrimination, and explosion yield estimation, with variances that are typically 3–4 times smaller than the conventional methods using direct waves.

Moreover, the coda ratio methodology (Mayeda et al., 2007) is similar in every respect to the traditional direct wave spectral ratio method, which takes advantage of co-located earthquakes to remove common path and site effects. The significant difference, however, comes from the fact that the coda envelope measurements are very stable and not very sensitive to either the source radiation pattern or source directivity (Mayeda and Malagnini, 2010) and represent a convolution over the entire source–time process. For these reasons, we can obtain stable estimates of stress drop and corner frequency using the coda-based method. We apply an improved coda-ratio method that employs overlapping frequency band measurements as well as direct S-wave ratios using a multitaper spectral method (Park et al., 1987; Prieto et al., 2009) to estimate corner frequency and static stress drop and analyze error in the estimates. Next, we compare our result with estimates obtained from the Nadeau and Johnson (1998) asperity loading model, as well as finite-source models of earthquakes from M 1.8 to 6.0 (Dreger et al., 2007; Uchide and Ide, 2010). We believe this validation provides an in-depth look at the relationship between the earthquake source scaling and resulting observed ground motions.

III.2 Data Selection

Our data set consists on 757 repeating micro-earthquake (17.988 waveforms) subdivided in 42 clusters, occurred on the Parkfield segment of the San Andreas Fault (SAF) from 2002 to 2012 with $0 \leq M_W \leq 1.9$ (Figure III.1); these event are localizated in depth in the range of 2-10 Km as shown in the Figure III.2.

The high quality records from the earthquake sequence has been intensively studied and provided an unprecedented opportunity to examine various seismological topics. We use three-component velocity records from the Berkeley Seismological Laboratory's High Resolution borehole Seismic Network (HRSN) to determine accurate values of corner frequency and stress drop. In particular, we focused on three specific clusters (Figure III.3), namely the ones called: *San Francisco, Los Angeles,* and *Hawaii*, close together and with the largest M_w's (cluster numbers: 20, 32, 33, see Table III.1). Figure III.2 shows also the location of the target events respect to the HRSN and their location in depth (green dots). The recordings of the HRSN are sampled at 250 sps, giving an effective bandwith of ~100 Hz; moreover, instruments are located in boreholes at depths between 63 and 298 m, providing an exceptional signal to noise ratio (SNR) in the recordings. The level of waveform similarity (correlation coefficients exceeding 0.98) is observed for all three components at all stations, and attests to the nearly collocated nature of the events.

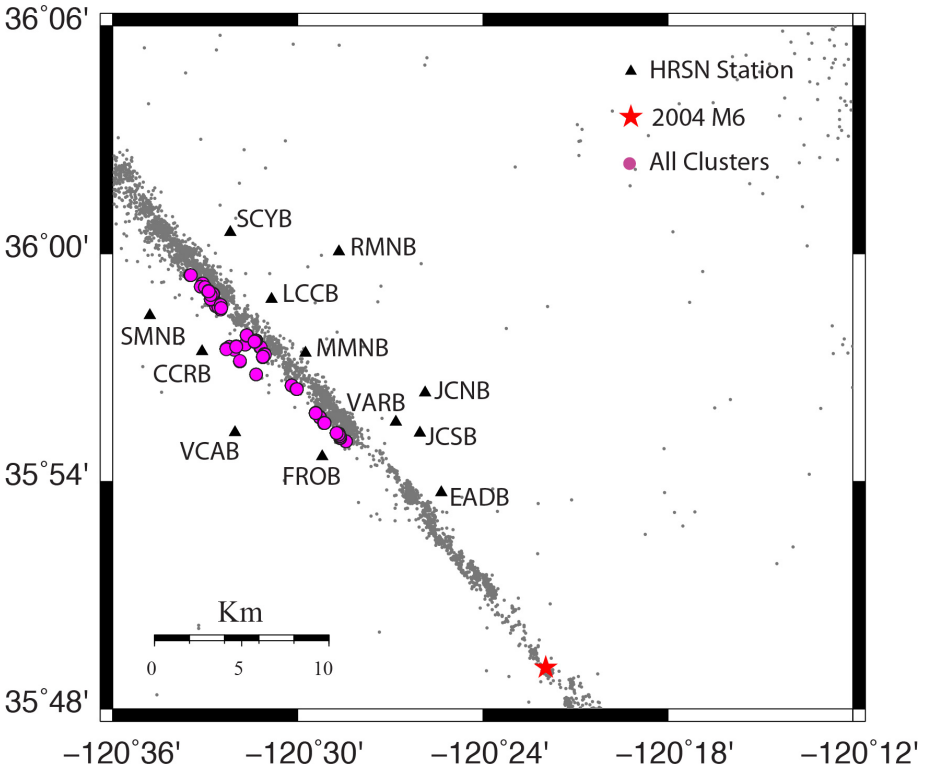

Figure III.1: Map showing the locations of HRSN stations (black triangles), the locations of the 2004 main shock epicenters (red stars), the locations of the 42 cluster used in this study (purple circles), and background seismicity (gray dots).

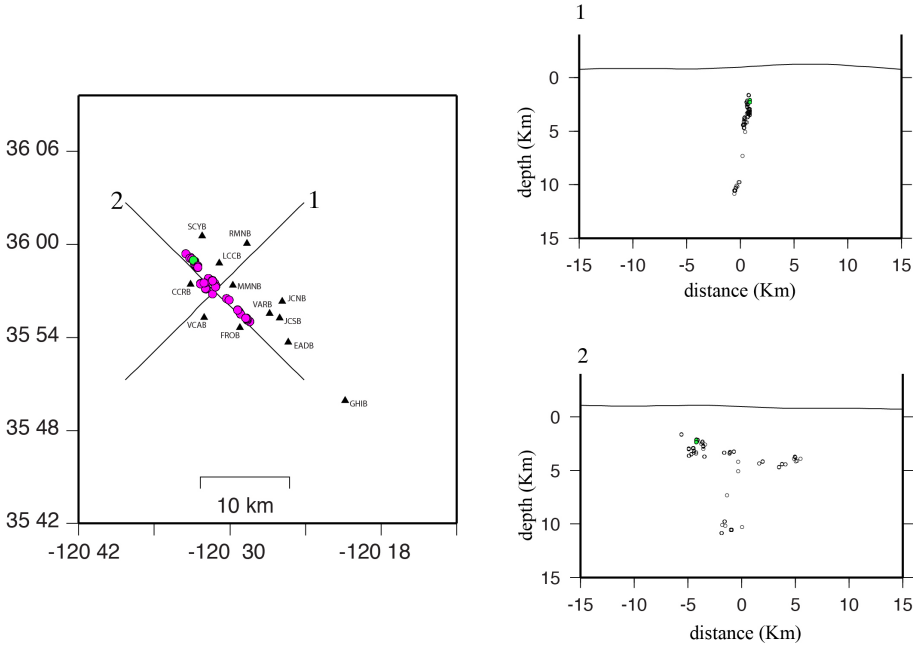

Figure III.2: Map showing the locations in depth of the 42 clusters used in this study (purple circles), the three target events (green circles), and HRSN stations (black triangles).

Clusters number	Time	Latitude	Longitude	Depth (Km)	Mw
20	2003139000447	35.982084	-120.545793	2.2	1.02
20	2004285062254	35.982076	-120.545801	2.2	1.14
20	2005159043055	35.982076	-120.545801	2.2	1.10
20	2005294005100	35.982080	-120.545801	2.2	1.08
20	2006218021725	35.982080	-120.545801	2.2	1.07
20	2007028170710	35.982084	-120.545801	2.2	1.04
20	2008126131756	35.982080	-120.545801	2.2	1.05
20	2008364023549	35.982080	-120.545801	2.2	1.09
20	2010293142955	35.982072	-120.545793	2.2	1.06
20	2011343093819	35.982088	-120.545776	2.2	1.00
32	2003293112543	35.982369	-120.545825	2.1	2.14
32	2004274043641	35.982361	-120.545850	2.1	2.08
32	2004343071645	35.982361	-120.545833	2.1	2.11
32	2005197033309	35.982365	-120.545833	2.1	2.12
32	2006306014022	35.982361	-120.545825	2.1	2.13
32	2008355062215	35.982353	-120.545825	2.1	2.16
32	2010327002055	35.982349	-120.545833	2.1	2.08
33	2003294090012	35.982463	-120.546216	2.3	1.90
33	2004274043449	35.982446	-120.546224	2.3	1.90
33	2004298085256	35.982430	-120.546200	2.3	1.82
33	2005023075352	35.982434	-120.546200	2.3	1.86
33	2005161114537	35.982414	-120.546175	2.3	1.64
33	2006028001751	35.982450	-120.546208	2.3	1.96
33	2007150104921	35.982418	-120.546208	2.3	1.15
33	2008354103217	35.982406	-120.546183	2.3	1.70
33	2010294003908	35.982414	-120.546191	2.3	1.50
33	2012081182758	35.982385	-120.546069	2.3	1.50

Table III.1: Repeating target events informations.

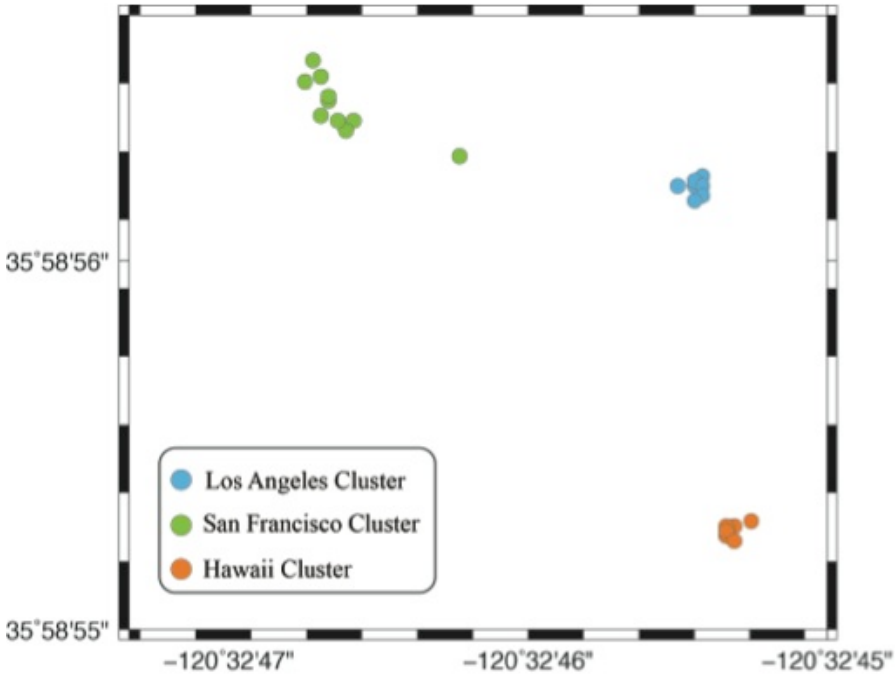

Figure III.3: Map showing the locations of three target clusters: *San Francisco, Los Angeles and Hawaii.*

III.3 Data Processing

Calculating corner frequencies can be challenging for events of small magnitudes. In attempt to resolve this, we used the coda-based source ratio methodology (Mayeda et al., 2007) and multitaper spectral estimation (Thomson, 1982; Park et al., 1987; Prieto et al., 2009) to compute spectral ratios using both direct and coda waves. With this approach we computed accurate values of the corner frequency and stress drop for the three clusters (San Francisco, Los Angeles and Hawaai) of Parkfield segment of the SAF. The multitaper spectrum algorithm was introduced by Thomson (1982) and has been applied to earthquake source spectral analysis (Abercrombie, 1995; Prieto, Thomson, et al., 2007), and it has been shown to provide unbiased and reliable spectral estimates by applying a family of orthogonal tapers, which are resistant to spectral leakage (Prieto, Parker, et al., 2007).

We also analyzed narrowband coda wave envelopes using an improved coda spectral ratio method that has significantly more narrow frequency bands and yields higher resolution spectra. Again, these methods allow one to determine the corner frequencies of the source spectra without any

assumption or correction for path and site effects by using two closely located events that will share common path and site effects. For example, as shown in Figure III.4, we formed spectral ratios between each of the San Francisco cluster events and all events of the Hawaii cluster. As observed for many other earthquakes (e.g., Mayeda and Malagnini, 2010; Yoo et al., 2010, 2011), the coda spectral ratios were very stable across the stations, with average standard deviations of less than 0.1 $\log_{10}$ units for all frequencies. The averaged S-wave spectral ratios are very consistent with the coda spectral ratios, with average standard deviations of 0.2, which is 2 times larger than the coda-ratio estimates. What is striking is the low data scatter for the coda ratios when compared against results from a conventional direct wave method (P-wave ratios in figure 6 of Yoo et al. [2010] and S-wave ratios in figure 2 of Izutani [2005]).

Assuming a single corner frequency omega-square source model (Aki, 1967; Brune, 1970), the ratio of the moment-rate functions for two closely located events recorded at the same station is given by

$$\frac{\dot{M}_1(f)}{\dot{M}_2(f)} = \frac{M_{0_1}\left[1+\left(f/f_{c_2}\right)^2\right]^{p/2}}{M_{0_2}\left[1+\left(f/f_{c_2}\right)^2\right]^{p/2}} \tag{1}$$

where M_0 is the seismic moment and f_c is the corner frequency and p is the high-frequency decay rate. The low-frequency limit the source ratio shown in Eq. 1 is proportional to the ratio of seismic moments $\left[M_{0_1}/M_{0_1}\right]$; under self-similarity, the high-frequency asymptotic value of (1) is: $\left[M_{0_1}/M_{0_1}\right]^{1-(p/3)}$. If we follow the Brune (1970) omega-square model and set p = 2, the exponent of the self-similar, high-frequency ratio becomes 1/3. Next, for each event we estimated the corner frequency and stress drop. Assuming a circular fault, the earthquake stress drop can be estimated from the seismic moment and source radius (Eshelby, 1957):

$$\Delta\sigma = \frac{7}{16}\frac{M_0}{r^3} \tag{2}$$

From Brune's model for a circular fault (Brune, 1970, 1971), the source radius r can be estimated from the corner frequency f_c,

$$r = \frac{2.34\beta}{2\pi f_c} \tag{3}$$

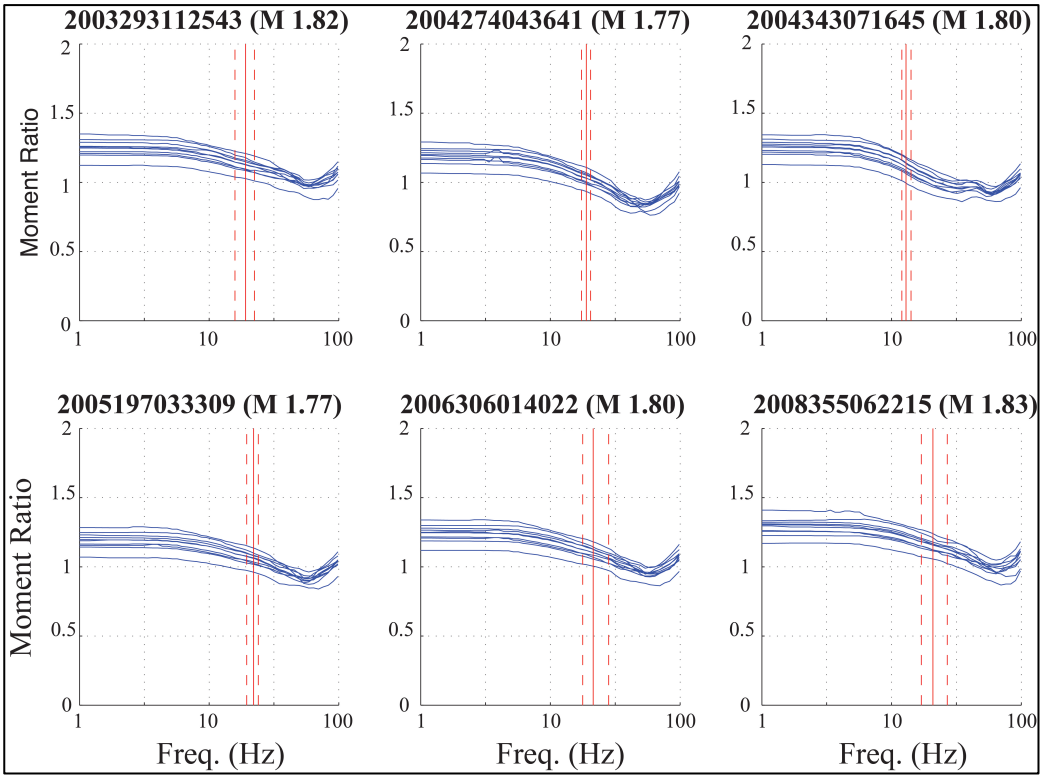

Figure III.4: the picture showing the average ratios between each of the San Francisco cluster events and all events of Hawaii cluster (blue lines). The estimates of the corner frequency average (red line) and minimum and maximum corner frequency values (dashed red lines).

First, assuming the earthquake has a flat spectral response below its corner frequency, we find the big event corner frequency (in our case we use each event of the SF cluster as a big event) using only lower frequency ratios to avoid potential bias caused by different smaller events (e.g. events of the HI cluster). When we have a corner frequency estimate for the big event from a single event pair, we use the estimate to find the corner frequency of the other small events. Then, in our case, we were able to compute the corner frequency and stress drop for each event of our target clusters (Figure III.5 and Figure III.6). We note that these stress drop estimates are in very good agreement with finite-fault estimates from Dreger et al., (2007) and Nadeau and Johnson (1998). In the Figure III.7A Dreger et al., (2007) show the slip distribution for the 2005197033309 San Francisco event obtained by inverting moment for SF, LA and HI clusters rate functions from HRSN stations. The hypocenter (white square) is in the center of the assumed rupture plane. The

dashed line shows the area used to determine the circular-fault stress drop estimates. In Figure III.7B we can se the stress drop obtained by applying the method of Ripperger and Mai (2004) to the slip model show in A). The stress drop from the simple average of the primary asperity B) is 5.3 MPa, and assuming a circular fault model and average slip it is 20.7 MPa. The simple average considering only subfaults with positive stress is 14.1 Mpa. The peak stress drop in the finite-source model is 65 MPa.

In figure III.8A Nadeau and Johnson (1988) compare the fault area and Brune stress drop from the observed corner frequency of 22.6 Hz; in B) the finite-source stress-change model is consistent with both measures, where the Brune model is more consistent with the average fom the finite-source modeling, and where Nadeau method is more consistent with the peak stress drop from the finite-surce modeling.

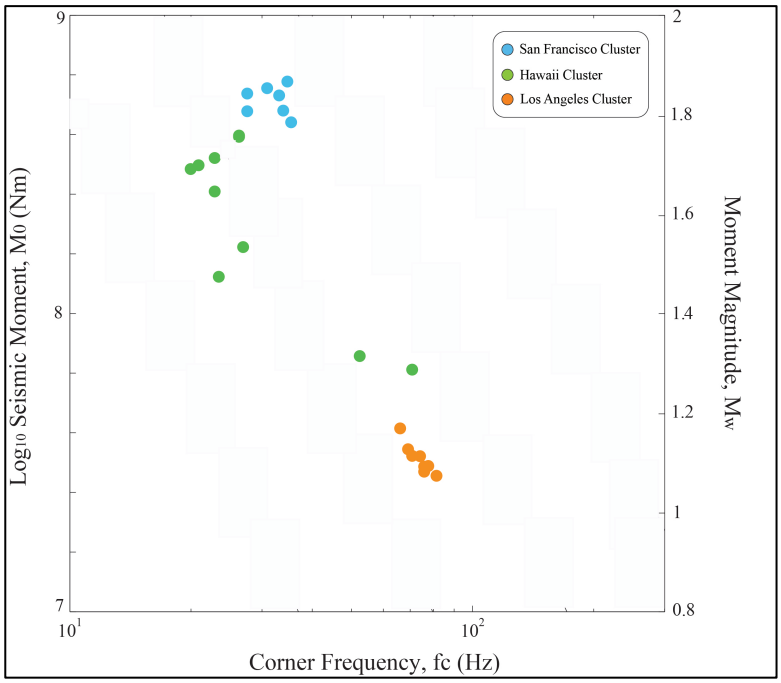

Figure III.5: the picture showing the values of corner frequency vs seismic moment for SF, LA and HI clusters.

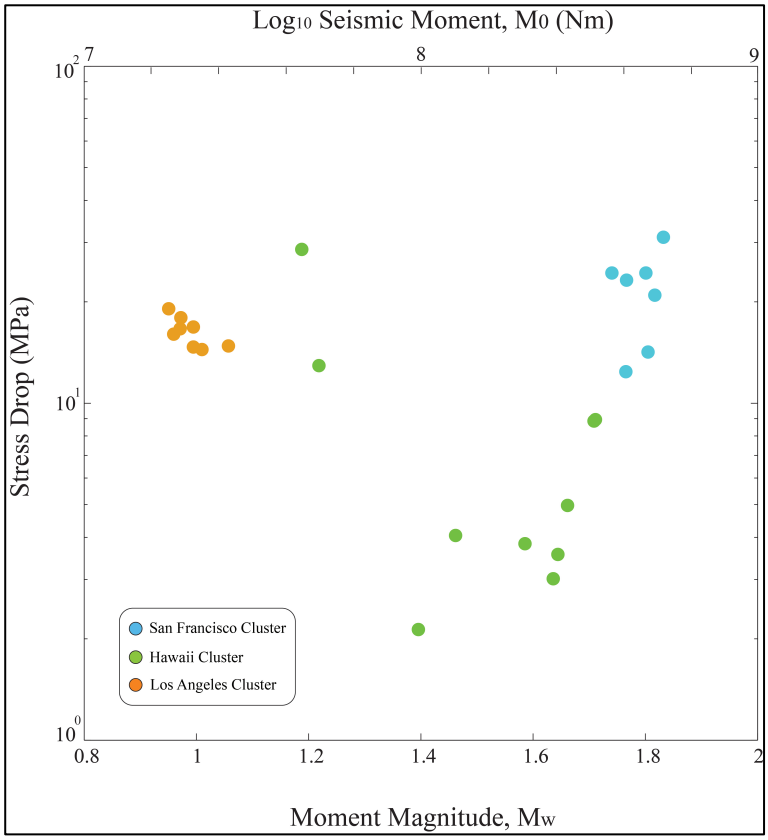

Figure III.6: the picture showing the values of Moment Magnitude vs stress drop for SF, LA and HI clusters.

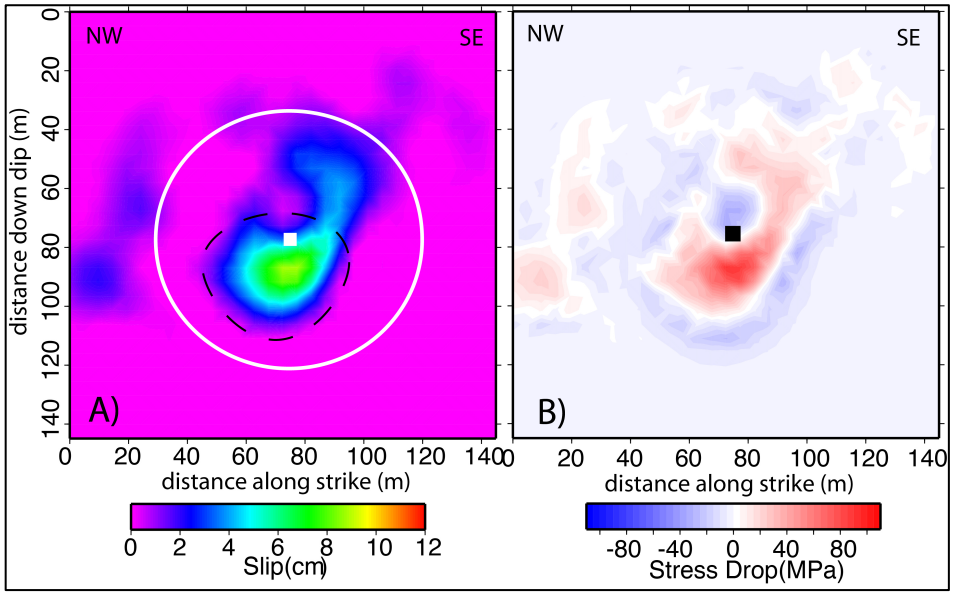

Figure III.7: A) silp distribution for 2005197033309 San Francisco event. B) stress drop obtained by applying the method of Ripperger and Mai (2004) to the slip model shown in A). (from Dreger et al., 2007).

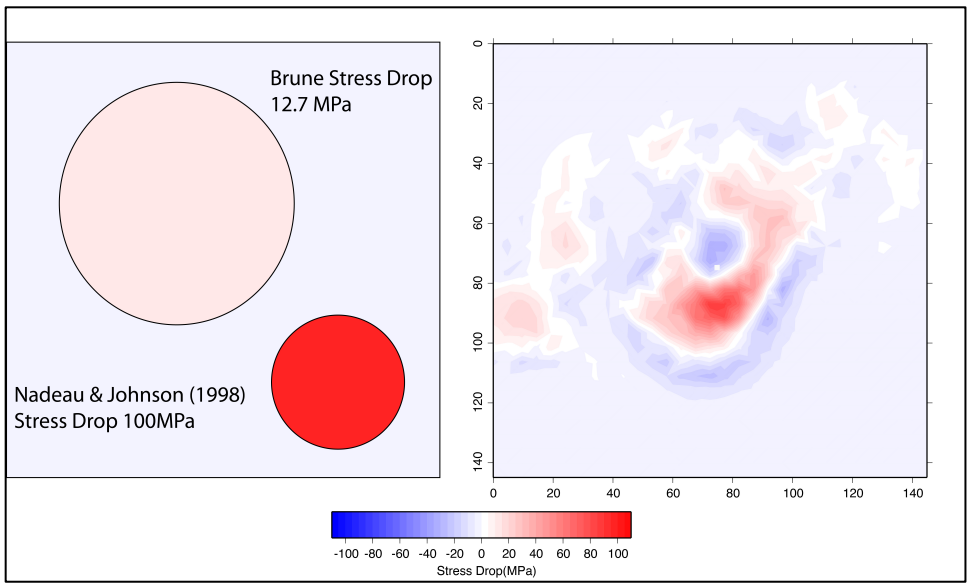

Figure III.8: A) compares the fault area and Brune stress drop. B) The finite-source stress-change model (from Nadeau and Johnson, 1998).

III.4 Moment Magnitude

Full waveform moment tensor inversion is currently a standard practice in evaluating earthquake source mechanisms. The Berkeley Seismological Laboratory (BSL) routinely performs moment tensor inversions for sizeable earthquakes in northern California (approximately $M \geq 3.5$); however the inversion method breaks down as we move down to smaller magnitude earthquakes, due to the fact that the method inverts long period waveforms. For smaller magnitude earthquakes, having a well-calibrated velocity model is important in obtaining a stable solution that generates synthetics that best fits the observed waveforms. Extensive study on the earthquakes in the Parkfield region shows that the focal mechanisms are mostly strike slip with nodal plane solutions close to the strike of the San Andreas Fault (Thurber et al., 2006).

To investigate the possibility of parameterizing micro-earthquake sources using full waveform moment tensor inversion, the BSL examined the 2004274043641 target event, shortly after the M6 mainshock. Using three borehole stations closely located to the event and well-constrained earthquake locations (Dreger et al., 2007), they obtained a solution that is stable in terms of inverting for well-constrained nodal plane orientation and scalar seismic moment. The obtained

M_w for this event is 1.76 as shown in Figure III.9. We used this value of magnitude as a reference magnitude in the spectral analysis only for our target cluster (Figure III.10).

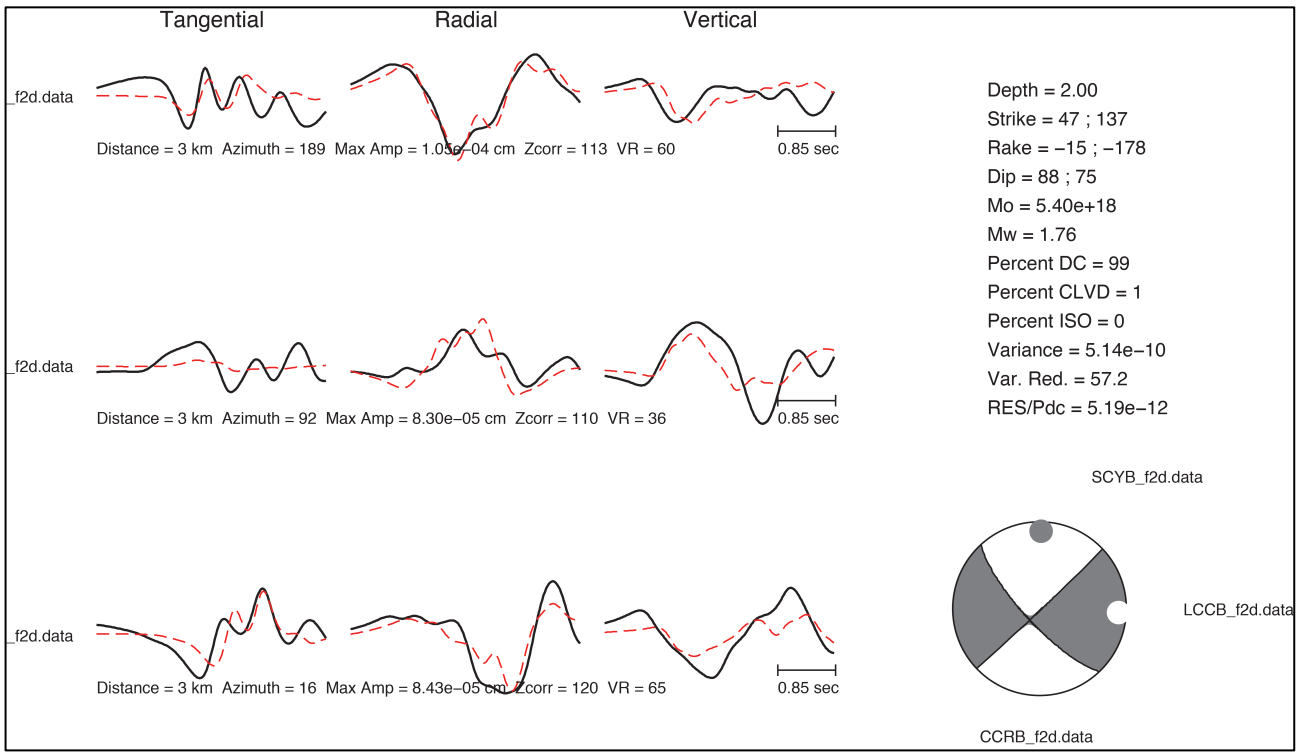

Figure III.9: the moment tensor solution for the 2004274043641 event.

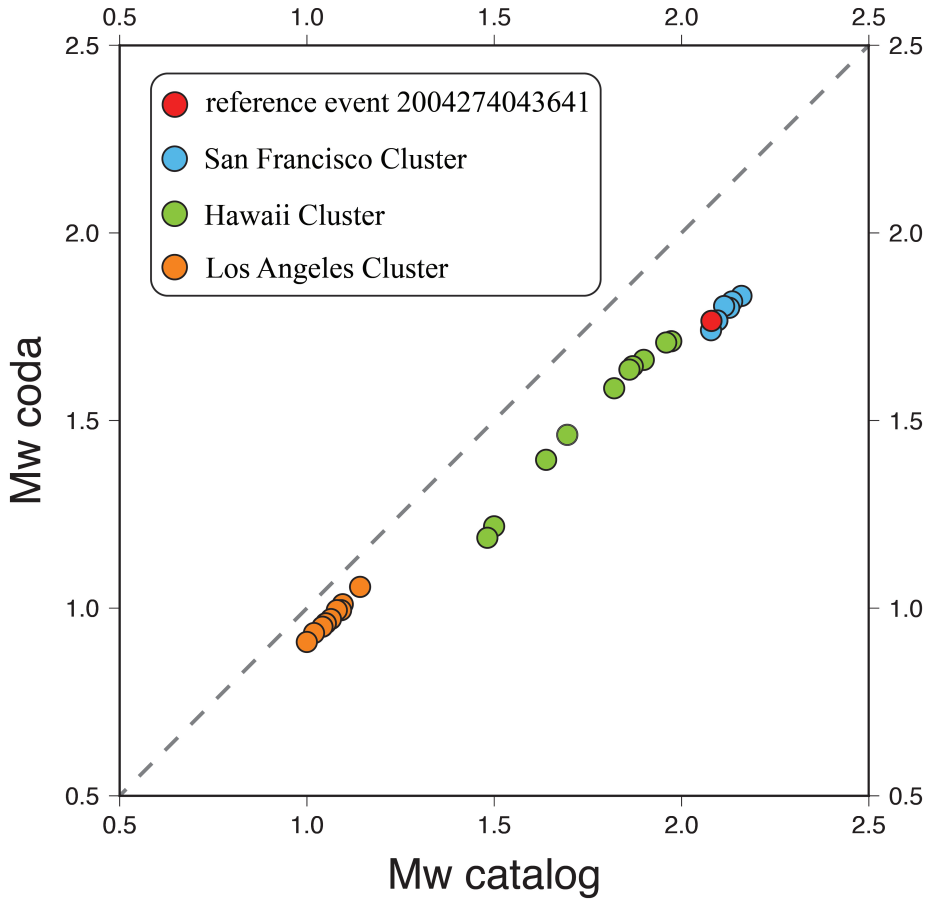

Figure III.10: Mw catalog from R.M. Nadeau (BSL) vs coda-derived moment magnitude. The red circle is the moment of the reference event which was used as a reference magnitude in the spectral analysis.

III.5 Ground Motion Scaling

We will use the same methodology for data processing and analysis as was successfully used in studies with data sets from Italy (Malagnini et al., 2000a, 2002; Morasca et al., 2006; Scognamiglio et al., 2005), Central Europe (Malagnini et al., 2000b; Bay et al., 2003) and from Utah and Yellowstone (Jeon et al., 2004). The technique consists of four stages: i) removal of the instrument response; ii) multiple filtering; iii) general regression and iiii) forward modeling.

In order to obtain the scaling relationships for the ground motion in the Parkfield area, regressions are carried out from 757 repeating micro-earthquakes with magnitude ranging from $M_w \simeq 0$ to M_w

≃ 2. The digital data are corrected for instrument response to actual ground motion, and the peak ground velocities are measured in selected narrow-frequency bands, between 1 and 67 Hz.

Ground motion attenuation with distance (Figure III.11) and the variation of excitation with magnitude are parameterized for this area to define a consistent model (Table III.2) that describes peak ground motion.

Regression results for peak velocities are used to define a piecewise linear (in loglog) continuous geometrical spreading function, a frequency-dependent attenuation paramenter Q (*f*), and a distance-and-frequency-dependent duration function.

A general form for a predictive relationship for observed ground motion may be written as:

$$AMP(f_i, r_{jk}) = SRC_j(f_i, r_{ref}) + SITE_k(f_i) + D(r_{jk}, r_{ref}, f_i) \quad (4)$$

where $AMP(f_i) = log_{10}$ amp(fi) represent the logarithm of peak amplitude observed, in the time domain, on a narrow bandpass-filtered version of the n-th time history, SRC_j (f_i, r_{ref}) is the excitation term for the ground motion at an arbitrary reference hypocentral distance r_{ref}, $SITE_k$ (f_i) represents the distortion of the seismic spectra induced by the shallow geology at the recording site, the propagation term is indicated as D (r_{jk}, r_{ref}, f_i) and represents an estimate of the average crustal response for the region at the hypocentral distance r_{ref}, at the central frequency f_i.

In the loglog space, D (r, r_{ref}, f) is determined as a piecewise linear function (Yazd, 1993; Anderson and Lei, 1994; Harmsen, 1997), allowing to consider complex behavior of the regional attenuation. Finally, r_{ref} is an arbitrary hypocentral distance at which all source terms are referred (6 Km); this is achieved by forcing the coinstraint D $(r_{jk}, r_{ref}, f_i) = 0$ to the i-th regression (e.g. see Malagnini et al., 2000).

Given a stationary, random time history of length T', the Random Vibration Theory (RVT, see Cartwright and Longuet-Higgins, 1956; see Appendix A for details) may be used to estimate its peak value: $Peak\ (a(t)) \approx \eta aRMS$, where the aRMS is its RMS-average calculated over T' and $\eta\ (m0, m2, m4)$ is a function of the specifies spectral moments of the filtered time history. The RVT model has been shown (Boore, 1983) to be quite robust in predicting the standard engineering ground-motions. The quantification of an effective duration of the seismograms as a function of hypocentral distance and frequency is critical for a correct use of RVT, and the reader is referred to Raoof et al., (1999) and to Malagnini (1999) for a thorough discussion on this aspect of the technique. The Parseval and the convolution theorems, together with the RVT, can be used

to completely switch from peak values in the time domain to Fourier spectral amplitudes. Equation (4) is solved in the time domain, from multiple narrow band-pass signals.

Due to the constraints applied to the system prior to the regressions, the excitation term represents the expected peak ground motion at the reference distance, as it would be observed at a site representative of the average site response of the network. We also use the crustal attenuation parameter

$$Q(f) = 80 f^{0.16} \tag{5}$$

Also two parameters are used to predict shapes and levels of the seismic spectra, the Brune's stress drop $\Delta\sigma$, and a high-frequency attenuation parameter κ = 0.015 sec (see Anderson and Hough, 1984).

Comparisons can be done among different zones in which this kind of studies have been conducted. It has been found that the western Alps (Morasca et al., 2006), eastern Alps (Malagnini et al., 2002), Southern Appenines, central Italy (Malagnini et al 2000a), eastern Sicily (Scognaniglio et al 2005), Central Europe (Malagnini et al., 2000b; Bay et al., 2003), Utah e Yellowstone (Jeon et al., 2004), and Parkfield region (this work) have different characteristics for the attenuation parameters because the combination of the geometrical spreading function and the parameter Q (f) is strictly related to the crustal characteristics.

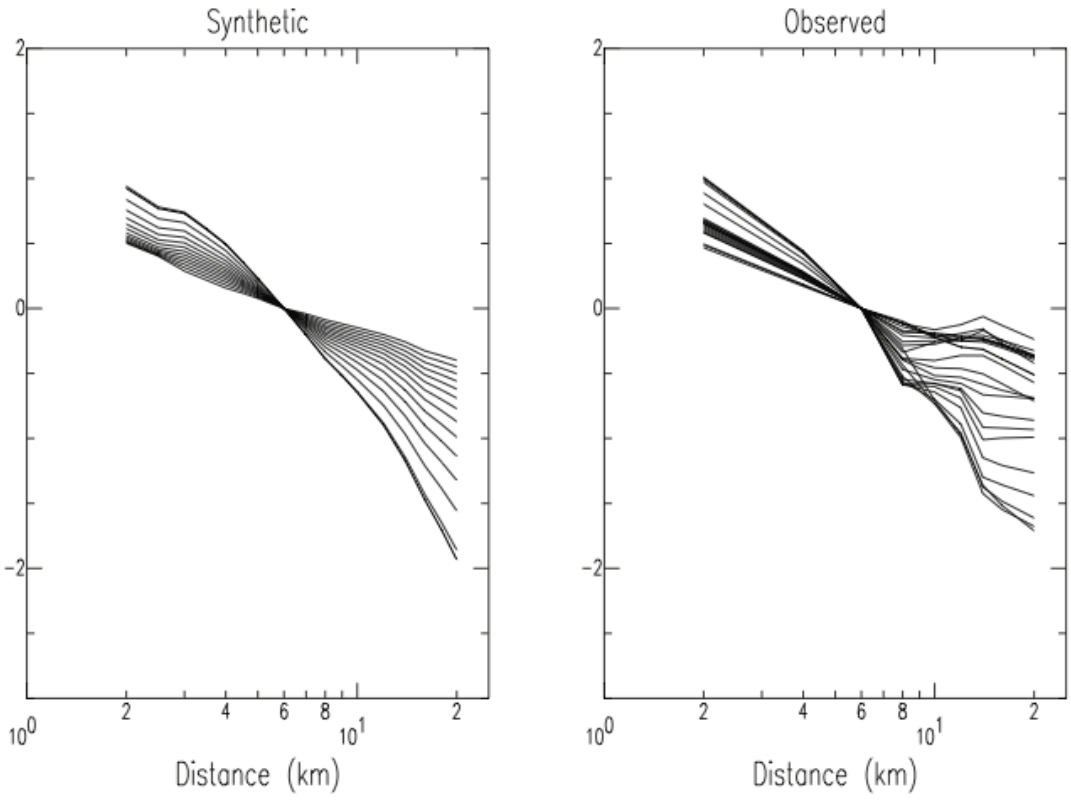

Figure III.11: The regional attenuation functional $D\ (r, r_{ref}, f)$ obtained for the Parkfield area from the regression on the peak values is shown at the sampling frequencies between 1 Hz (shallowest) and 67 Hz (steepest). Frequencies are equally spaced logatithmically. The attenuation function is normalized to zero at the reference hypocentral distance of 6 km.

$k = 0.015$ (sec)	$Q(f) = 80\, f^{0,16}$
$g(r) = r^{-1.1}$ $r < 10$ km	$g(r) \propto r^{-0.1}$ $r \geq 10$ km
M_w	**$\Delta\sigma$ (MPa)**
0.0	2
0.4	5
0.8	10
1.2	15
1.6	18
2.0	25

Table III.2: In this model of crustal attenuation we use to predict shapes and level of the seismic spectra: ***g(r)***=body-wave geometrical spreading; ***Q(f)***=crustal attenuation parameter; ***Δσ***=stress drop (different values calibrated on cluster 32); ***k***=residual systematic attenuation parameter relative to the average reference site of the network (calculated on stations CCRB, VARB, VCAB).

The Figure III.12 compare the observed and predicted excitation of filtered velocity spectra obtained from the Parkfield segment of the SAF. In particular the figure shows the spectra relative to clusters 08, 13, 15, 20, 23, 24, 25, 32, 33, 40 at the reference hypocentral distance (6 Km). Theoretical red curves are obtained using a body-wave geometrical spreading, a crustal attenuation parameter, and a non self-similar source scaling. The black lines indicate the regression result, and the red thick lines denote the theoretical prediction at the indicated levels of moment magnitude. Table III.2 provide the parameters of our working model.

We noted that several clusters contain events whose Mw's are bi-modally distributed (e.g. Cluster 15, 33, 40). This characteristic may suggest a time-dependent behavior, consistently with the idea of Rubinstein and Ellsworth (2009), and of Chen et al., (2010). Rubinstein and Ellsworth analyzed a subset of 29 repeating earthquake from 1984 to 2005 at Parkfield, and noted a small change in the magnitude distribution of the events following the Parkfield earthquake: events appear to get larger following the Parkfield main shock. Specifically, they determined the relative amplitude (moment) to compute a final estimate of relative moment. Chen et al. analyzed a subset of repeating earthquake from 1987 to 2009 at Parkfield to examine the variation of their recurrence properties in space and time. Following the main shock, many of the repeating events have greatly reduced recurrence intervals that systematically increase with time. In addition to this change in timing, they also found systematic changes in seismic moment (immediate increase and subsequent decay) determined calculating spectra for 0.5 (P) and 1.0 (S) second time windows to obtain a consistent network-averaged spectral ratio for each event.

The SAF separates two very different but relatively homogeneous crustal structures (Li et al., 2004), for this reason we decided to split our data set in two: the North America (NA) and the Pacific America (PA) sides of the SAF. Results shown in Figure III.13 are from the NA data set, but totally equivalent results were obtained also for the PA side of the SAF. In this Figure we can observe that the spectral amplitudes of earthquakes occurred after the Parkfield main shock are larger and the variations in moments, as mentioned above, are described in detail in Rubinstein and Ellsworth (2009), and in Chen et al., (2010).

Taira et al., 2009 identified long-term changes in fault strength induced by large seismic events, namely the 2004 M_w 9.1 Sumatra-Andaman earthquake. The change possessed two manifestations: temporal variations in the properties of seismic scatterers (probably reflecting the stress-induced migration of fluids) and systematic temporal variations in the characteristic of repeating-earthquake sequence that are most consistent with changes in fault strength. For this reasons, we removed all the event occurred after Sumatra (Figure III.13).

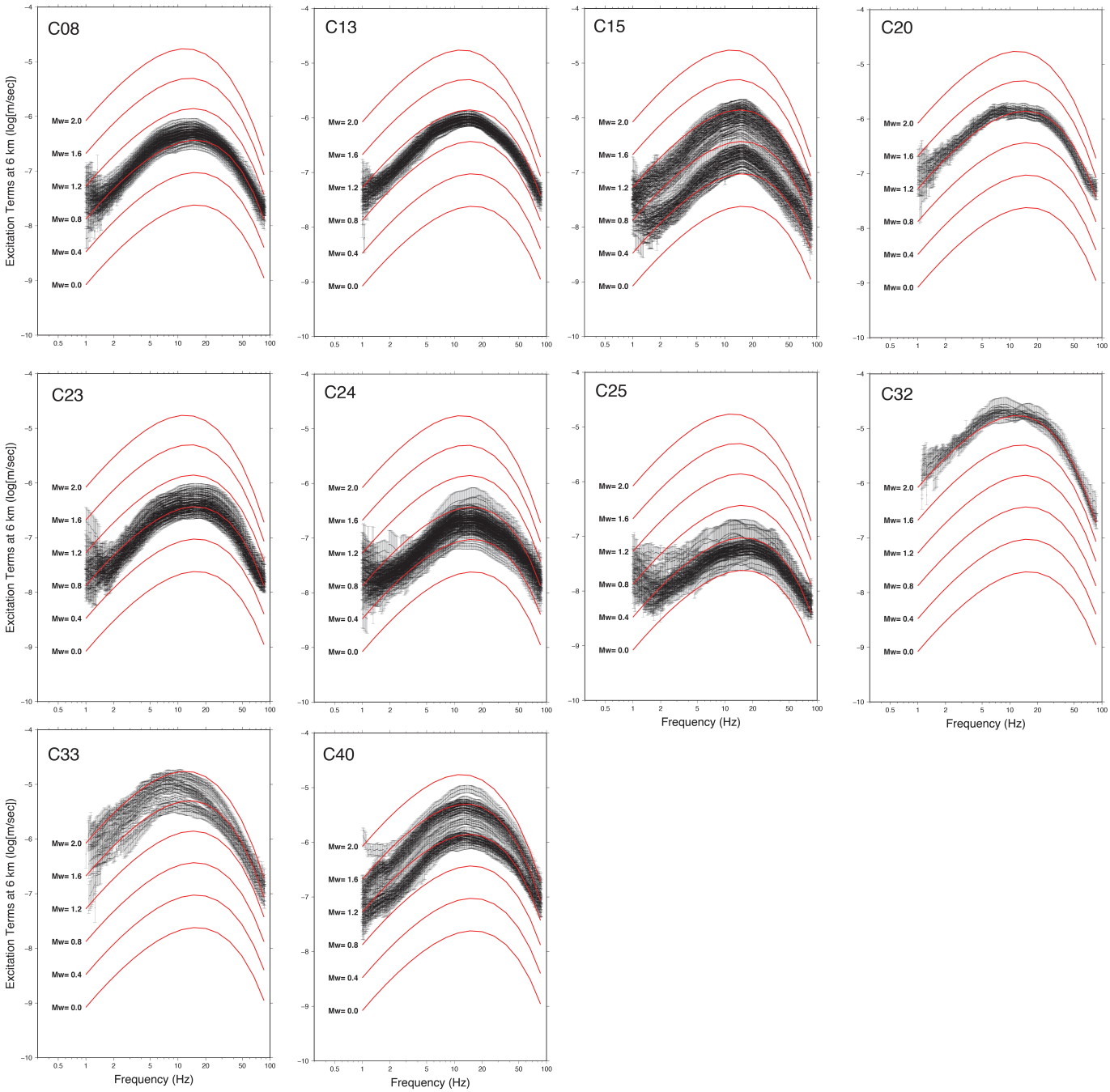

Figure III.12: Filtered ground velocity excitation terms relative to the cluster 08, 13, 15, 20, 23, 24, 25, 32, 33, and 40 (black lines). Red thick lines indicate the theoretical prediction at the indicated levels of moment magnitude.

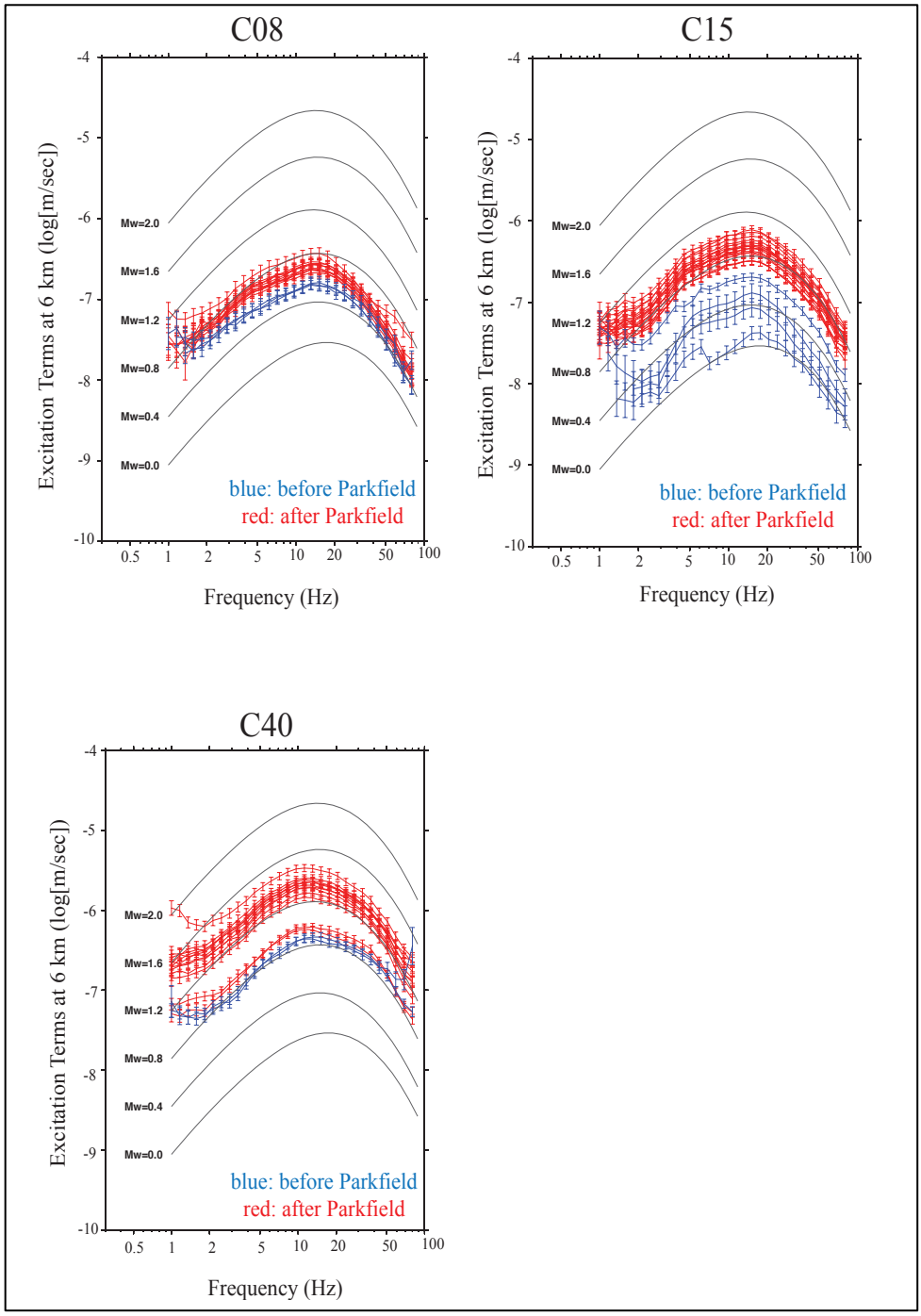

Figure III.13: spectral amplitudes of earthquakes occurred after the Parkfield main shock relative to the cluster 08, 15, and 40. Black lines indicate the theoretical prediction at the indicated levels of moment magnitude; blue lines indicate the events occurred before the Parkfield main shock and the red lines indicate the events occurred after the Parkfield main shock.

Figure III.14 shows the site terms obtained from the regression on the peak amplitudes. Given the constraint

$$\sum_i SITE_i(f) = 0 \tag{6}$$

$$D\,(r = r_{ref}, f_i) = 0 \tag{7}$$

the individual site terms shown in the Figure III.14 represents the deviation of the specific site from the network average. The constraints given by (6) and (7) are necessary, in order to reduce the degrees of freedom of the system prior to the inversion. Moreover, by forcing the conditions (6) and (7) we give a precise physical meaning to the excitation terms, since they now represent what would be recorded at the reference hypocentral distance by the average network site.

To give an example, if we knew the absolute site term at a specific station at all frequencies, we could have forced the corresponding term in the inversion to be equal to the known site response. In such a case, the excitation terms would have represented the peak spectra of the events, as they would have been recorded at the specific site, with all events located at the reference hypocentral distance.

Figure III.14 shows that there are large fluctuations from the network average at the various frequencies. No detailed information about the site geology is available at each seismometric location, although we know that all of them were deployed on rock outcrops. For this reason we expect the constraint forced on the site terms to result in a relatively small bias on the inverted source terms, and thus our model predicts the expected rock outcrop motion in the region

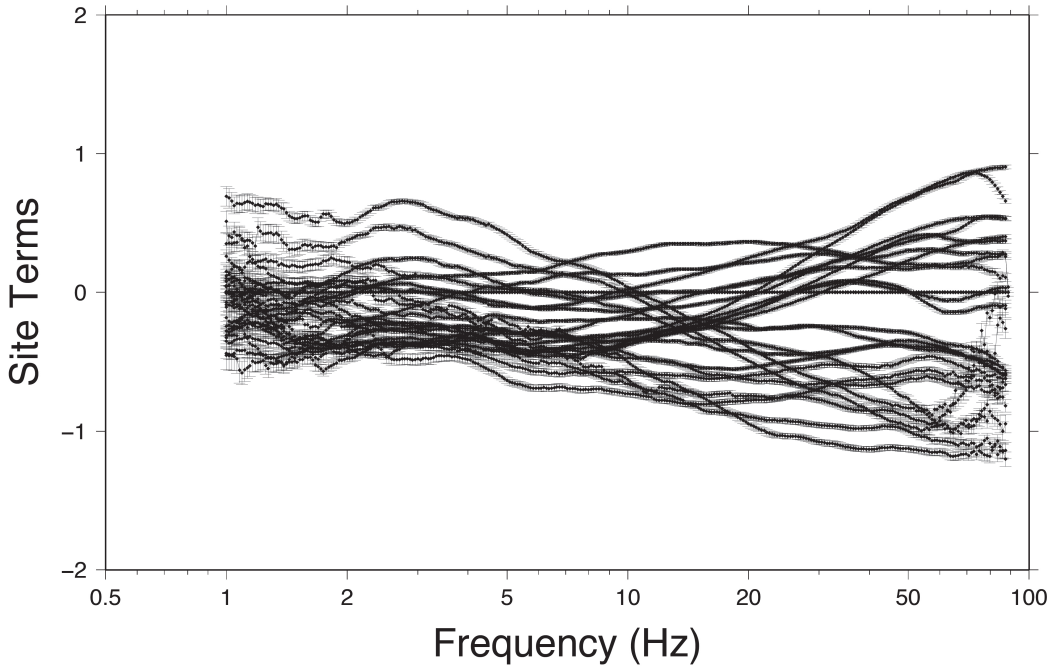

Figure III.14: Inverted site terms for the Parkfield data set. The figure shows thaht the network average at the various frequencies are far from being flat.

We were able to calculate accurate M_0 values for all event of our data set; we did this in two different ways: i) Figure III.15 shows M_W catalog (from R. M. Nadeau, Berkeley Seismological Laboratory) versus M_W from waveforms. Spectral corrections are calculated on the spectra of the single waveform (through a MACRO SAC). We computed the average and evaluated the spectral plateau. A critical part of this calculation is remove the micro-seismic noise; the paradox is represented by the fact that the greater magnitude are worse, we should therefore enhance the use of the high pass filter; ii) in order to improve the values calculated above, we do a series of regressions with the Fast Fourier Transform (FFT) technique. In our case we selected the twenty biggest events to compute Amp_{RMS} in a range of 3-10 Hz to obtain M_0 values. We apply a correction for *g (r)* and *Q* (see Table III.2). Then we do the same procedure on Peak values and we compute the ratios with the twenty selected event to obtain M_0 value for all our data set (Figure III.13).

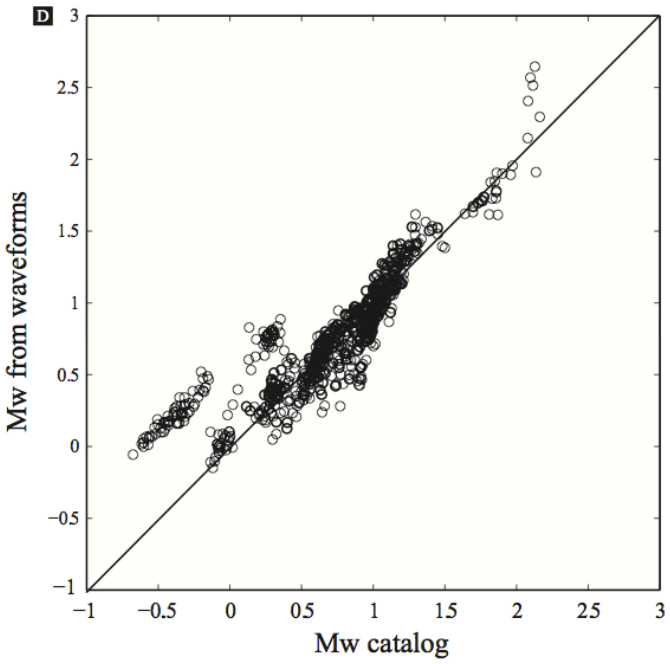

Figure III.15: Mw catalog vs Mw from waveform. It shows the Mw of all events that corrects for the observed attenuation (anelastic and geometric).

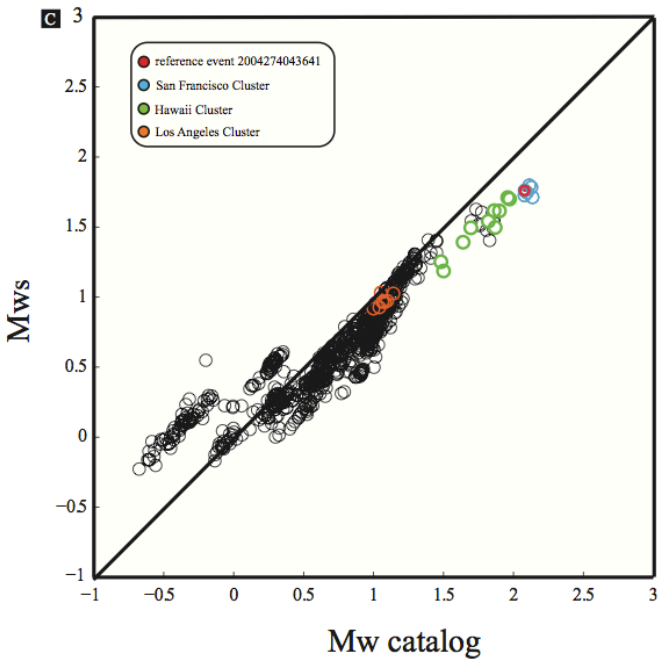

Figure III.16: Mw catalog vs Mw_S(spectral ratio). It shows the Mw of events that were calculated by spectral ratio between the reference event (Mw 1.76, red circle).

For some clusters (08, 15, 28, 29, and 40) we show the seismic moment as a function of time. We observe different behaviors: for example, on the cluster 15, we note the transient induced by Parkfield main event. It is clear, in fact, that the amplitude of anomaly decrease with time and the recurrence time of repeaters increase away from perturbation. On the cluster 08, instead, we observe the smoother response to perturbation even if the fluctuation could be within of the standard errors. It is also interesting to observe, on the cluster 15, 28, 29, and 40 a dynamic effect possibly induced by the 2004 M_w 9.1 Sumatra earthquake stress waves (Taira et al., 2009).

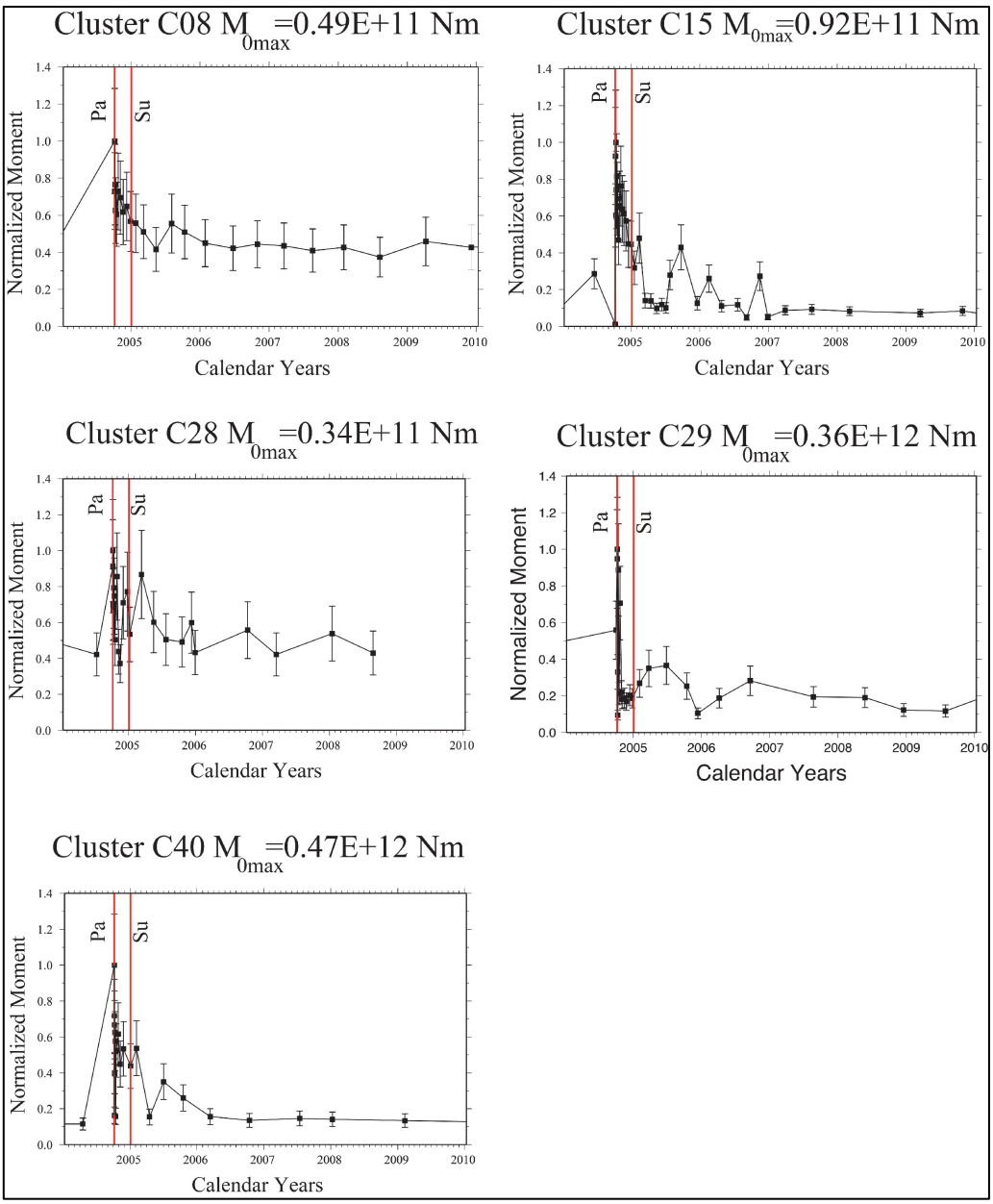

Figure III.17: Seismic Moment as a function of time for the cluster 08, 15, 28, 29, and 40. Pa= Parkfield main event, Su= Sumatra main event.

III.6 Conclusions

The seismological data acquired by the HRSN at Parkfield over the past 10 years provides a valuable resource for the study of earthquake source mechanics. The present study takes advantage of the large number of repeating sequences of micro-earthquakes in a relatively short period of time (from 2002 to 2012), and this allows a fairly complete characterization of the sequences. The observational data analyzed contain some interesting implications for our understanding of the earthquake process. In this study, we analyzed a data set acquired by HRSN, installed to monitor the repeating micro-earthquakes, to validate the analysis procedure. This data set provided a unique opportunity to quantify earthquake ground motion due to the quality and quantity of observations. From analysis of 757 earthquakes along the Parkfield segment of the San Andreas fault, we conclude the following:

i) we computed source corner frequency and stress drop using multi-taper spectral analysis of P and S waves (Yoo et al., 2012), an improve of coda method (Mayeda et al., 2007);

ii) corner frequency for the SF, LA, and HI target clusters are high (approx. 20 – 80 Hz), resulting in high stress drops (~1.5 to 20 MPa). High stress drop estimates are consistent with those by Nadeau and Johnson (1998) and Dreger et al. (2007), indicating that high strength patches exist on the Parkfield segment of the San Andreas fault;

iii) similar values of stress drop are obtained at least for the 10 clusters shown here, indicating that it may be general characteristic of all repeaters;

iv) several clusters contain events whose Mw's are bi-modally distributed (e.g. Cluster 15, 33, 40), we can explain this with a time dependent behavior consistent with Rubinstein and Ellsworth, (2009), and Chen et al., (2010);

v) the two events with the lowest stress drops in the SF cluster occurred in 2004 and 2005 and followed the 2003 first event in the SF cluster, suggesting a time dependent behavior for the corner frequencies (and therefore stress drops), consistently with the idea of transient fault damage, healing, and modulation of high frequency radiation through healing (McLaskey et al., 2012; Vidale et al., 1994);

vi) the stress drop parameter seems to be spatially homogeneous over the clusters sampled in this study, and to smoothly increase with increasing magnitude;

vii) site terms of most 264 borehole sensors are far from being flat. The analysis of ground motion was done using a two-step modeling procedure: i) a regression was performed to characterize source duration and excitation, source-receiver distance dependence, and station site effects; ii) a

point-source forward model is constructed in terms of geometrical spreading, observed duration, site effects, and source scaling, in order to match the regression results. A proper description of ground motion scaling requires presenting enough information to duplicate the observations. This means that, until definitive information will be available on source scaling and absolute site effects, $Q(f)$ cannot be presented without being coupled to $g(r)$ and κ ; iii) we also calculated an accurate moment megnitudes for most of the 757 events of our data set, between $M_W \sim 0$ and $M_W \sim 1.9$.

Abstract

Evaluation and prediction of strong ground motions is of fundamental importance to determine the input motions for seismic design of structures. In the frequency domain, ground motions may be quantified by summing three terms, namely: source, path, and site terms, as shown in Figure IV.1. Among these, the site term represents the influence of sediments on the ground motions and it includes the two competing effects due to shallow impedance contrasts (amplification), and to the anelastic attenuation (high-frequency attenuation). In this study, we study the ground motions generated by subduction-zone earthquakes occurred in Chile. For subduction-zone earthquakes, simple characteristic source models are newly developed and used.

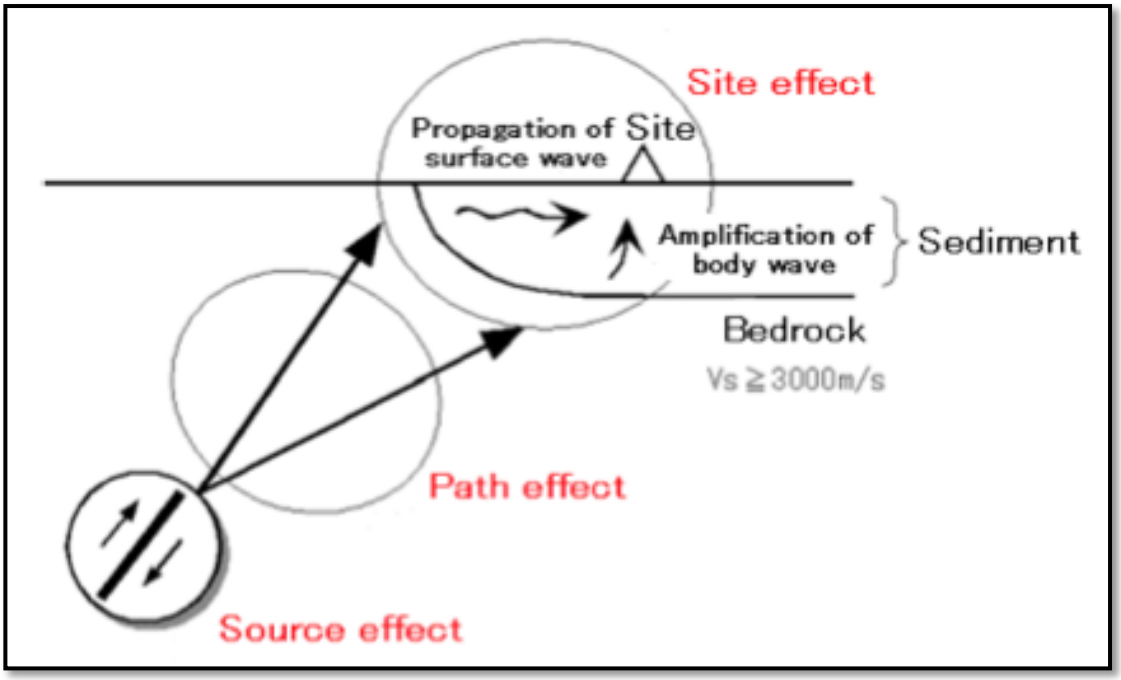

Figure IV.1: The source, path and site effects.

IV Characteristics of high frequency ground motions in the Maule region (Chile), obtained from aftershocks of the 2010 Mw 8.8 earthquake.

IV.1 Introduction

The M_w 8.8 Maule earthquake occurred about 3 km off the coast of the central Chile on 2010 February 27 at 03:34 local time (06:34 UTC) with intense shaking lasting for about three minutes and it was followed by thousands of aftershocks. The earthquake took place along the boundary between the Nazca and South American tectonic plates, at the location where the Nazca plate is subducting beneath the South America tectonic plate at a rate of about 74 mm/yr.

The subduction zone event caused severe ground shaking across a 660 km swath of the country and generated a tsunami that ravaged the coastline. Chile is located on a convergent plate boundary that generates mega-thrust earthquake since the Paleozoic era (500 million years ago). In fact, based on the historical record, the Chilean coast has suffered many mega-thrust earthquakes along this plate boundary, including the strongest earthquake ever measured (1960 Valdivia earthquake, M 9.5). The segment of the fault zone that ruptured in this earthquake was estimated to be over 700 km long with a displacement of almost 10 meters. It lays immediately north of the 1000 km segment that ruptured in the great earthquake of 1960.

This study uses a data set consisting of 172 aftershocks of the M_w 8.8 Maule earthquake recorded by more than 100 temporary broadband stations deployed between March 2010 and January 2011. (Figure IV.2). Each of these earthquakes use the relocations performed for National Earthquake Information Center (NEIC) and is characterized by a well-constrained focal mechanism and moment magnitudes in the range M_w 3.7 to 6.2. The RMTs were determined using the WUS velocity model (Herrmann et al., 2011a). Most of these earthquakes are characterized by shallow (Figure IV.3), eastward-dipping, thrust-type focal mechanisms consistent with faulting at or near the plate interface.

The aim of this work is to quantitatively describe the high-frequency ground motion in Chile. To accomplish this task, regressions are performed over large data sets covering a wide range of earthquake sizes and hypocentral distances.

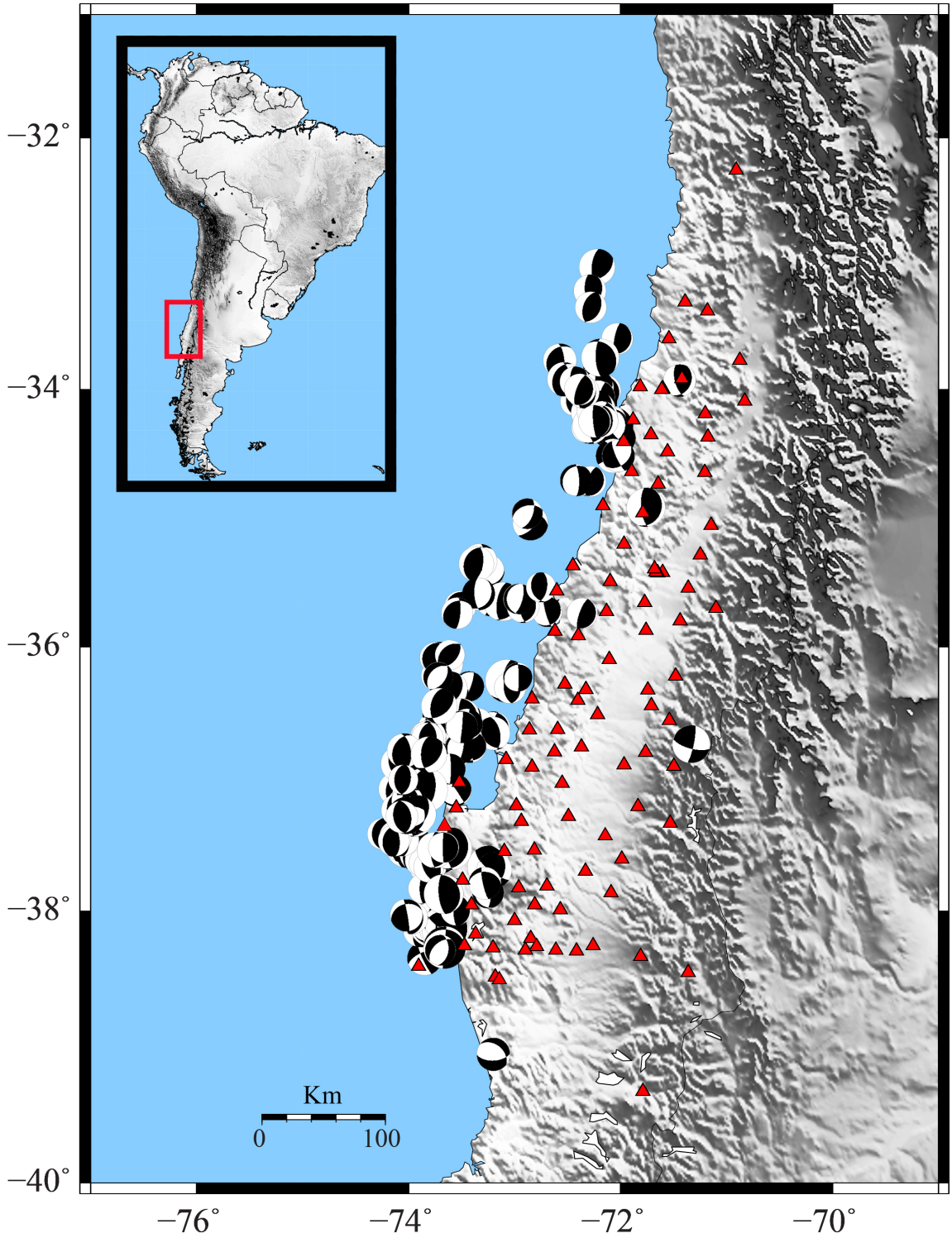

Figure IV.2: Map of the Maule region (Chile). Beach balls indicate the moment tensor solutions of all 172 aftershock in the range M_w 3.7 to 6.2. Red triangles indicate the positions of the 100 temporary broadband seismic stations used in this study.

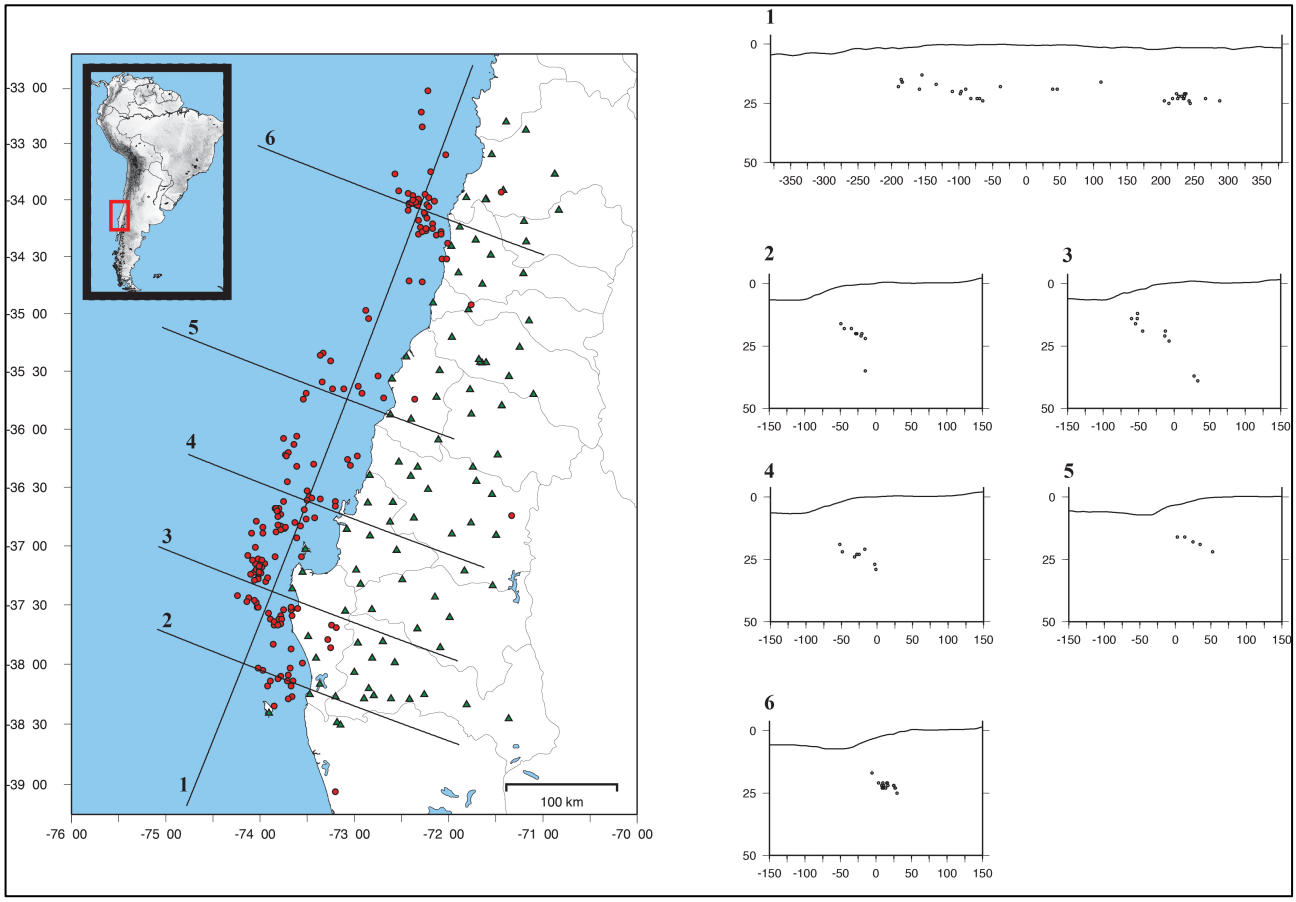

Figure IV.3: a) Cross-section (1-6) of subduction zone showing the area constrained in this work. b) Earthquake locations (red circles) and stations (green triangles) are shown.

IV.2 Data Processing

We will use the same methodology for data processing and analysis as was successfully used in studies with data sets from Italy (Malagnini et al., 2000a, 2002; Morasca et al., 2006; Scognamiglio et al., 2005), Central Europe (Malagnini et al., 2000b; Bay et al., 2003) and from Utah and Yellowstone (Jeon et al., 2004). The technique consists of four major stages: i) removal of the instrument response; ii) multiple filtering; iii) general regression and iiii) forward modeling.

In order to obtain the scaling relationships for the high-frequency ground motion in the Maule region (Chile), regressions are carried out from 172 regional aftershocks with magnitude ranging from $M_w \simeq 3.7$ to $M_w = 6.2$. The digital data are corrected for instrument response to actual ground

motion, and the peak ground velocities are measured in selected narrow-frequency bands, between 0.2 and 30 Hz.

Ground motion attenuation with distance (Figure IV.4) and the variation of excitation with magnitude are parameterized for this area to define a consistent model (Table IV.1) that describes peak ground motion.

Regression results for peak velocities are used to define a piecewise linear (in loglog) continuous geometrical spreading function, a frequency-dependent attenuation paramenter Q (*f*), and a distance-and-frequency-dependent duration function.

A general form for a predictive relationship for observed ground motion may be written as:

$$AMP(f_i, r_{jk}) = SRC_j(f_i, r_{ref}) + SITE_k(f_i) + D(r_{jk}, r_{ref}, f_i) \quad \text{(IV.1)}$$

where $AMP(f_i) = log_{10}$ amp(fi) represent the logarithm of peak amplitude observed, in the time domain, on a narrow bandpass-filtered version of the n-th time history, SRC_j (f_i, r_{ref}) is the excitation term for the ground motion at an arbitrary reference hypocentral distance r_{ref}, $SITE_k$ (f_i) represents the distortion of the seismic spectra induced by the shallow geology at the recording site, the propagation term is indicated as D (r_{jk}, r_{ref}, f_i) and represents an estimate of the average crustal response for the region at the hypocentral distance r_{ref}, at the central frequency f_i. In the loglog space, it is determined as a piecewise linear function (Yazd, 1993; Anderson and Lei, 1994; Harmsen, 1997), allowing to consider complex behavior of the regional attenuation. Finally, r_{ref} is an arbitrary hypocentral distance at which all source terms are referred (40 Km); this is achieved by forcing the coinstraint D $(r_{jk}, r_{ref}, f_i) = 0$ to the i-th regression (e.g. see Malagnini et al., 2000). Given a stationary, random time history of length T', the Random Vibration Theory (RVT, see Cartwright and Longuet-Higgins, 1956; see Appendix A for details) may be used to estimate its peak value: $Peak\ (a(t)) \approx \eta aRMS$, where the aRMS is its RMS-average calculated over T' and $\eta\ (m0, m2, m4)$ is a function of the specifies spectral moments of the filtered time history. The RVT model has been shown (Boore, 1983) to be quite robust in predicting the standard engineering ground-motion parameters. The quantification of an effective duration of the seismograms as a function of hypocentral distance and frequency is critical for a correct use of RVT, and the reader is referred to Raoof et al., (1999) and to Malagnini (1999) for a thorough discussion on this aspect of the technique. The Parseval and the convolution theorems, together with the RVT, can be used to completely switch from peak values in the time domain to Fourier spectral amplitudes. Equation (IV.1) is solved in the time domain, from multiple narrow band-pass signals.

Due to the constraints applied to the system prior to the regressions, the excitation term represents the expected peak ground motion at the reference distance, as it would be observed at a site representative of the average site response of the network. We also use the crustal attenuation parameter

$$Q(f) = 200 f^{0.5} \qquad \text{(IV.2)}$$

The quality factor given in (IV.2), and coupled with a geometrical spreading $g(r)$, is consistent with the results described by Garcia et al. (2004), who found: $Q(f) = 251 f^{0.58}$.

Also two parameters are used to predict shapes and levels of the seismic spectra, the Brune's stress drop $\Delta\sigma$, and a high-frequency attenuation parameter $\kappa = 0.030$ sec (see Anderson and Hough, 1984).

Comparisons can be done among different zones in which this kind of studies have been conducted. It has been found that the western Alps (Morasca et al., 2006), eastern Alps (Malagnini et al., 2002), Southern Appenines, central Italy (Malagnini et al 2000a), eastern Sicily (Scognaniglio et al 2005), Central Europe (Malagnini et al., 2000b; Bay et al., 2003), Utah e Yellowstone (Jeon et al., 2004), and Chile region (this work) have different characteristics for the attenuation parameters because the combination of the geometrical spreading function and the parameter $Q(f)$ is strictly related to the crustal characteristics.

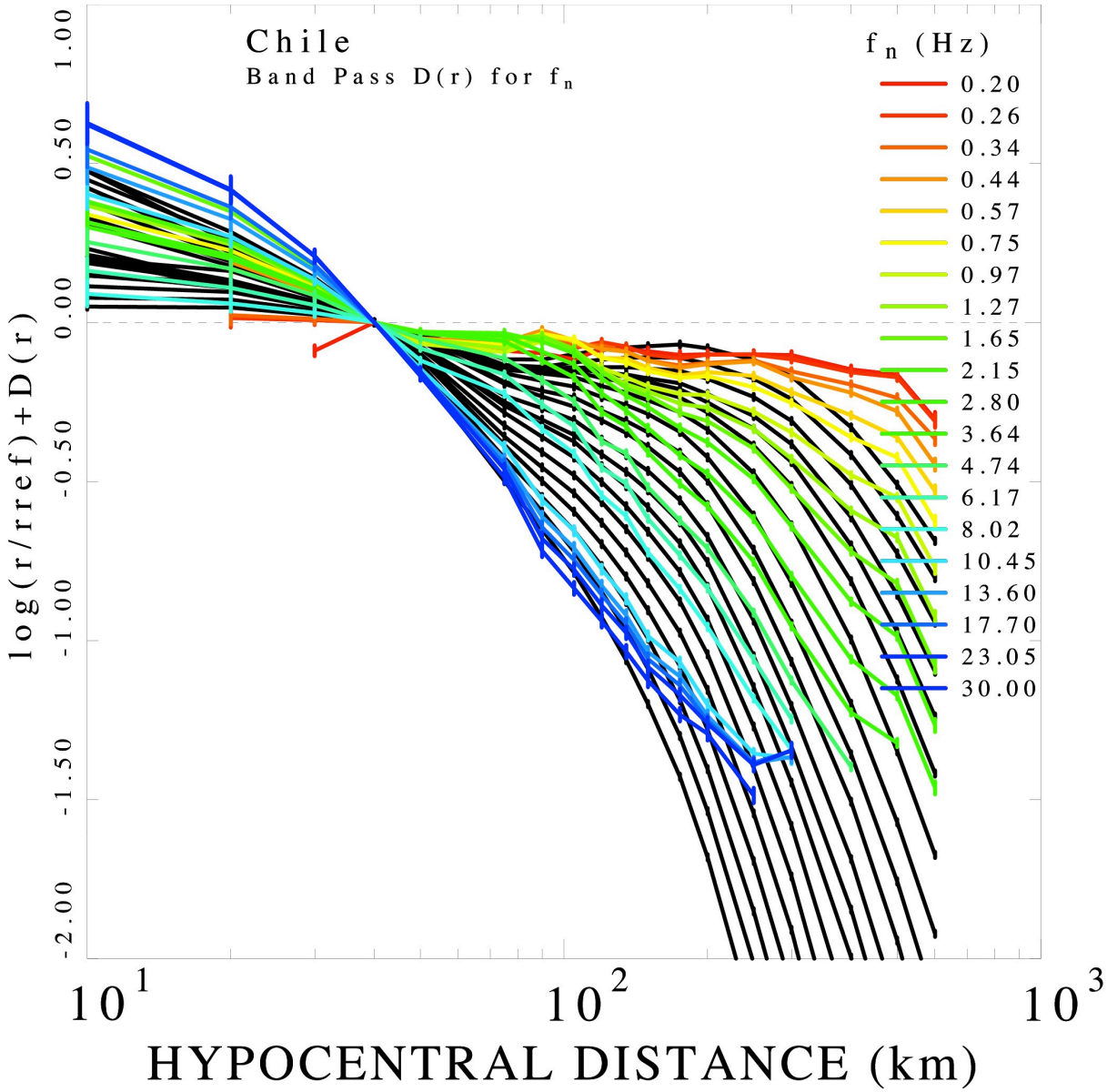

Figure IV.4: The regional attenuation functional *D (r, r_{ref}, f)* obtained for the Maule region from the regression on the peak amplitudes of the band-pass-filtered ground velocities at the sampling frequencies (color curves). The attenuation function is normalized to zero at the reference hypocentral distance of 40 km. The black curves in the background are from an attenuation model.

k = 0.02 (sec)		$Q(f) = 100\, f^{0,65}$	
high frequencies		**low frequencies**	
Km	$g(r)$	Km	$g(r)$
1.0	-1.15	1.0	-1.15
80	-0.0	80	-0.0
180	-0.4	180	-0.2
		300	-0.5
M_w		**$\Delta\sigma$ (MPa)**	
4.0		30	
4.5		50	
5.0		90	
5.5		100	
6.0		100	

Table IV.1: In this model of crustal attenuation we use to predict shapes and level of the seismic spectra: ***g(r)***=body-wave geometrical spreading; ***Q(f)***=crustal attenuation parameter; ***Δσ***=stress drop; ***k***=residual systematic attenuation parameter.

Figure IV.5 compares the observed and predicted excitation of filtered velocity spectra obtained from the Chile region. The black lines indicate the regression result, and the red thick lines denote the theoretical excitations computed. Table IV.1 provide the parameters of our working model.

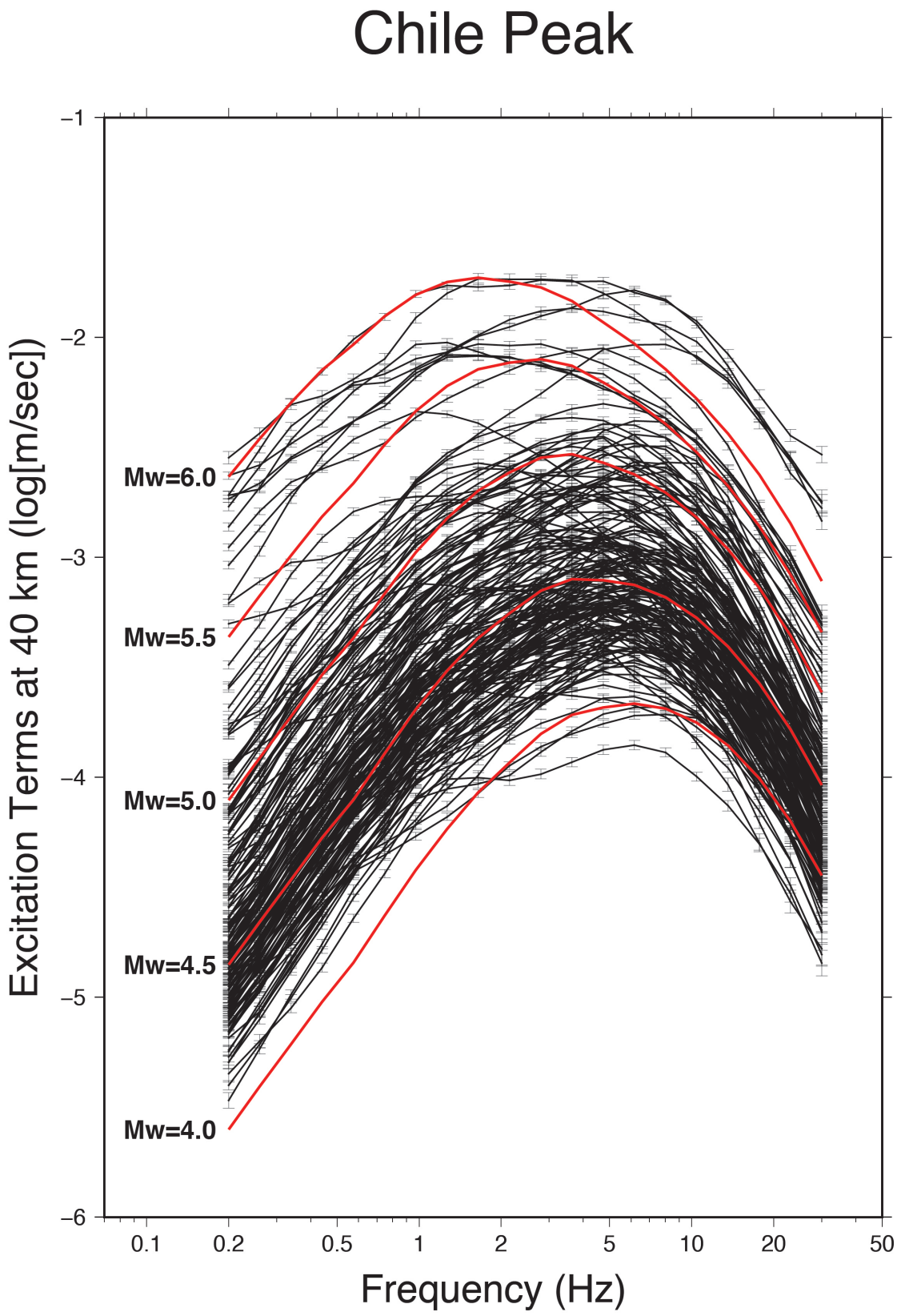

Figure IV.5: Filtered ground velocity excitation terms relative to the aftershocks recorded during the Maule seismic sequence in 2010 (black lines). Red thick lines indicate the theoretical prediction at the indicated levels of moment magnitude.

Figure IV.6 shows the site terms obtained from the regression on the peak amplitudes. Given the constraint

$$\sum_i SITE_i(f) = 0 \tag{IV.3}$$

$$D\ (r = r_{ref}, f_i) = 0 \tag{IV.4}$$

the individual site terms shown in the Figure IV.6 represents the deviation of the specific site from the network average. The constraints given by (IV.3) and (IV.4) are necessary in order to reduce the degrees of freedom of the system prior to the inversion. Moreover, by forcing the conditions (IV.3) and (IV.4) we give a precise physical meaning to the excitation terms, since they now represent what would be recorded at the reference hypocentral distance by the average network site.

To give an example, if we knew the absolute site term at a specific station at all frequencies, we could have forced the corresponding term in the inversion to be equal to the known site response. In such a case, the excitation terms would have represented the peak spectra of the events, as they would have been recorded at the specific site, with all events located at the reference hypocentral distance. Figure IV.6 shows that there are large fluctuations from the network average at the various frequencies.

No detailed information about the site geology is available at each seismometric location, although we know that all of them were deployed on rock outcrops. For this reason we expect the constraint forced on the site terms to result in a relatively small bias on the inverted source terms, and thus our model predicts the expected rock outcrop motion in the region.

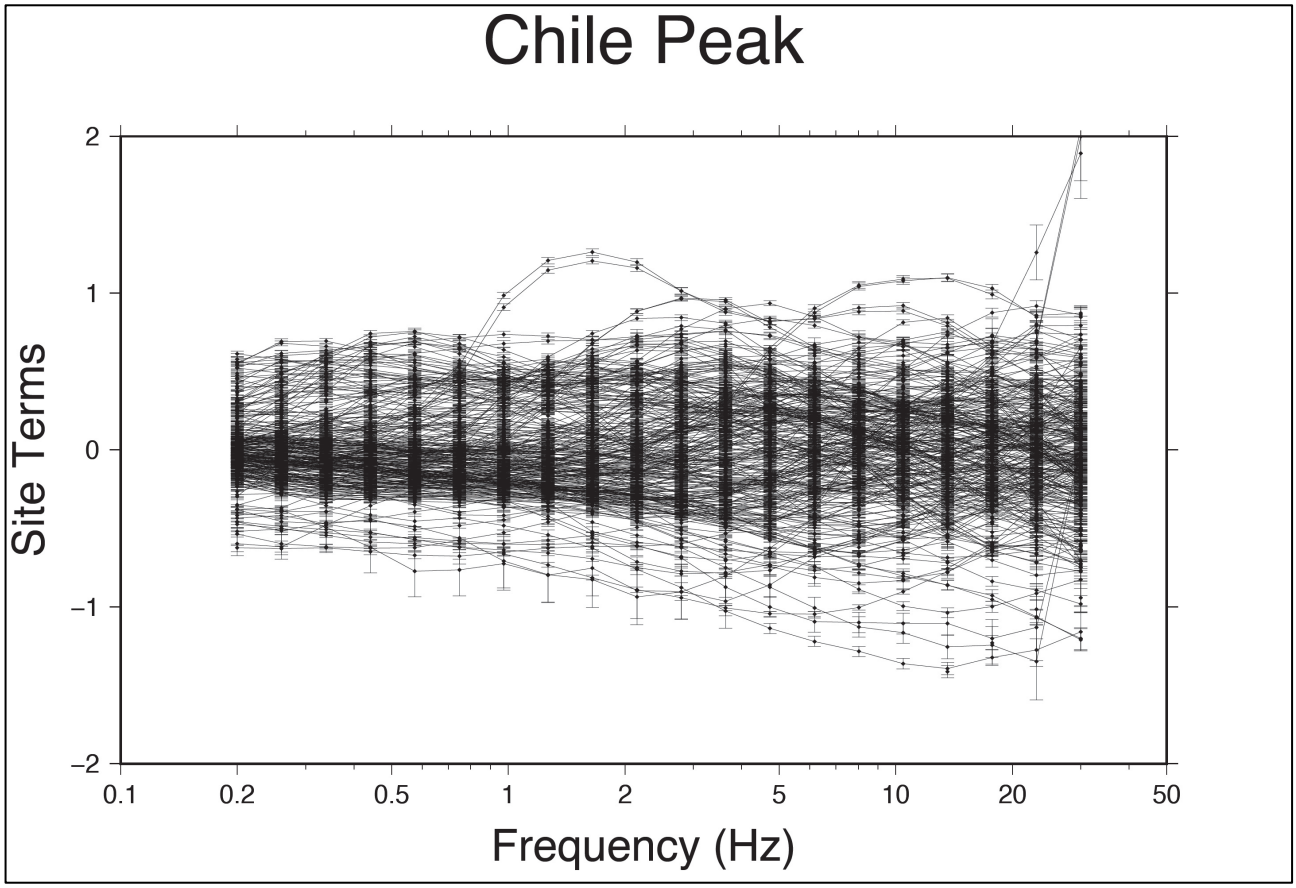

Figure IV.6: Inverted site terms for the Maule data set.

IV.3 Conclusions

The prediction of the earthquake ground motion has always been of primary interest for seismologists and structural engineers. For engineering purposes it is necessary to describe the ground motion according to certain number of ground motion parameters such as: amplitude, frequency content and duration of the motion. However, it is necessary to use more than one of these parameters to adequately characterize the ground motion excited by a specific source, and observed at a specific site.

In this study, we analyzed data set acquired by portable network installed to monitor the aftershocks of the Maule earthquake to validate the analysis procedure. This data set provided a unique opportunity to quantify high-frequency earthquake ground motion in a subduction zone due to the quality and quantity of observations in the frequency and distance ranges of 0.2-30 Hz and 40-500

km. The analysis was done using a two-step modeling procedure: i) a regression was performed to characterize source duration and excitation, source-receiver distance dependence, and station site effects; ii) a point-source forward model is constructed in terms of geometrical spreading, observed duration, site effects, and source scaling, in order to match the regression results. The outlined procedure provides the necessary point source parameters for a stochastic finite-fault modeling of the ground motions for future large earthquakes in this subduction zone.

A proper description of ground motion scaling requires presenting enough information to duplicate the observations. This means that, until definitive information will be available on source scaling and absolute site effects, $Q(f)$ cannot be presented without being coupled to $g(r)$ and κ.

An important future goal of this research is represented by the study on source scaling. We will perform this task by using a technique based on the analysis of source spectral ratios. Numerous studies were published by Malagnini, Mayeda, and co-workers on all tectonic environments (normal, strike-slip, and reverse), but no data have yet been analyzed on subduction earthquakes; for this reason, the present data set will be of special interest.

Abstract

Inadequate seismic design codes can be dangerous, particularly when they underestimate the true hazard. In this study we use data from a sequence of moderate-sized earthquakes in northeast Italy to validate and test a regional wave propagation model which, in turn, is used to understand some weaknesses of the current design spectra. Our velocity model, while regionalized and somewhat ad hoc, is consistent with geophysical observations and the local geology. In the 0.02–0.1 Hz band, this model is validated by using it to calculate moment tensor solutions of 20 earthquakes ($5.6 \geq M_w \geq 3.2$) in the 2012 Ferrara, Italy, seismic sequence. The seismic spectra observed for the relatively small main shock significantly exceeded the design spectra to be used in the area for critical structures. Observations and synthetics reveal that the ground motions are dominated by long-duration surface waves, which, apparently, the design codes do not adequately anticipate. In light of our results, the present seismic hazard assessment in the entire Pianura Padana, including the city of Milan, needs to be re-evaluated.

V.1 Introduction

On May 20 2012, an event of M_L 5.9 (M_W 5.6) struck the southern edge of the Po river flood plain (Pianura Padana), approximately 30 km West of the town of Ferrara, and 10 km to the NW of the village of Finale Emilia (INGV). On 05/19/2012 at 23:13:27 the earthquake was preceded by a foreshock of M_L 4.1 (M_W 3.8). Hypocentral depths were 6.3 km for both events; centroid depths were 5 and 6 km (main and foreshock, respectively). Fault was a reverse one, dipping 45° to the South (Figure V.1). The main shock started a complex seismic sequence, in which six more earthquakes with $M_L \geq 5$ struck the area, the latest one on June 3 2012. Aftershocks delineated a 50 km-long strip, 10–15 km wide, elongated in the EW direction (Figure V.1). A total of 2100 events were located between May 19 and June 25 2012 by the INGV National Seismic Network. 80 of them (whose waveforms were gathered and used for this study) had $M_L \geq 3.5$.

The widespread damage due to the seven M_L 5+ earthquakes was especially severe for historical towns and industrial infrastructures. However, a striking inconsistency exists between the relatively small main events of the sequence ($M_W \leq 5.6$), and the corresponding high level of shaking (a PGA of 9 m/sec^2 was recorded by the MRN strong-motion station on the vertical component of the

ground motion, whereas a value of 3 m/sec^2 was observed on the horizontal motions), that, together with observed extreme durations, caused severe damage to houses and industrial structures, as well as the occurrence of widespread liquefaction phenomena [*EMERGEO Working Group*, 2012, http://emergeo.ingv.it]. In this study we used the seismic profile App_Orient_1 (see http://unmig.sviluppoeconomico.gov.it/videpi/) to define a velocity structure of the shallow crust beneath the Pianura Padana. The crustal model was validated using the broadband waveforms of our data set. Like for the L'Aquila case study presented by Herrmann et al. [2011], our goal was the inversion of waveforms in the frequency band between 0.02 and 0.1 Hz. Synthetic seismograms highlighted important implications for the seismic hazard in the Pianura Padana, because the shallow structure of the Po flood plain dramatically affects also the high-frequency ground motion, with which damage should strongly correlate.

V.2 Regional Velocity Structure and Moment Tensor Solutions

The study area (Figure V.1a) includes the Ferrara arc: one of the northernmost portions of the Northern Apennines thrust front, that was active during late Pliocene - early Pleistocene times [Scrocca et al., 2007]. The Ferrara arc lies under a thick sedimentary cover from the Po river with an average sediment thickness of 2–4 km. Thicknesses up to 8.5 km characterize the deepest depocenters of the valley [Pieri and Groppi, 1975].

We compared geological data in literature [Carminati et al., 2010; Fantoni and Franciosi, 2010] (see Figures V.1b and V.1c) against the seismic profile App_Orient_1, and con- structed a 1D velocity model of the shallow crust for the area. We started from the deeper part of the model CIA [Herrmann et al., 2011], and added shallow low-velocity layers based on the gathered information. We thus obtained a crustal model called PADANIA (Table V.1) that, on a N-S path across the basin to stations SALO and MAGA, fitted well the dispersion curves of Love waves at periods as low as 10 sec (Figure V.2).

Rayleigh wave dispersion data are also acceptably fitted by model PADANIA, down to 10 sec or less (Figure V.2). However, small time shifts allowed to the synthetic seismograms of actual earthquakes permit very satisfactory fits, partially correcting distance- and azimuth- dependent model imperfections (see figures in the Supplemental Material Chapter V). The locations of stations SALO and MAGA can be found in Figure 1d. Models CIA and PADANIA overlap below 4 km from the free surface.

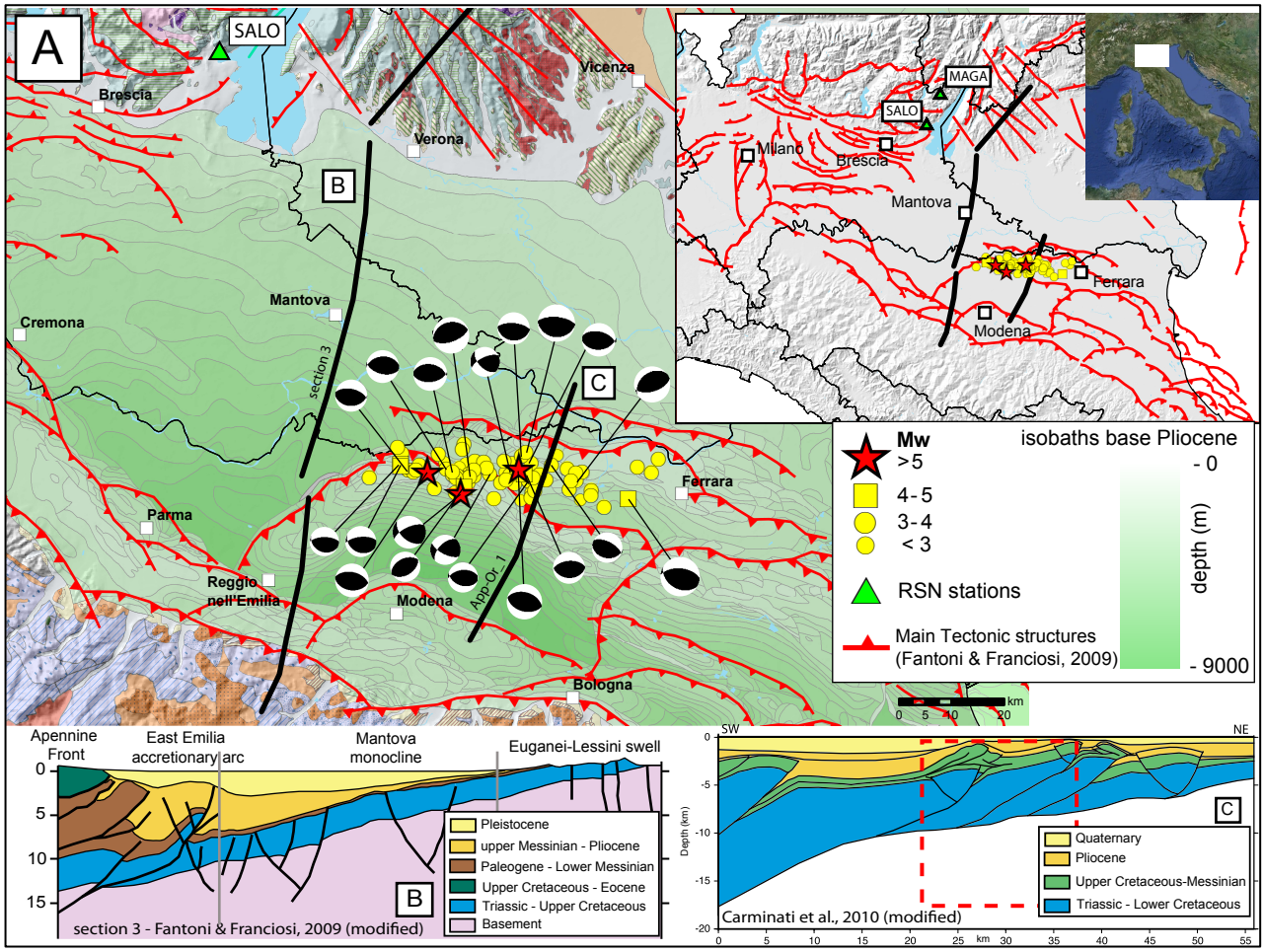

Figure V.1: (a) Structural setting of the study area, as as reported by Consiglio Nazionale delle Ricerche [1992]. Isobaths contours of Pliocene base surface below the whole Po Plain highlight the buried architecture of the area. Main tectonic linea- ments are taken from Fantoni and Franciosi [2010]. 78 events of the entire seismic sequence and our 22 MT solutions are plotted. (b) Geological cross section modified from Fantoni and Franciosi (2010, three-pieces profile B of Figure V.1a): gray vertical lines mark the discontinuities of the profile. (c) Geological cross section built on the interpretation of the App_Or_1 seismic profile (modified from Carminati et al. [2010], profile C in Figure V.1a); dashed box indicates a section of the volume that is potentially interested by the seismic activity. (d) Location of the various elements, including the seismic stations SALO and MAGA, which were used to investigate the PADANIA model.

Thickness (km)	V_P (km/sec)	V_S (km/s)	(kg/m^3)	Q_P	Q_S
1.0	1.9000	0.8000	2.25E+03	50	25
1.0	2.6000	1.4300	2.60E+03	80	56
2.0	3.8000	2.1350	2.65E+03	200	200
0.5	4.4000	2.4400	2.85E+03	250	250
0.5	4.9399	2.8210	2.85E+03	250	250
3.0	6.0129	3.4336	2.85E+03	250	250
7.0	5.5516	3.1475	2.85E+03	600	300
15.0	5.8805	3.3583	2.85E+03	600	300
6.0	7.1059	4.0081	3.00E+03	600	300
8.0	7.1000	3.9864	3.01E+03	600	300
0.0	7.9000	4.4036	3.28E+03	600	300

Table V.1: The PADANIA Model

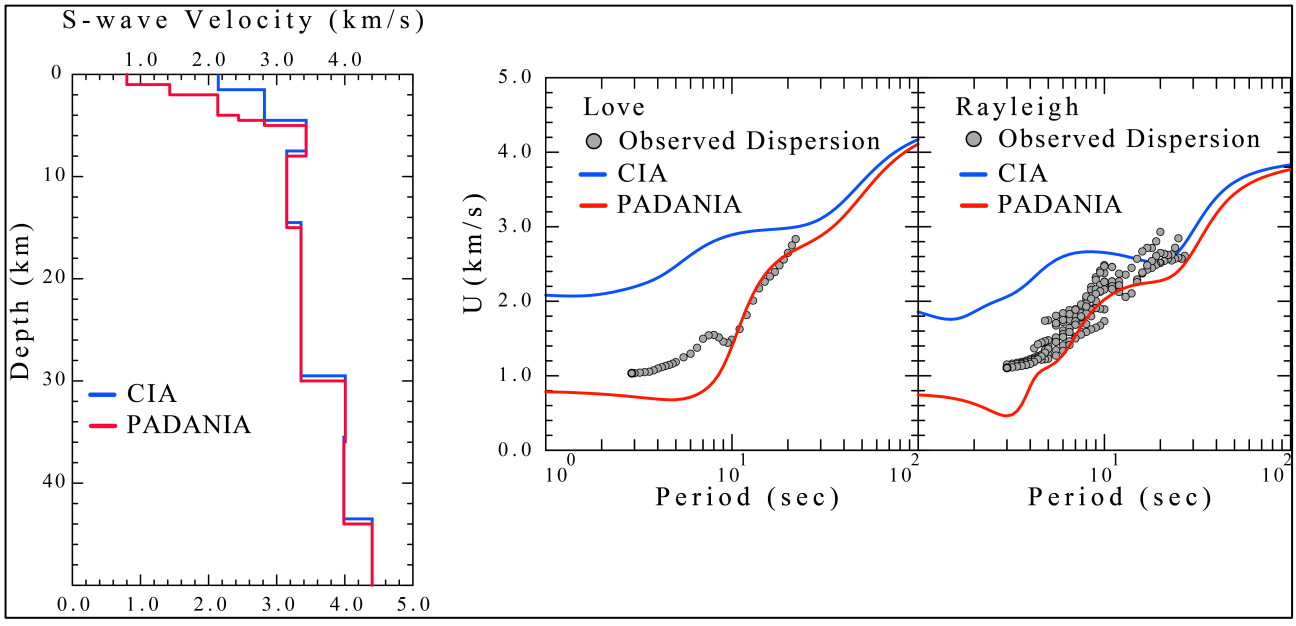

Figure V.2: Love and Rayleigh dispersion observations obtained at stations MAGA and SALO (circles), compared to theoretical predictions from the crustal models CIA (gray curves) and PADANIA (black curves). Most of the source-receiver paths are within the sediments. The events used for the dispersion analysis are the ones indicated with footnote a in Table V.2, as well as the seismograms from two events occurred on 06/01/2012 at 12:22:44, and on 06/01/2012 at 23:07:15.

With the PADANIA crustal model, we attempted to compute stable moment tensor solutions for the 80 earth- quakes with $M_L \geq 3.5$.

Due to the high level of ambient noise that affect most stations within and around the Po valley, we were able to compute only 20 robust focal solutions (Figure V.1a and Table V.2).

Focal mechanisms outline the existence of a thrust fault system that is in good agreement with the reconstructions by Fantoni and Franciosi [2010], and Carminati et al. [2010].

We found that only three earthquake of the sequence had $M_W > 5$, and noted a systematic discrepancy between M_W and M_L for the events analyzed (Table V.2).

A regression yielded the following relationship, for the INGV network M_L, and the corresponding M_W (Figure V.3):

$$M_L = M_W + 029 \; ; \quad 3.5 \leq M_L \leq 5.9 \tag{V.1}$$

We will analyze the reasons for the discrepancy described in (V.1) by comparing time histories calculated using models PADANIA and CIA. For earthquakes in the Appennines, we usually observe that $M_L = M_W$ [Herrmann et al., 2011].

The difference indicated in equation (V.1) may be a direct consequence of the fact that the Ferrara earthquakes occurred underneath a very thick layer of low-velocity sediments.

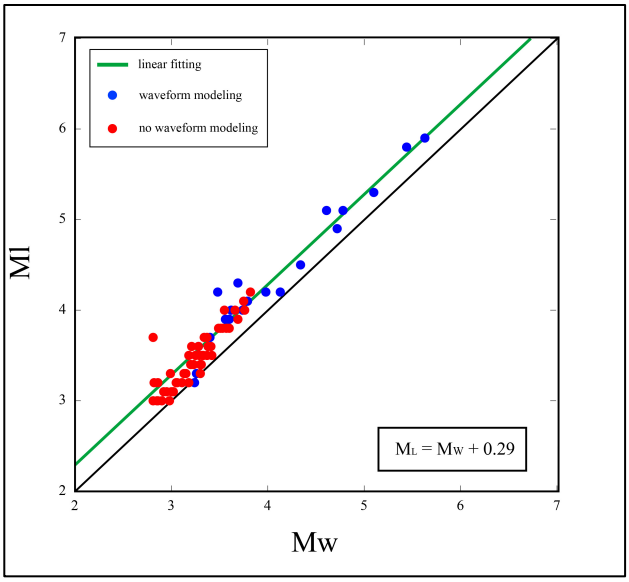

Figure V.3: This plot shows a regression for the INGV network M_L, and the corresponding M_W.

from INGV Network location					from MT Solution							
Date	Time	Latitude	Longitude	M_L	Depth	M_W	Strike		Dip		Rake	
							p1	p2	p1	p2	p1	p2
05/19/2012	23:13:27	44.898	11.258	4.10	5.0	3.79	284	85	52	40	102	75
05/20/2012	02:03:53	44.889	11.228	5.90	6.0	5.63	285	105	45	45	90	90
05/20/2012	03:02:50	44.860	11.095	4.90	13.0	4.72	245	132	65	50	45	147
05/20/2012[a,b]	09:13:21	44.879	11.241	4.20	7.0	4.13	265	94	55	35	85	97
05/20/2012	12:50:24	44.866	11.366	3.90	6.0	3.60	235	73	35	56	75	100
05/20/2012	13:18:02	44.831	11.490	5.10	7.0	4.78	275	120	55	38	75	110
05/21/2012	08:01:36	44.911	11.235	3.20	7.0	3.24	275	95	65	25	90	90
05/21/2012	18:02:26	44.847	11.259	3.60	11.0	3.28	245	135	65	54	40	149
05/22/2012	06:11:15	44.850	11.074	3.70	5.0	3.40	245	58	45	45	95	85
05/23/2012	21:41:18	44.868	11.251	4.30	7.0	3.69	265	108	50	42	75	107
05/24/2012	14:34:38	44.868	11.293	3.30	7.0	3.26	297	100	61	30	99	75
05/25/2012	13:14:05	44.883	11.108	4.00	5.0	3.62	260	70	30	60	99	85
05/27/2012	18:18:45	44.882	11.158	4.00	6.0	3.74	201	310	60	60	145	35
05/29/2012	07:00:03	44.851	11.086	5.80	5.0	5.44	270	97	45	45	85	95
05/29/2012	08:25:51	44.901	10.943	4.50	7.0	4.34	270	113	65	27	80	110
05/29/2012	08:40:58	44.892	10.962	4.20	7.0	3.98	282	90	56	35	97	80
05/29/2012[a,b]	09:30:21	44.892	11.053	4.20	5.0	3.48	104	265	52	40	102	75
05/29/2012[a,b]	10:55:57	44.888	11.008	5.30	6.0	5.10	280	100	50	40	90	90
05/29/2012[a,b]	14:39:40	44.882	11.068	3.90	5.0	3.56	280	85	41	50	102	80
06/03/2012	19:20:43	44.899	10.943	5.10	10.0	4.61	265	117	65	29	75	119

Other Events

Date	Time	Latitide	Longitude	M_L	Depth
05/29/2012[a,b]	11:07:05	44.876	11.076	15.0	4.00
05/30/2012[a]	06:00:33	44.931	10.937	5.0	3.80
05/31/2012[a]	04:21:56	44.872	11.262	4.5	3.60
06/01/2012	12:22:44	44.877	10.986	6.7	3.1
06/01/2012	23:07:15	44.948	10.914	2.3	3.5

Table V.2: The 20 Events for which we could obtain an MT Solution and other events used for the dispersion analysis.

[a]Events used in Figure V.2.

[b]Events used in Figure V.3b.

p1= plane 1.

p2= plane 2.

V.3 Synthetic Seismograms

In order to compare synthetic seismograms generated using models CIA and PADANIA (up to a 5 Hz maximum frequency), we simulated an M_W 4 earthquake with the following source parameters: Strike = 105, Dip = 40, Rake = 100, Depth = 5 km, representative of the typical event of the sequence (depths of the events are well constrained, see the Supplemental Material Chapter V). We are aware of the fact that we cannot use model PADANIA for successfully reproduce the individual wiggles of the recorded seismograms in the frequency band between 0.1 Hz and 1 Hz, but we strongly believe that the new crustal model may be used to understand the general properties of the ground motion in Pianura Padana.

Seismograms of Figure V.4a (Transverse and Vertical components of the ground motion) are calculated at an epicentral distance of 40 km, and an azimuth of 330 (i.e., along the path to station SALO). Upper waveforms (in red) in each frame of Figure V.4a refer to model PADANIA, whereas lower seismograms (in black) refer to model CIA. Figure V.4a shows that surface waves dominate the seismograms in the PADANIA crustal structure.

Large amplitudes and durations of the ground motion are documented in Figure V.4b, where the seismograms observed at SALO during five earthquakes (black shading) are compared with synthetic time histories calculated with the source parameters and azimuth used for Figure V.4a. Observed and synthetic waveforms are normalized to their peak values after they are bandpass-filtered in the indicated frequency bands.

We satisfactorily reproduce the low-frequency char- acters of the observed seismograms of Figure V.4b, together with the extreme duration of the ground motion at all fre- quencies. The extreme durations that characterize the ground motion at high frequencies, at least between 0.02 Hz and 1.0 Hz (bottom frames in Figure V.4b), are due to the strong dispersion characteristics of the seismic waves trapped in the thick sedimentary layer at the surface, and may also be influenced by the attenuation characteristics of the crust in the region [Del Pezzo et al., 2011].

Finally, anomalous durations of the ground motion may be one of the main reasons for the anomalous level of damage observed in the epicentral area, and for the widespread occurrence of liquefaction phenomena as well (Emergeo Working Group, 2012).

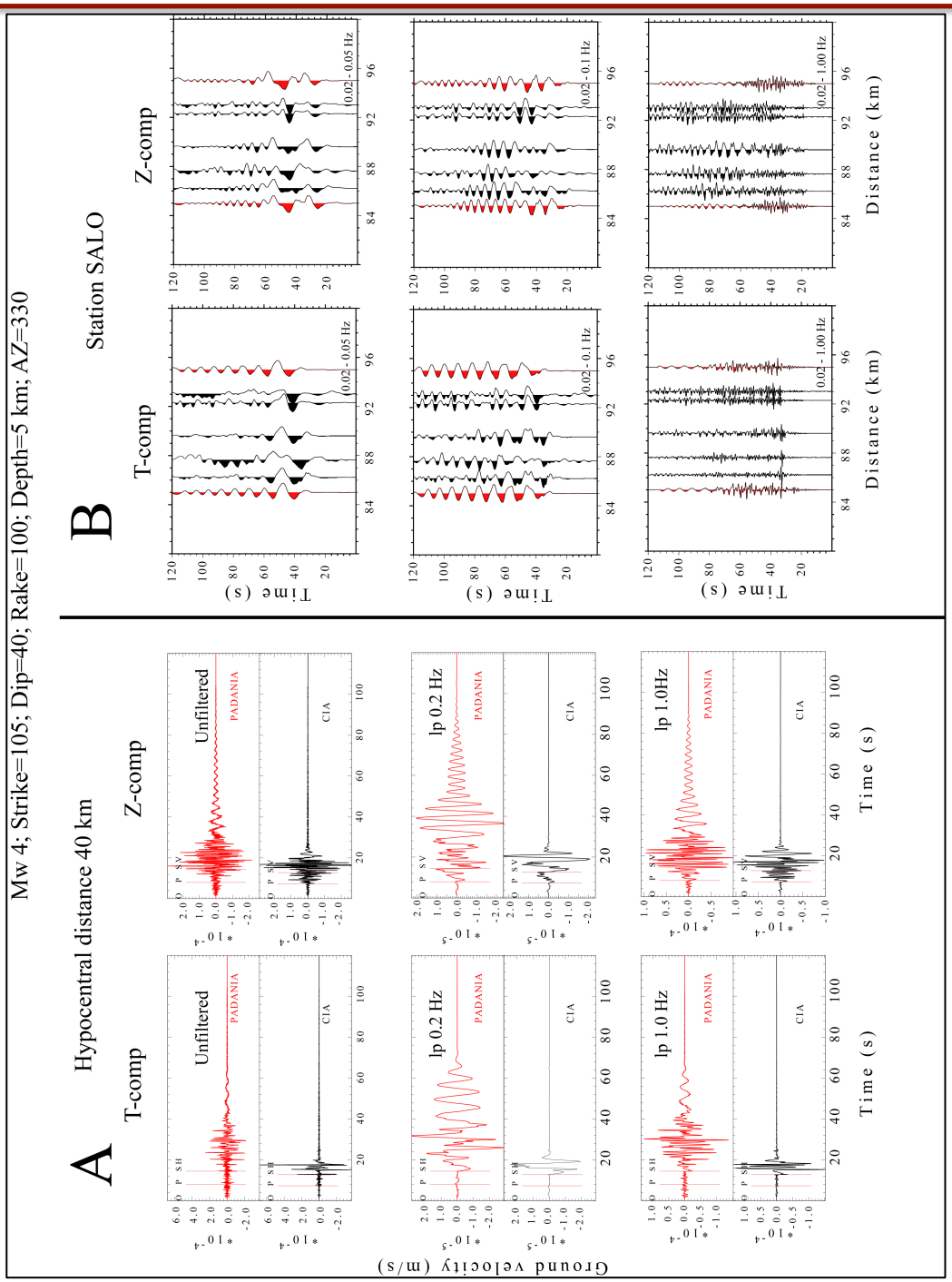

Figure V.4: (a) Synthetic seismograms (left: transverse components; right: vertical components) calculated at 40 km distance and at an azimuth of 300° over the PADANIA and CIA crustal models (red and black, respectively), for an earthquake of M_W 4, strike = 105°; dip = 40°; rake = 100°. From top to bottom: i) unfiltered; ii) bandpass filtered between 0.02 and 0.2 Hz; iii) bandpass filtered between 0.02 and 1.0 Hz. (b) Waveforms recorded at SALO (T and Z components of the ground motion, black shading) during five earthquakes (events marked with footnote b in Table V.2), compared with synthetic waveforms (red shading) calculated around the same hypocentral distances. Parameters are the same as before. Amplitudes are normalized to their peak values. Waveforms are bandpass-filtered in the following frequency bands: top 0.02–0.05 Hz; middle 0.02–0.1 Hz; bottom 0.02–1.0 Hz.

V.4 Seismic Hazard

Figure V.5 shows the spectral acceleration of the closest waveform registered at a Joyner-Boore distance R_{jb} = 5 km at the Mirandola (MRN) strong-motion station (used in engineering seismology to take into account the finite dimensions of a seismic source, R_{jb} indicates the distance to the nearest point of the vertical projection to the surface of a fault rupture). MRN is classified as a C-type soil in the EC8 classification [*European Committee for Standardization*, 2003].

During the main event of May 20 2012 (M_W 5.63, see Table V.2) site MRN recorded a horizontal Peak Ground Acceleration (PGA) of 3 m/sec^2 [Dolce et al., 2012].

We compared the observed spectral acceleration of the radial and transverse component at MRN (5% damping) with the Italian building code spectra (Uniform Hazard Spectra - UHS) relative to soil class C, and two different return periods: 475 and 2475 years (Figure V.5).

UHS estimates are obtained from the official website of the Consiglio Superiore dei Lavori Pubblici (http://www.cslp.it/cslp/), and are based on the recently developed National Probabilistic Seismic Hazard Maps for Italy (http://esse1.mi.ingv.it/).

We argue that, if compared with the maximum magnitude expected for the area ($M_W$max = 6.14 [see Stucchi et al., 2011]), the main earthquake of the Ferrara sequence is characterized by a small moment magnitude (M_W = 5.63).

Yet, Figure V.5 shows that the spectral acceleration observed during the main event at station MRN largely exceeds the design spectra (the UHS) in a broad frequency range around 1 Hz. In fact, at 1 Hz, the observed transverse component of the ground motion is a factor of two larger than the estimate for the 475 years return period, and almost 30% larger than that relative to a return period of 2475 years.

The considerations just made clearly demonstrate the need for an update of the reference hazard map of northern Italy, in which the regional characteristics of the ground motion are to be included.

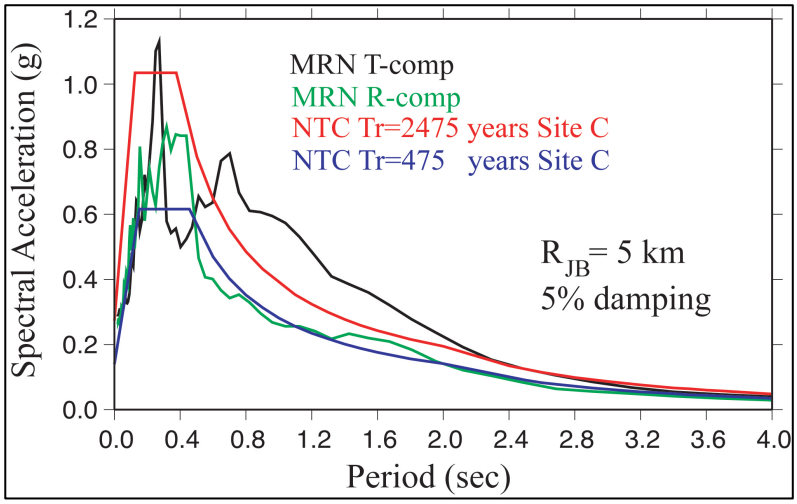

Figure V.5: Transverse and radial Spectral Acceleration (black and green, respectively) recorded at station MRN (Mirandola, EC8 site C) during the main event of 05/20/ 2012 (MW 5.63, 5 km Joyner-Boore distance). SAs are plotted against 475 and 2475 years return time estimates (blue and red, respectively) for an EC8 C site.

V.5 Conclusions

We calibrated a 1-D crustal structure (model PADANIA) for seismic paths going across the Pianura Padana, allowing the inversion of moment tensor solutions for 20 events of the Ferrara seismic sequence, from M_W 5.63 (the largest main event, occurred on May 20 2012), down to M_W 3.2.

Due to a high noise level at low frequency, we were not able to obtain acceptable moment tensor solutions for all the 80 events of the sequence with $M_L \geq 3.5$. Nevertheless, PADANIA represents a major improvement for the investigation of the seismicity along the southern edge of the Pianura Padana. We also used model PADANIA in order to perform a numerical study on the characteristics of the ground motion in the thick sediments of the flood plain, in the frequency band between 0.02 and 1.0 Hz. Our synthetic seismograms correctly reproduced the anomalous durations of the ground motion observed on the sediments at high frequencies, at least up to 1 Hz, and Figure V.4 shows how the seismograms in the Po flood plain are dominated by surface waves, that may have played a major role in enhancing the damage observed on industrial structures.

Predicted Spectral Accelerations (SA) at 5% damping for a return period of 2475 years (see Figure V.5) were exceeded at station MRN by the spectral acceleration observed during the largest main

event of May 20 2012. Note that predicted SAs are somehow controlled by the maximum magnitude chosen for the area (M_{Wmax} = 6.14 [see Stucchi et al., 2011]), which is 0.5 magnitude units larger than that of the main event that struck Ferrara.

The inconsistency pointed out in Figure V.5, between observed SA and UHS, indicates the necessity of including the regional characteristics of the ground motion into the tools used for the calculation of the UHS, at least in this region of Italy. Although the work on regional Ground Motion Predictive Equations (GMPEs) in Italy was included in the logic tree of the hazard map [Montaldo et al., 2005], no high-quality digital waveforms from substantial earthquakes in the Pianura Padana were available until now, and no regional GMPE from this specific area could be included in the logic tree.

Because the fundamental characteristics of earthquake-induced ground motion are not taken into account in current estimates of seismic hazard, it is likely that, within the thick sedimentary body of the Pianura Padana, seismic hazard got substantially underestimated until now. The issue may be especially important at low-frequencies, with a substantial impact on the expected response of very tall structures, even in Milan.

The Supplemental Material is made of 20 figures describing the moment tensor solutions for the events of the Ferrara sequence that we were able to compute. All figures contain:

1) the map of the station distribution, with the epicentral location of the specific event;
2) the beach ball of the focal mechanism, with the indication of all the geometric parameters, the origin time, the epicentral coordinates, and the parameters used to bandpass filter the waveforms;
3) the plot of fit vs. centroid depth (green dots), with the corresponding focal mechanisms;
4) all the recorded waveforms that went through the inversion procedure (red), each one with the corresponding synthetic seismogram from the best-fit moment tensor (blue);
5) the plot of the offset used to improve the fit of each observed waveform, translated in km using the indicated group velocities, Red symbols refer to Rayleigh waves (Vertical –squares- and Radial –circles. Components of the ground motion) , and black triangles refe to Love waves (Transverse ground motion). In this plot, an event mislocation would result in a systematic pattern of offset vs. azimuth.

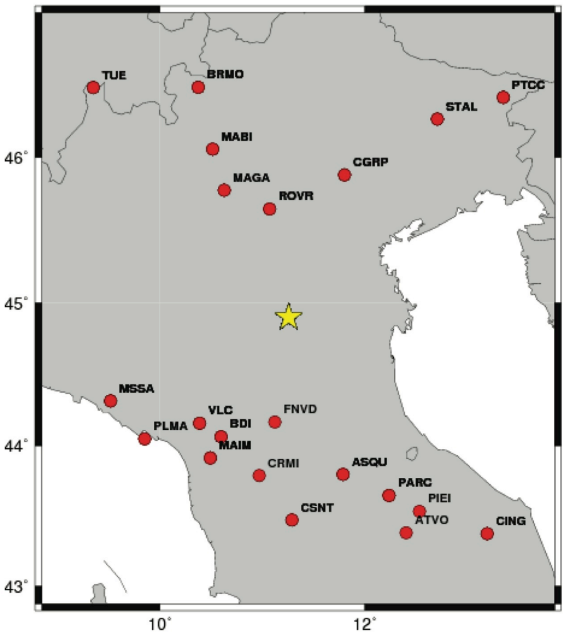

b) Location of broadband stations used for the waveform inversion.

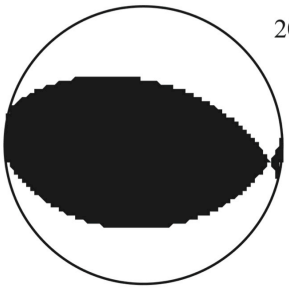

2012/05/19 23:13:27
44.898 11.258
Ml 4.10
Mw 3.79
Depth 5 Km
Strike 284
Dip 52
Rake 102
hp c 0.02 n 3
lp c 0.04 n 3

a) Waveform inversion focal mechanism.

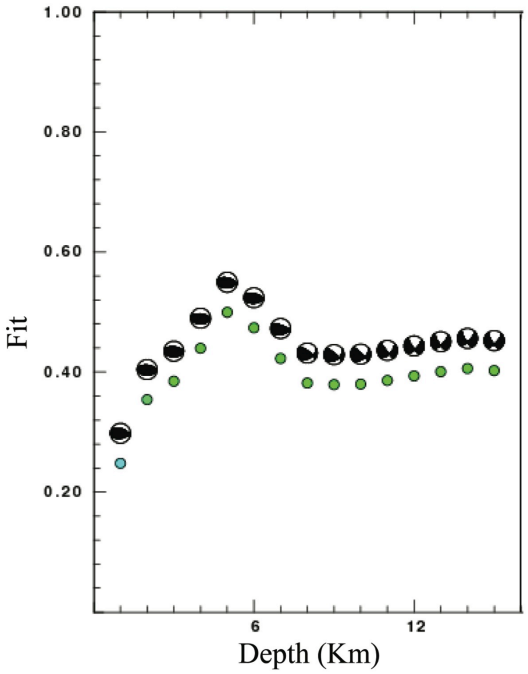

c) Depth sensivity for waveform mechanism

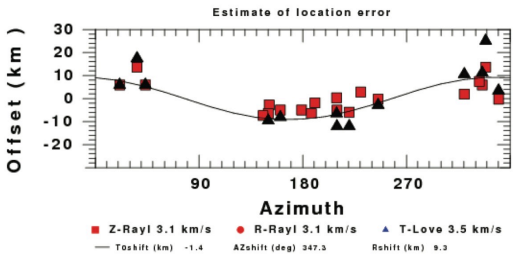

d) The time shifts for this inversion.

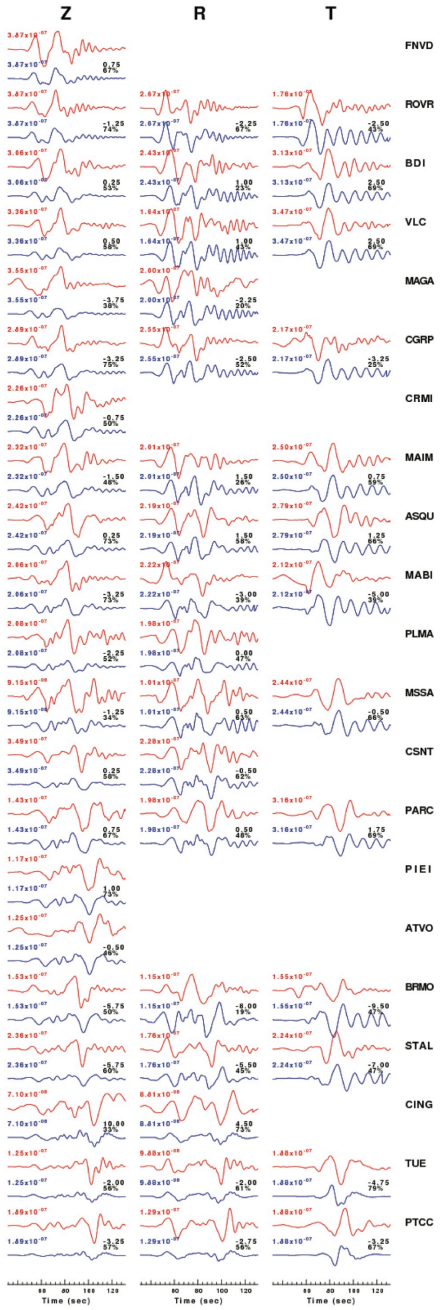

e) Comparison of the observed and predicted waveforms.

The foreshock occurred on 2012/05/19 at 23:13:27.

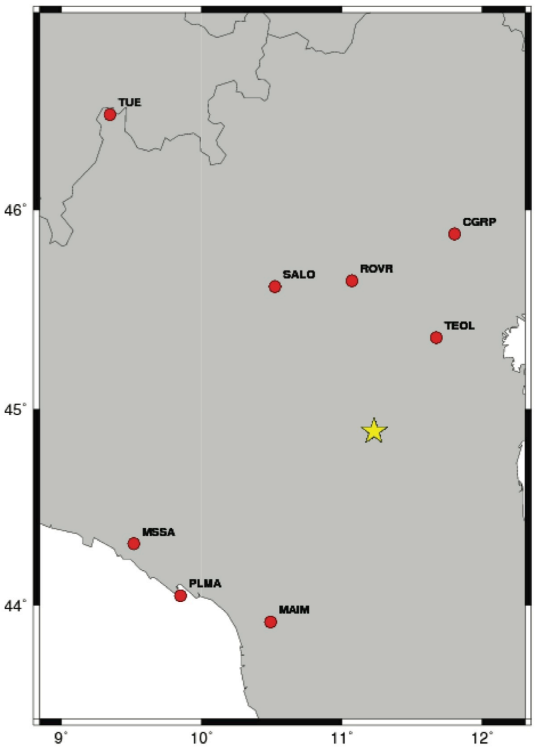

b) Location of broadband stations used for the waveform inversion.

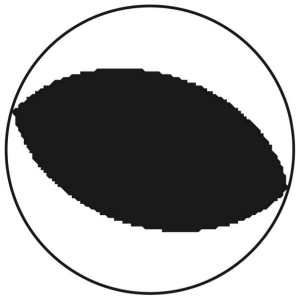

2012/05/20 02:03:53
44.890 11.230
Ml 5.90
Mw 5.63
Depth 5 Km
Strike 285
Dip 45
Rake 90
hp c 0.01 n 3
lp c 0.04 n 3

a) Waveform inversion focal mechanism.

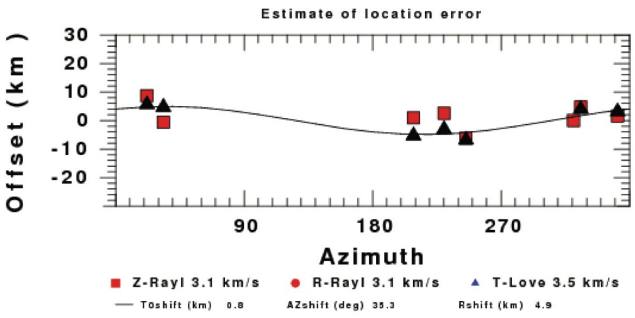

c) The time shifts for this inversion.

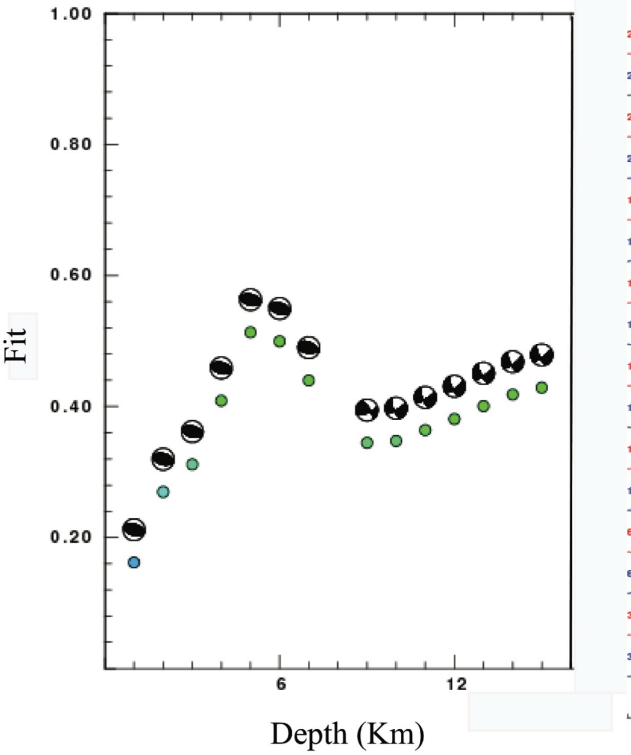

d) Depth sensivity for waveform mechanism

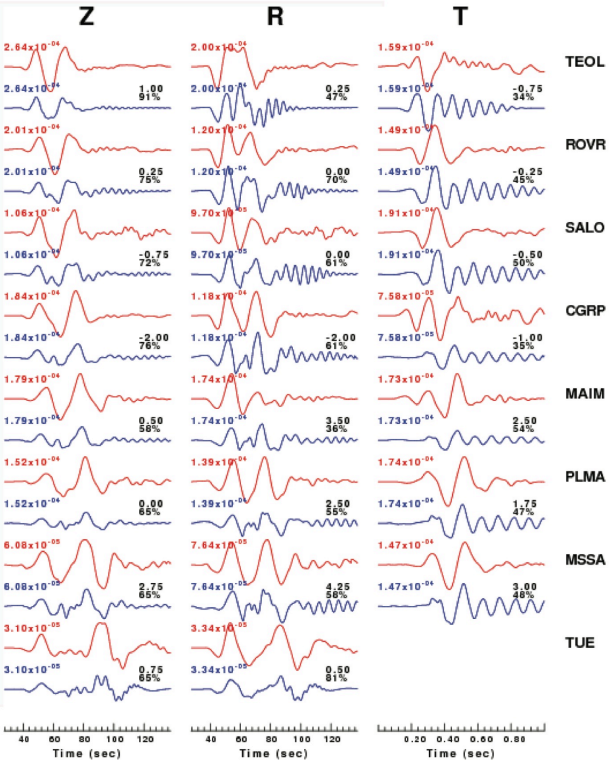

e) Comparison of the observed and predicted waveforms.

The main shock occurred on 2012/05/20 at 02:03:53.

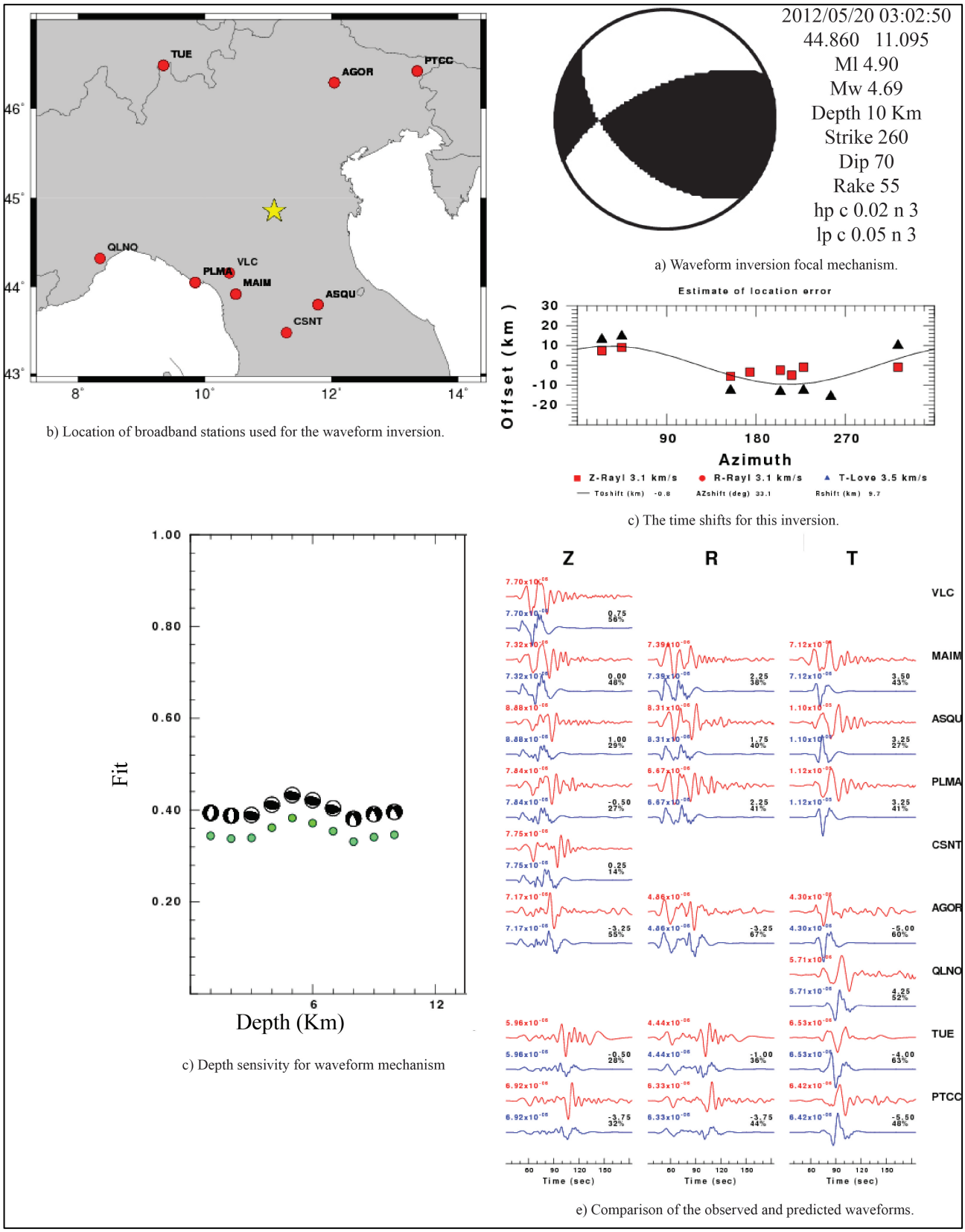

a) Waveform inversion focal mechanism.

b) Location of broadband stations used for the waveform inversion.

c) The time shifts for this inversion.

c) Depth sensivity for waveform mechanism

e) Comparison of the observed and predicted waveforms.

The event occurred on 2012/05/20 at 03:02:50.

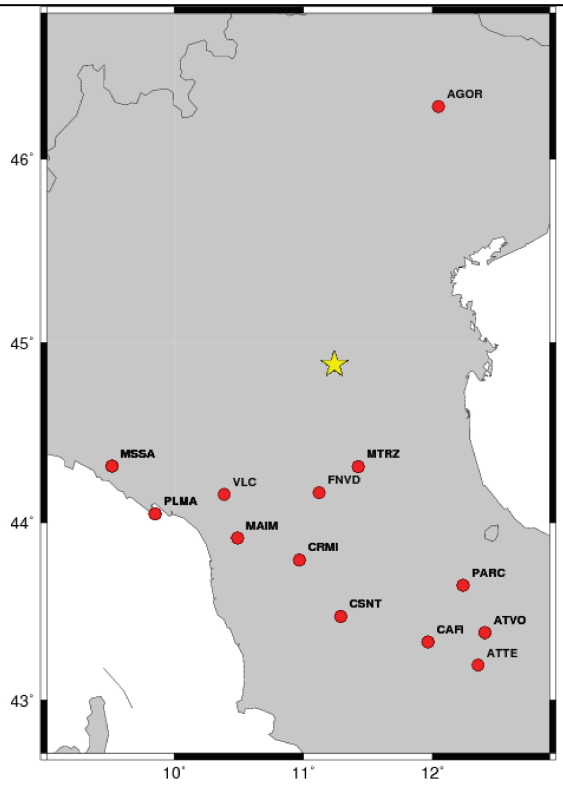

b) Location of broadband stations used for the waveform inversion.

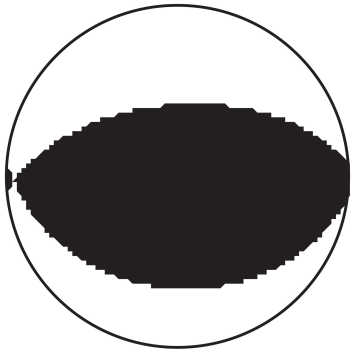

2012/05/20 09:13:21
44.879 11.241
Ml 4.20
Mw 4.13
Depth 7 Km
Strike 265
Dip 55
Rake 85
hp c 0.02 n 3
lp c 0.04 n 3

a) Waveform inversion focal mechanism.

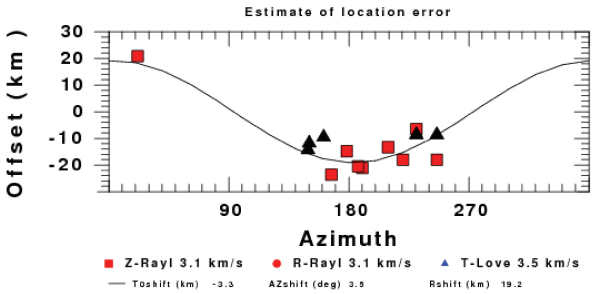

c) The time shifts for this inversion.

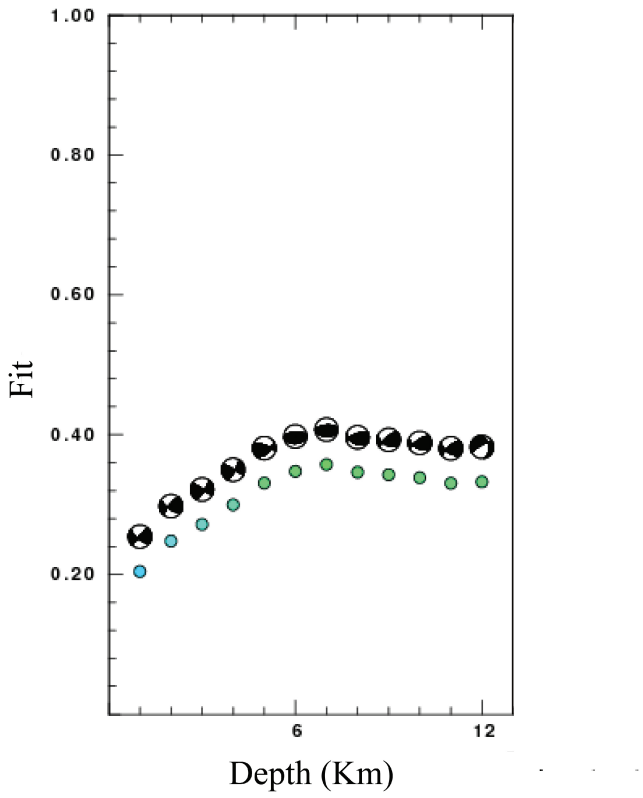

d) Depth sensivity for waveform mechanism

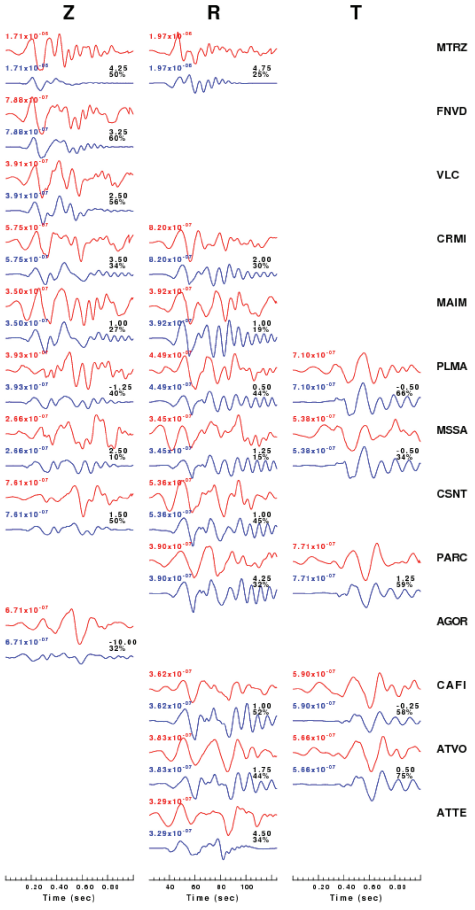

e) Comparison of the observed and predicted waveforms.

The event occurred on 2012/05/20 at 09:13:21.

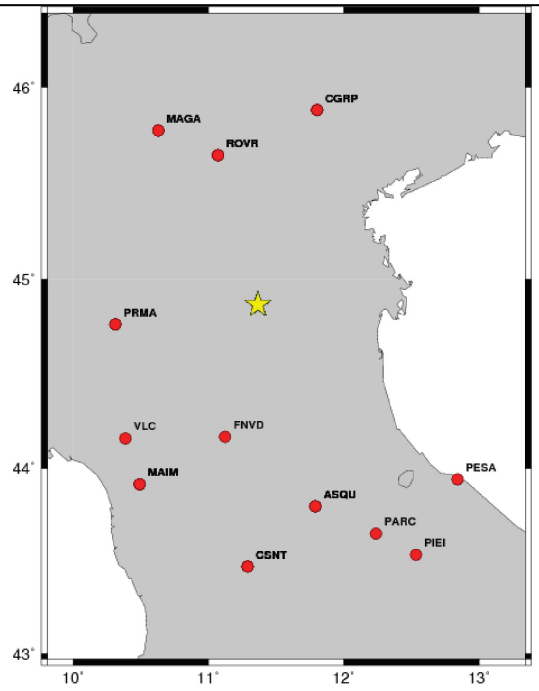

b) Location of broadband stations used for the waveform inversion.

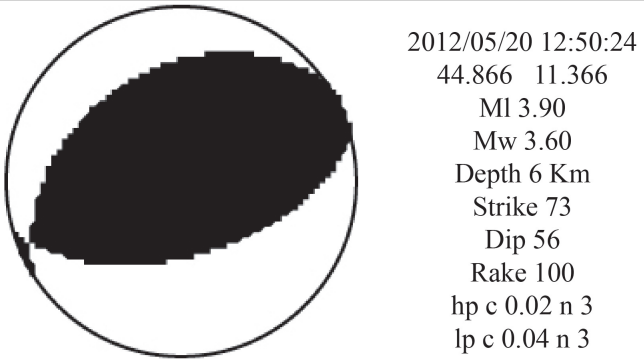

a) Waveform inversion focal mechanism.

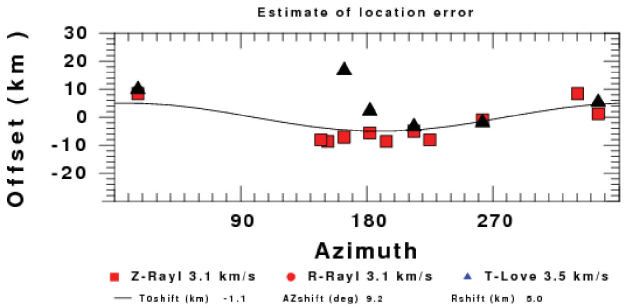

c) The time shifts for this inversion.

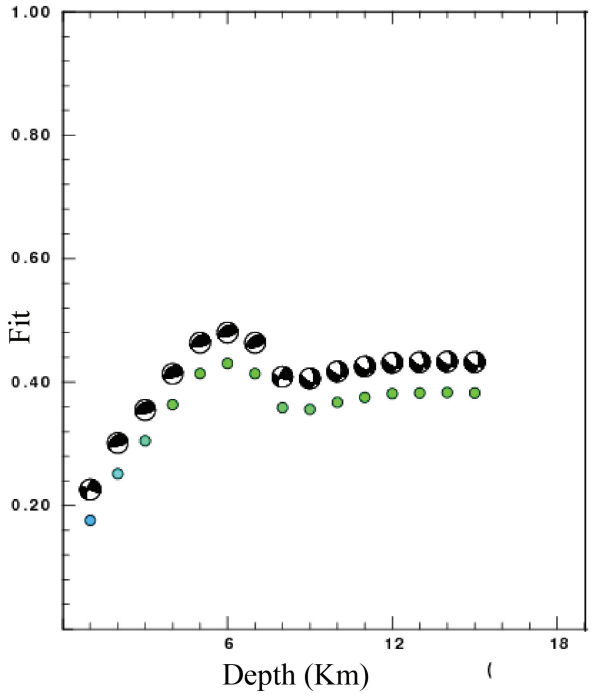

c) Depth sensivity for waveform mechanism

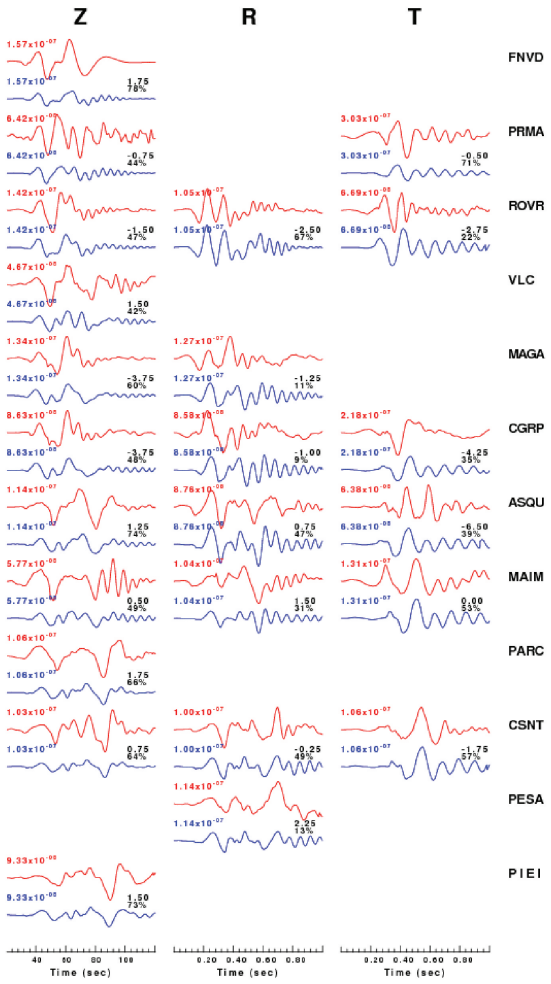

e) Comparison of the observed and predicted waveforms.

The event occurred on 2012/05/20 at 12:50:24.

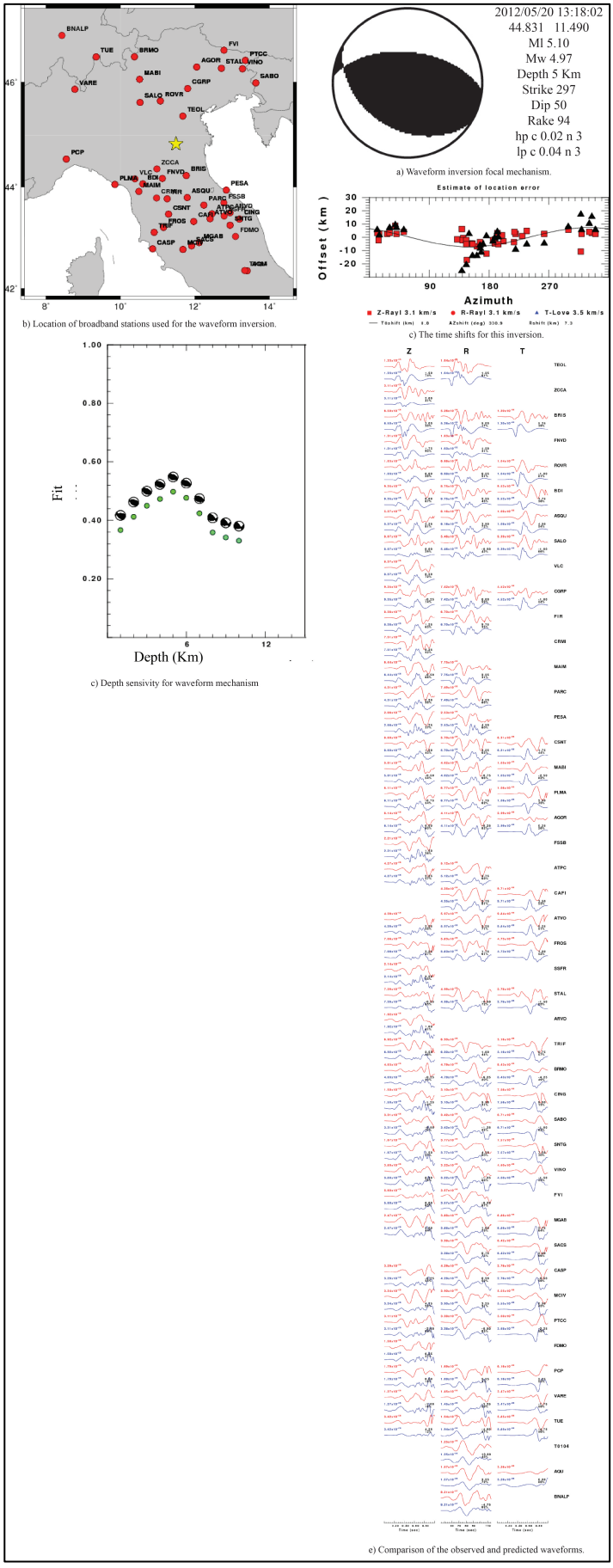

The event occurred on 2012/05/20 at 13:18:02.

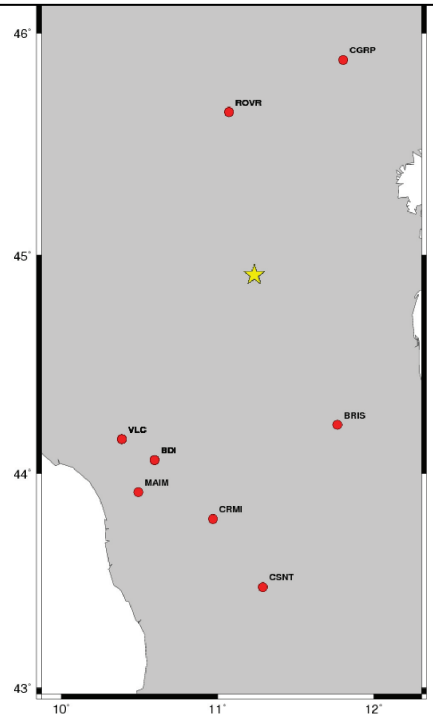

b) Location of broadband stations used for the waveform inversion.

2012/05/21 08:01:36
44.911 11.235
Ml 3.20
Mw 3.24
Depth 11 Km
Strike 275
Dip 65
Rake 90
hp c 0.02 n 3
lp c 0.04 n 3

a) Waveform inversion focal mechanism.

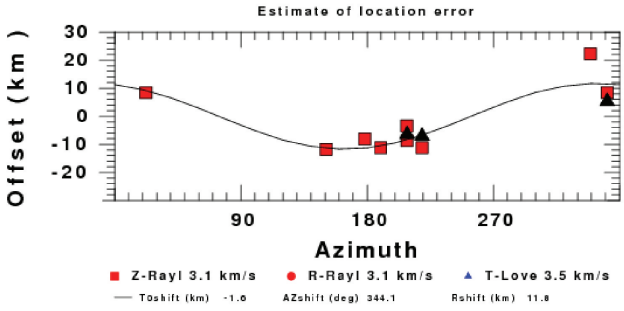

c) The time shifts for this inversion.

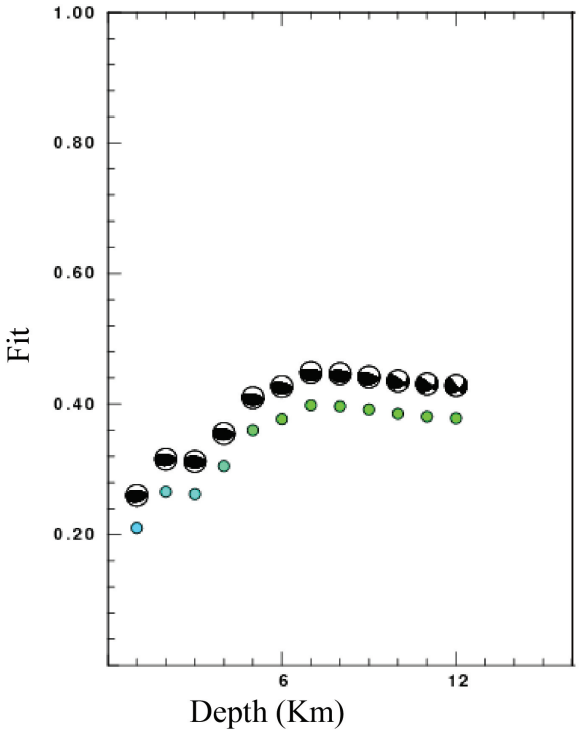

c) Depth sensivity for waveform mechanism

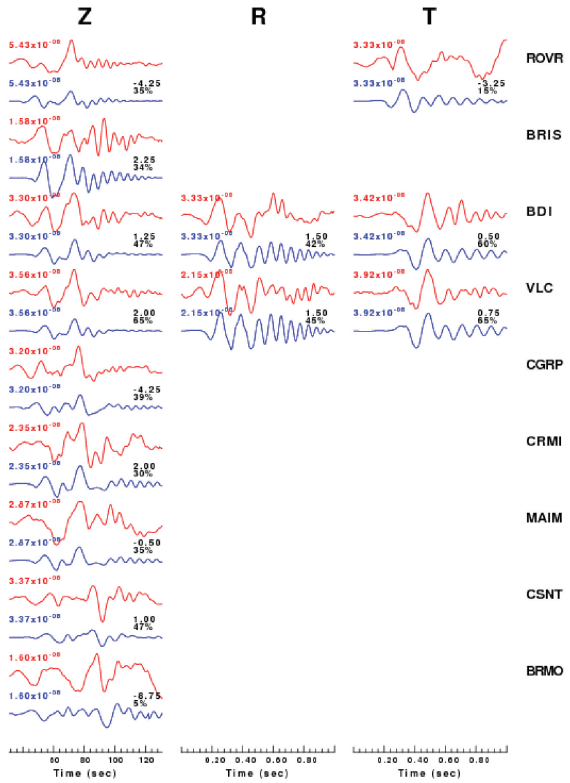

e) Comparison of the observed and predicted waveforms.

The event occurred on 2012/05/21 at 08:01:36.

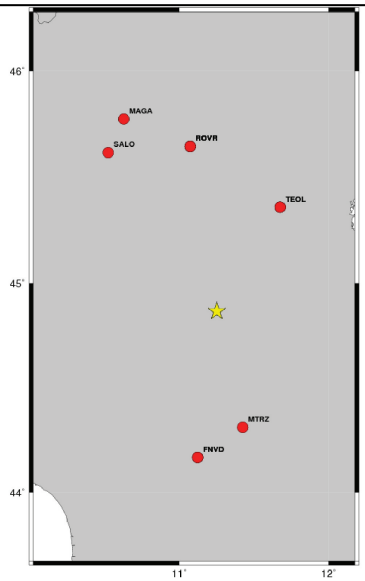

b) Location of broadband stations used for the waveform inversion.

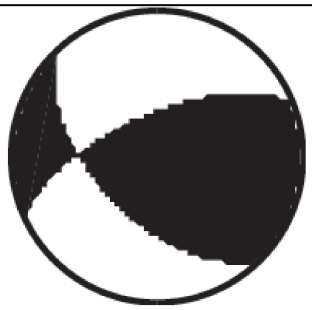

2012/05/21 18:02:26
44.847 11.259
Ml 3.60
Mw 3.28
Depth 11 Km
Strike 245
Dip 65
Rake 40
hp c 0.02 n 3
lp c 0.05 n 3

a) Waveform inversion focal mechanism.

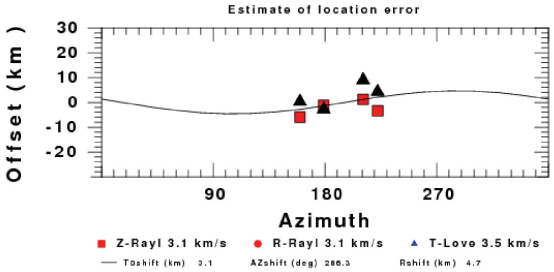

c) The time shifts for this inversion.

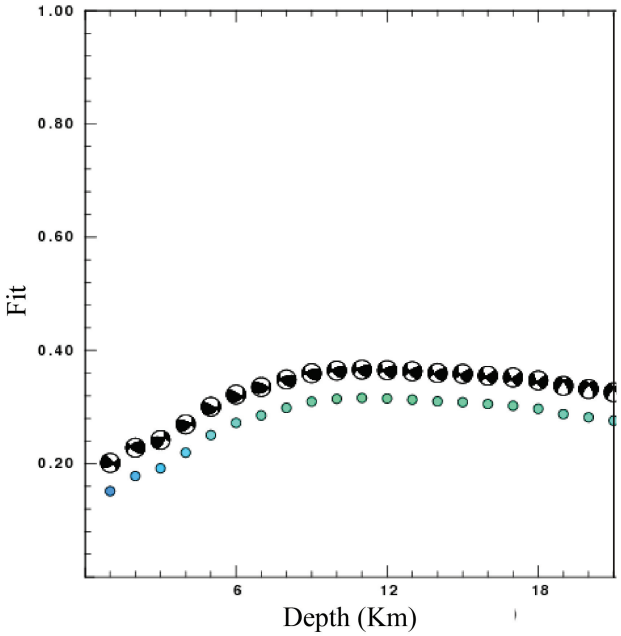

c) Depth sensivity for waveform mechanism

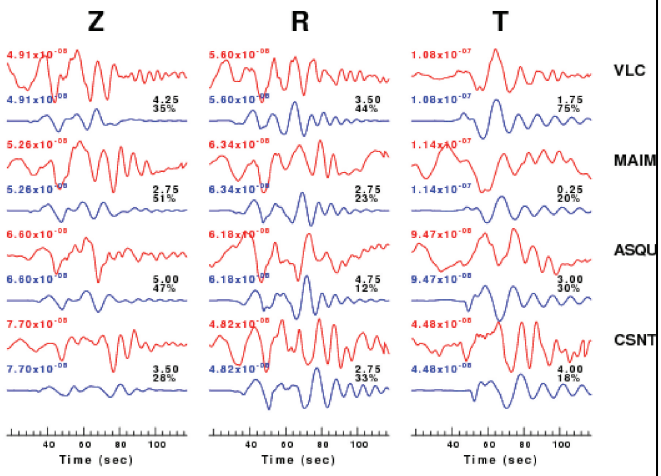

dicted waveforms.

The event occurred on 2012/05/21 at 18:02:26.

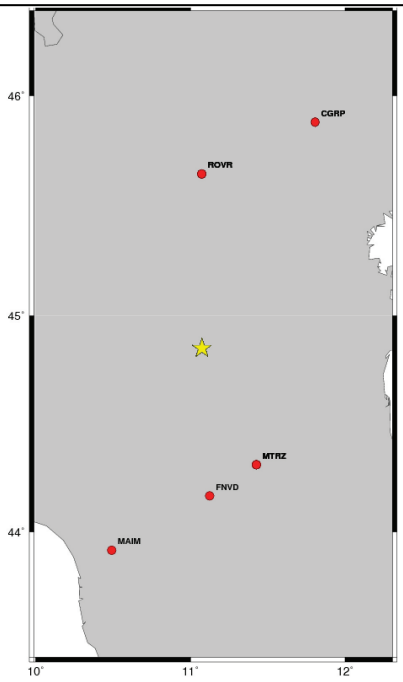

b) Location of broadband stations used for the waveform inversion.

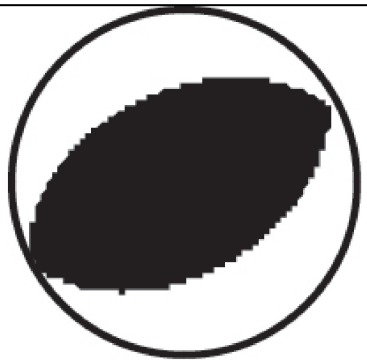

2012/05/22 06:11:15
44.850 11.074
Ml 3.70
Mw 3.57
Depth 5 Km
Strike 65
Dip 50
Rake 85
hp c 0.02 n 3
lp c 0.04 n 3

a) Waveform inversion focal mechanism.

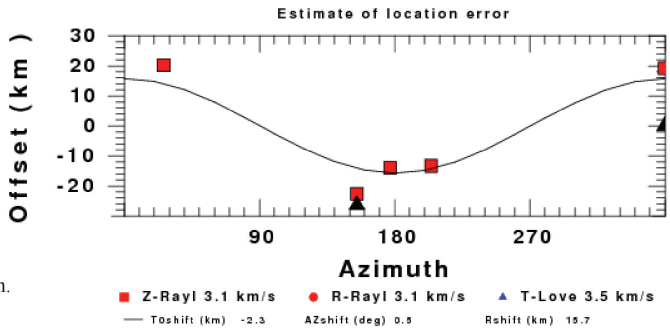

c) The time shifts for this inversion.

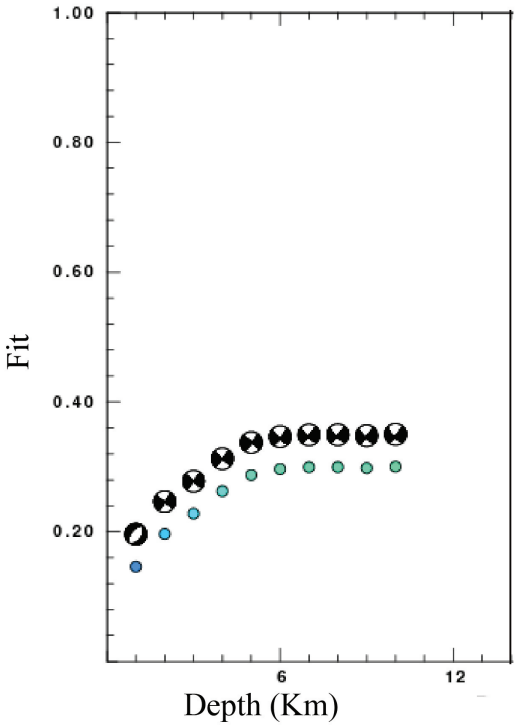

c) Depth sensivity for waveform mechanism

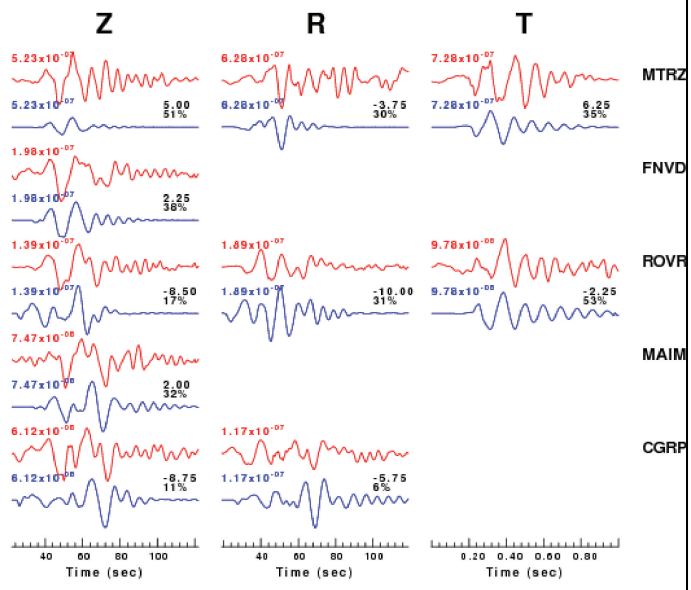

e) Comparison of the observed and predicted waveforms.

The event occurred on 2012/05/22 at 06:11:15.

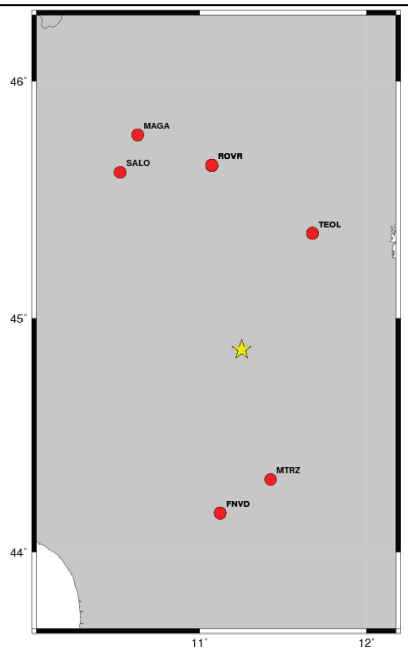

b) Location of broadband stations used for the waveform inversion.

2012/05/23 21:41:18
44.868 11.255
Ml 4.30
Mw 3.90
Depth 6 Km
Strike 275
Dip 45
Rake 90
hp c 0.02 n 3
lp c 0.04 n 3

a) Waveform inversion focal mechanism.

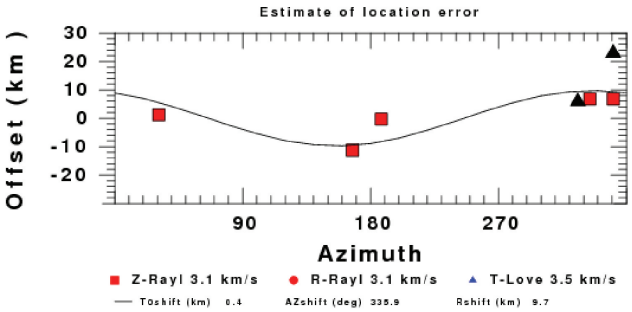

c) The time shifts for this inversion.

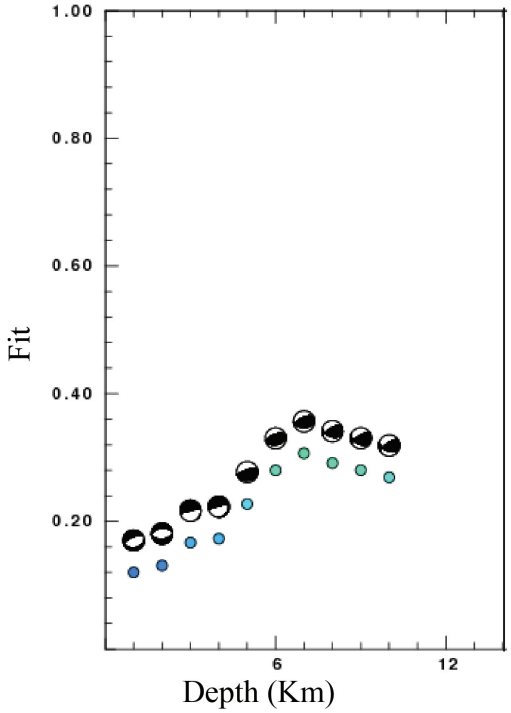

c) Depth sensivity for waveform mechanism

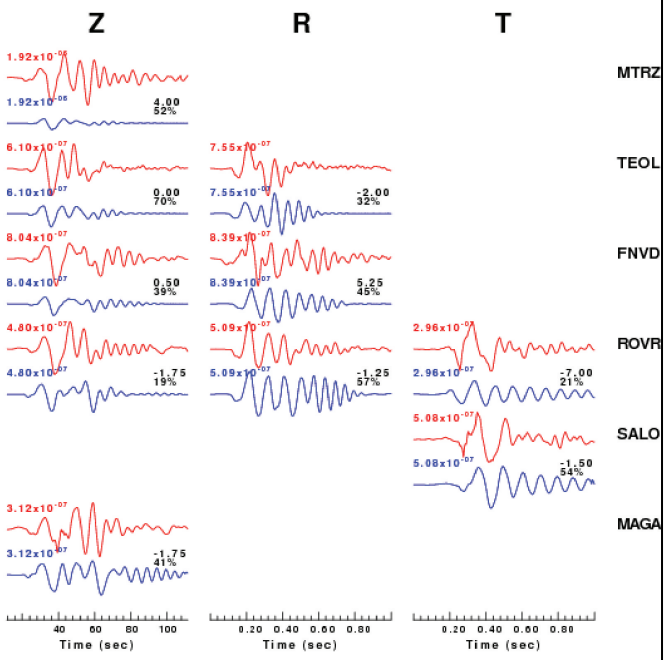

e) Comparison of the observed and predicted waveforms.

The event occurred on 2012/05/23 at 21:41:18.

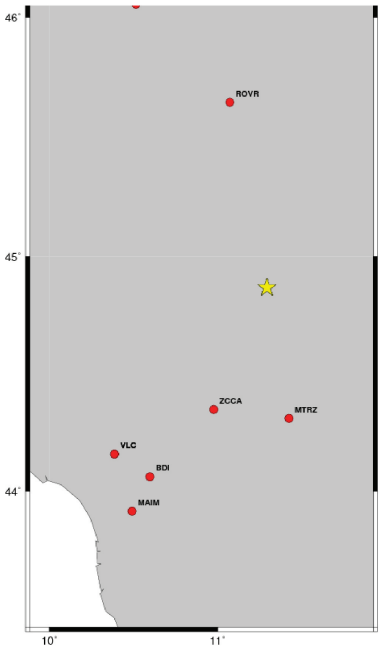

b) Location of broadband stations used for the waveform inversion.

2012/05/24 14:34:38
44.868 11.293
Ml 3.30
Mw 3.26
Depth 7 Km
Strike 297
Dip 61
Rake 99
hp c 0.02 n 3
lp c 0.04 n 3

a) Waveform inversion focal mechanism.

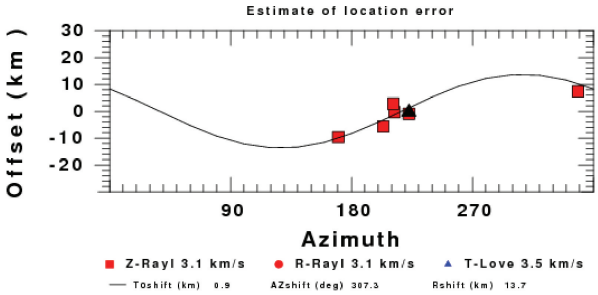

c) The time shifts for this inversion.

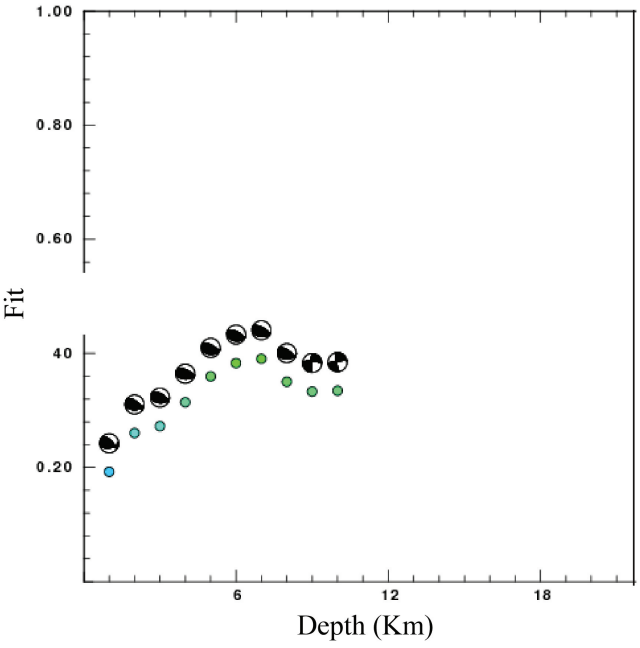

c) Depth sensivity for waveform mechanism

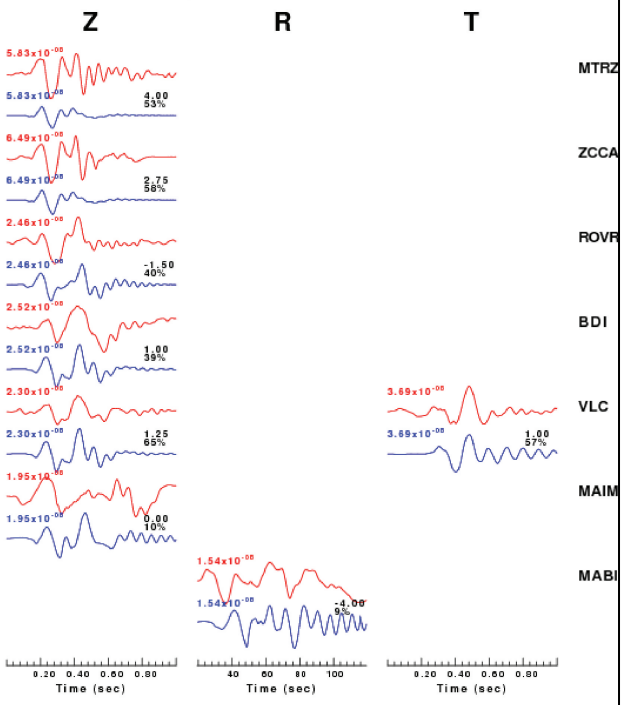

e) Comparison of the observed and predicted waveforms.

The event occurred on 2012/05/24 at 14:34:38.

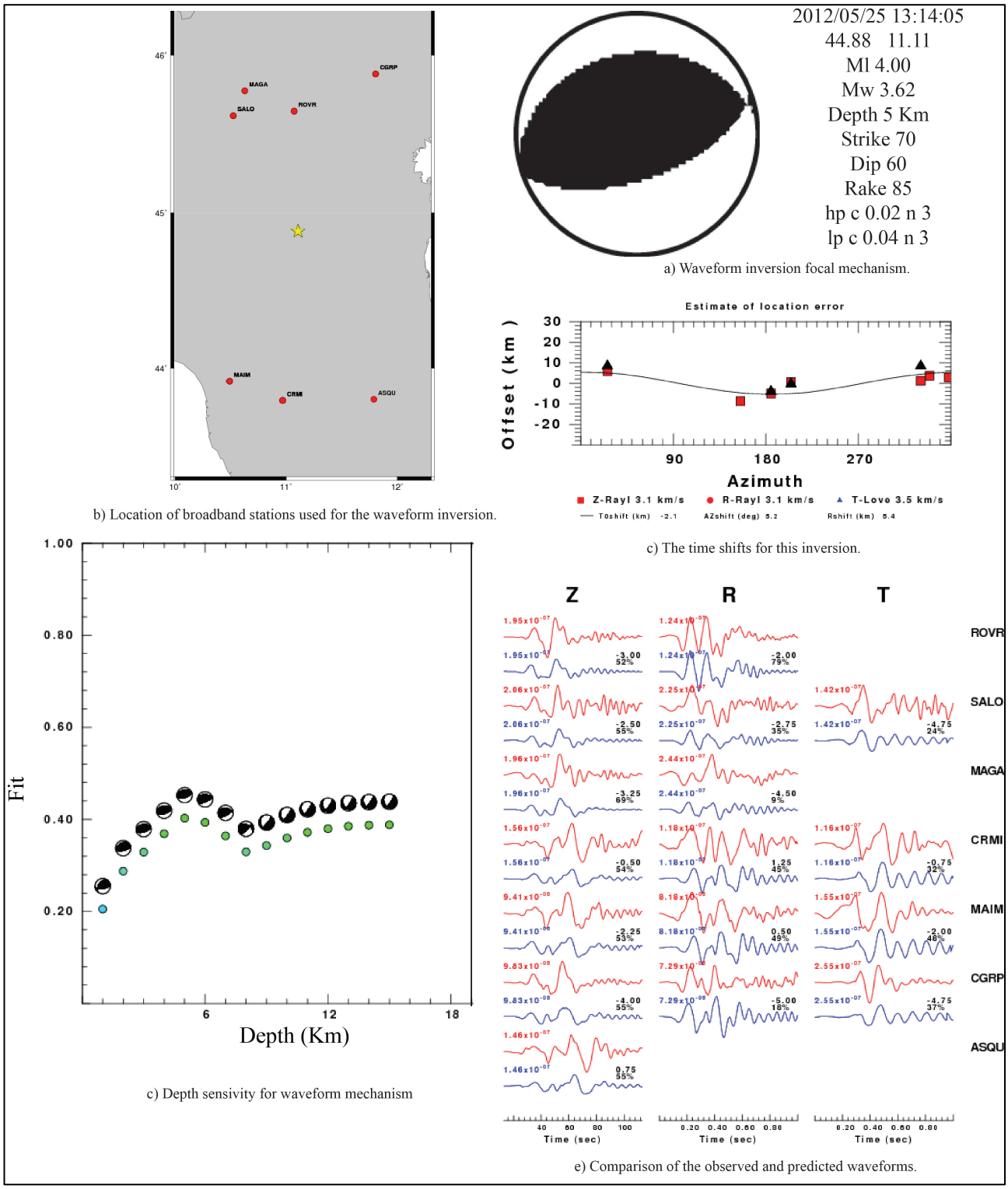

a) Waveform inversion focal mechanism.

b) Location of broadband stations used for the waveform inversion.

c) The time shifts for this inversion.

c) Depth sensivity for waveform mechanism

e) Comparison of the observed and predicted waveforms.

The event occurred on 2012/05/25 at 13:14:05.

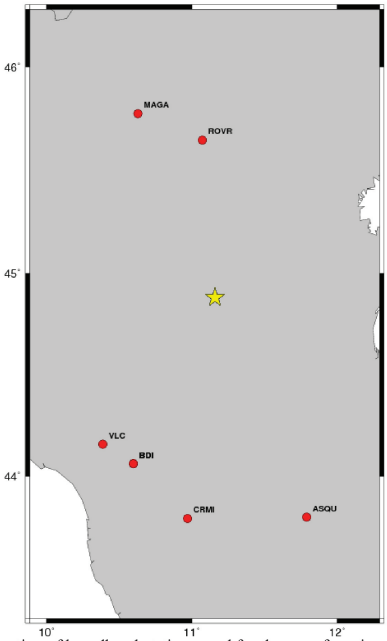

b) Location of broadband stations used for the waveform inversion.

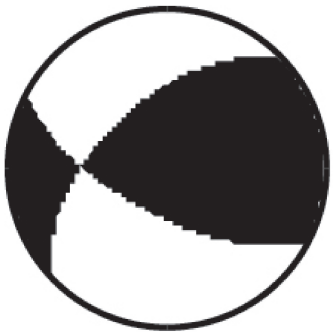

2012/05/27 18:18:45
44.882 11.158
Ml 4.00
Mw 3.85
Depth 11Km
Strike 201
Dip 60
Rake 145
hp c 0.02 n 3
lp c 0.04 n 3

a) Waveform inversion focal mechanism.

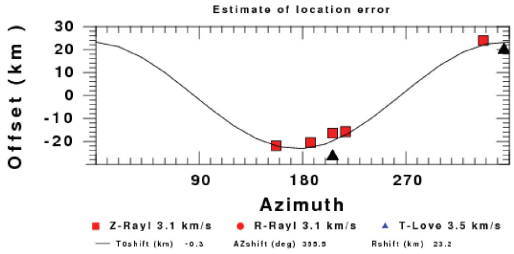

c) The time shifts for this inversion.

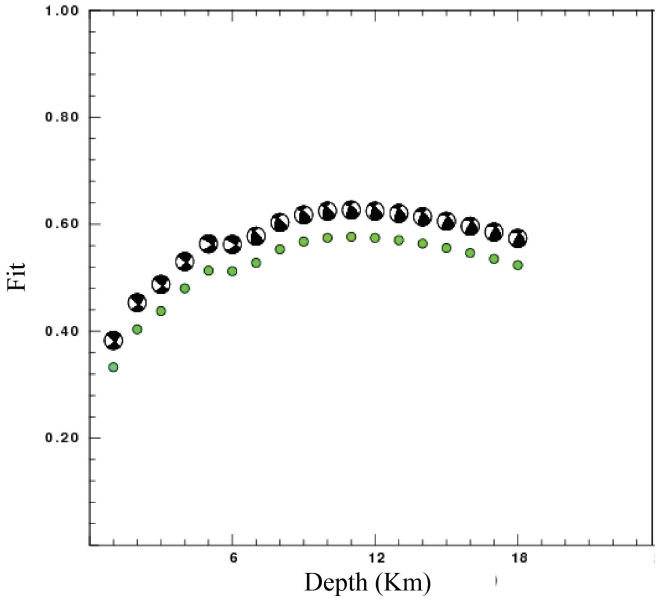

c) Depth sensivity for waveform mechanism

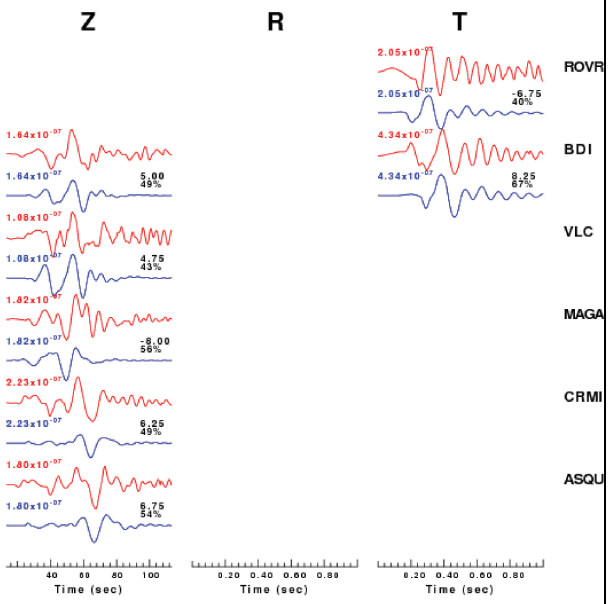

e) Comparison of the observed and predicted waveforms.

The event occurred on 2012/05/27 at 18:18:45.

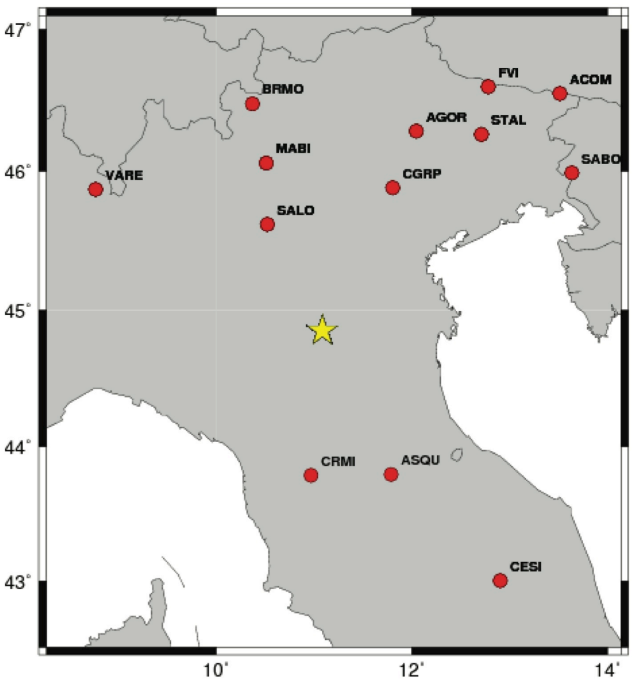

b) Location of broadband stations used for the waveform inversion.

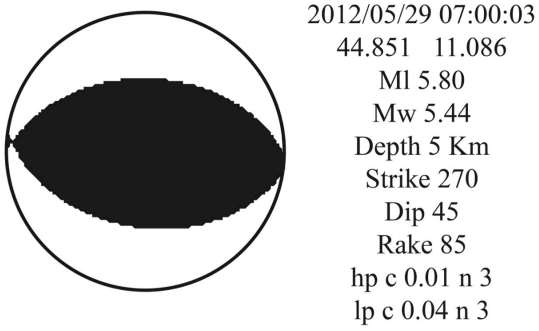

a) Waveform inversion focal mechanism.

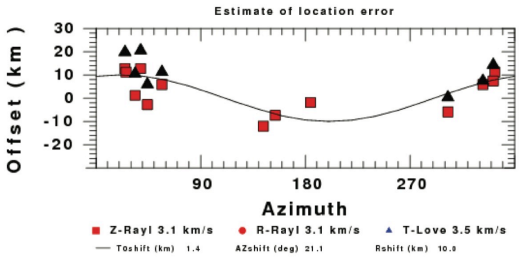

c) The time shifts for this inversion.

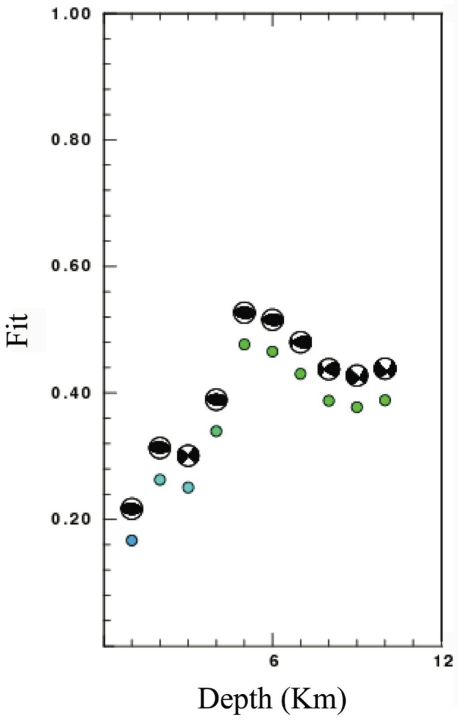

d) Depth sensivity for waveform mechanism

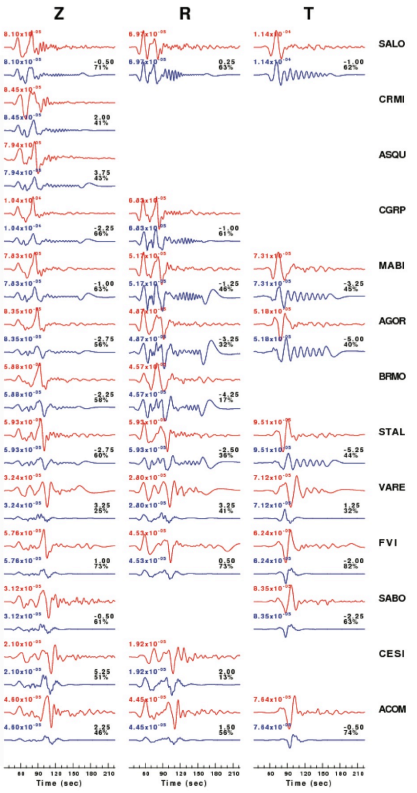

e) Comparison of the observed and predicted waveforms.

The event occurred on 2012/05/29 at 07:00:03.

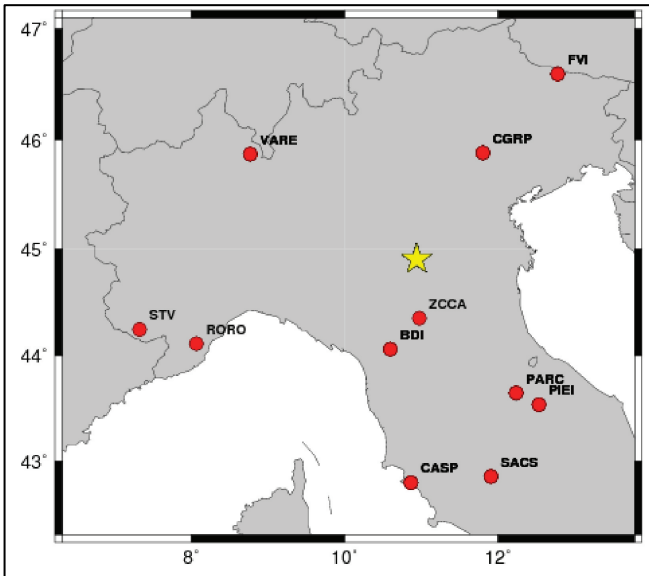

b) Location of broadband stations used for the waveform inversion.

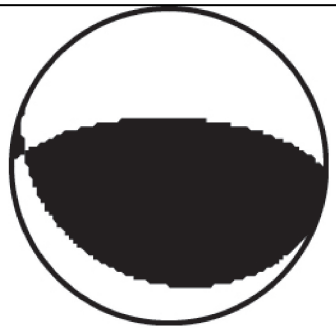

2012/05/29 08:25:51
44.901 10.943
Ml 4.50
Mw 4.34
Depth 7 Km
Strike 270
Dip 65
Rake 80
hp c 0.02 n 3
lp c 0.04 n 3

a) Waveform inversion focal mechanism.

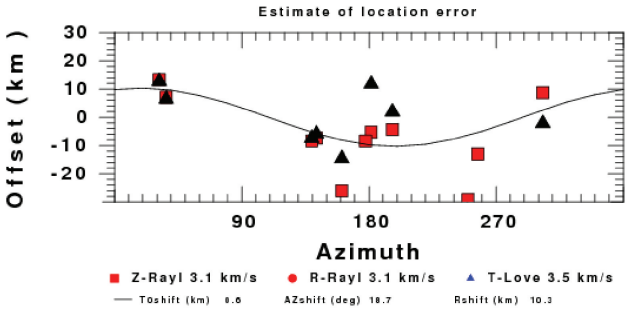

c) The time shifts for this inversion.

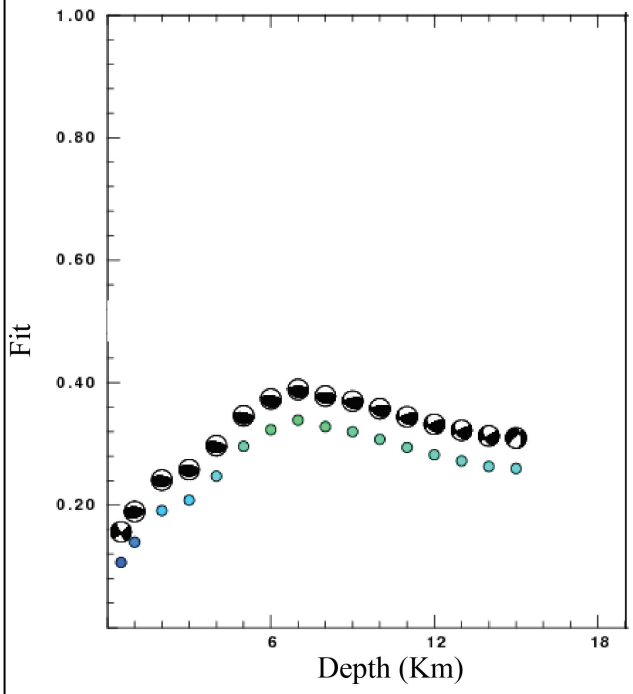

c) Depth sensivity for waveform mechanism

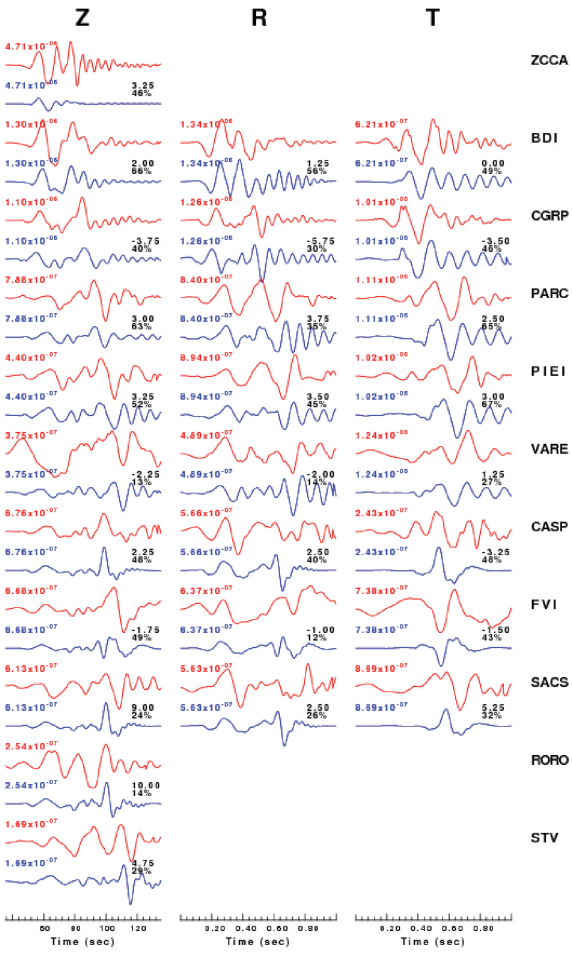

e) Comparison of the observed and predicted waveforms.

The event occurred on 2012/05/29 at 08:25:51.

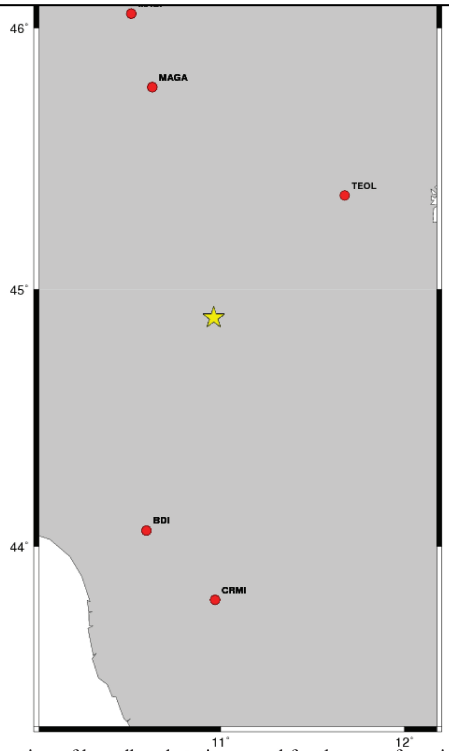

b) Location of broadband stations used for the waveform inversion.

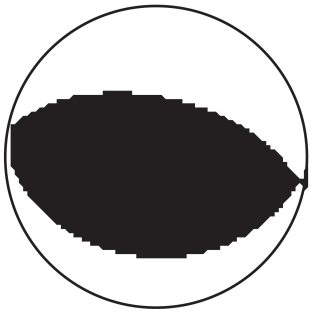

2012/05/29 08:40:58
44.892 10.962
Ml 4.20
Mw 3.98
Depth 7 Km
Strike 282
Dip 56
Rake 97
hp c 0.02 n 3
lp c 0.04 n 3

a) Waveform inversion focal mechanism.

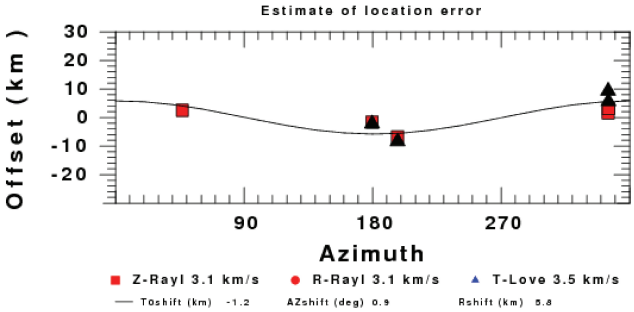

c) The time shifts for this inversion.

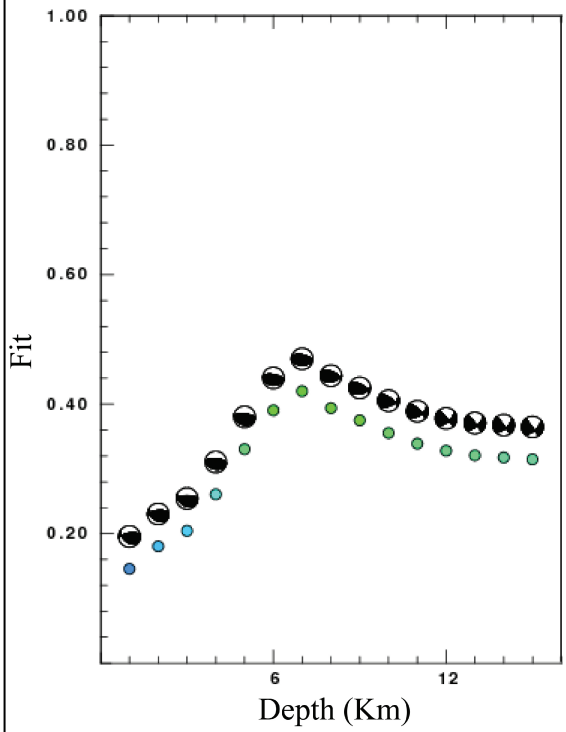

d) Depth sensivity for waveform mechanism

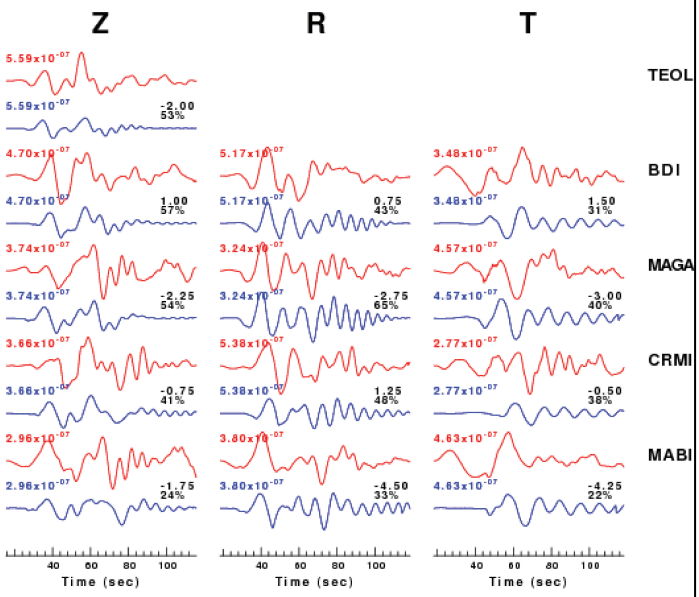

e) Comparison of the observed and predicted waveforms.

The event occurred on 2012/05/29 at 08:40:58.

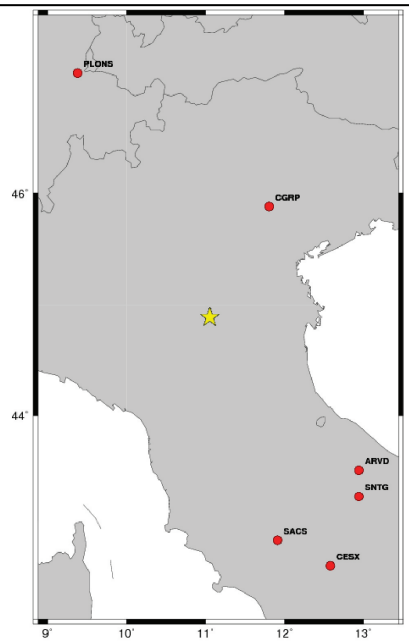

b) Location of broadband stations used for the waveform inversion.

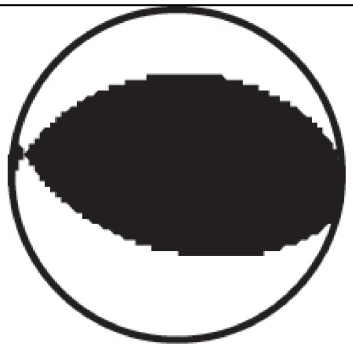

2012/05/29 09:30:21
44.892 11.053
Ml 4.20
Mw 3.69
Depth 5 Km
Strike 85
Dip 50
Rake 90
hp c 0.02 n 3
lp c 0.04 n 3

a) Waveform inversion focal mechanism.

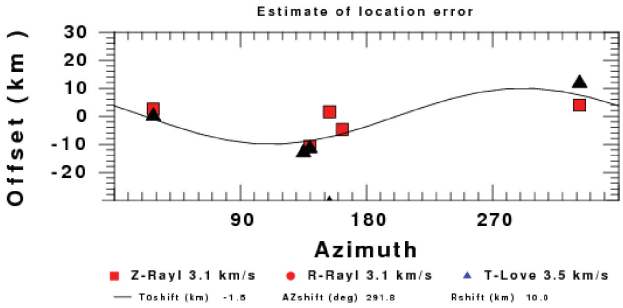

c) The time shifts for this inversion.

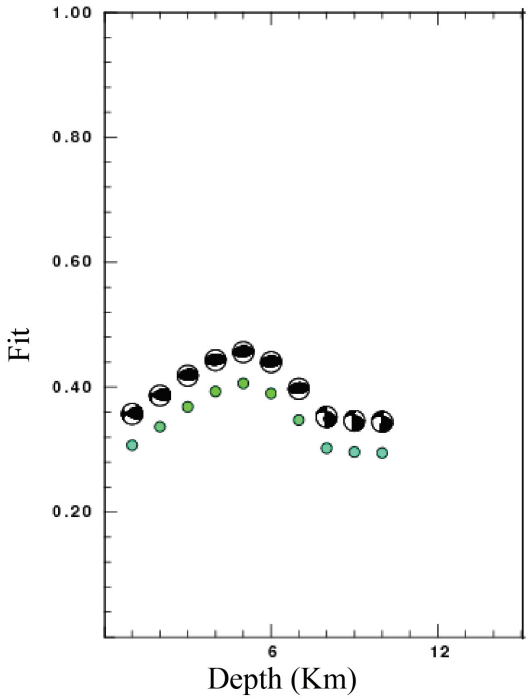

c) Depth sensivity for waveform mechanism

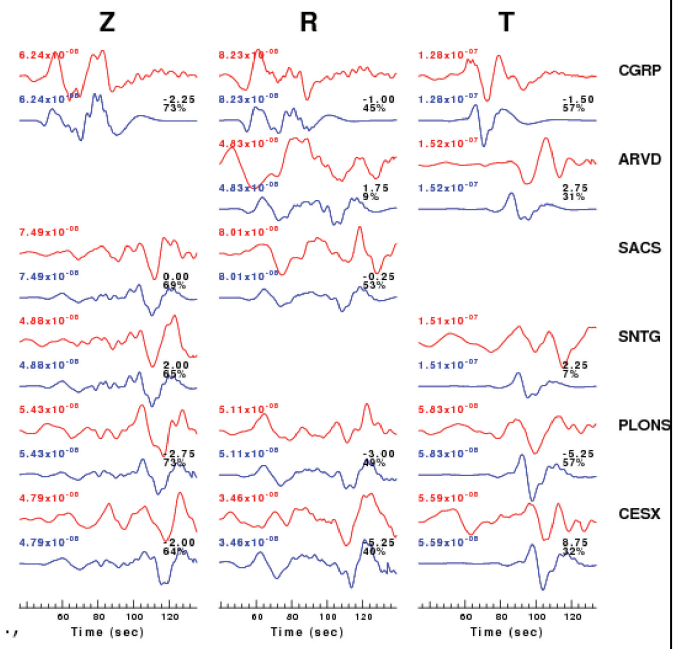

e) Comparison of the observed and predicted waveforms.

The event occurred on 2012/05/29 at 09:30:21.

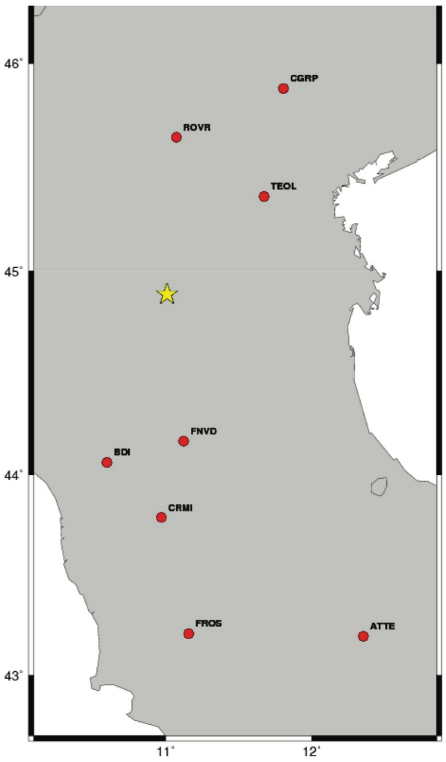

b) Location of broadband stations used for the waveform inversion.

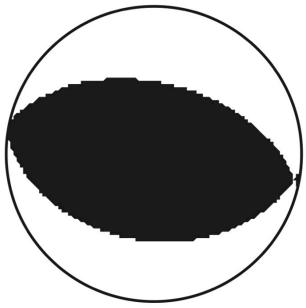

2012/05/29 10:55:57
44.888 11.008
Ml 5.30
Mw 5.10
Depth 6 Km
Strike 282
Dip 50
Rake 94
hp c 0.01 n 3
lp c 0.04 n 3

a) Waveform inversion focal mechanism.

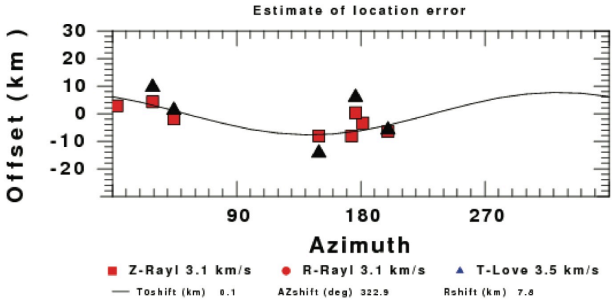

c) The time shifts for this inversion.

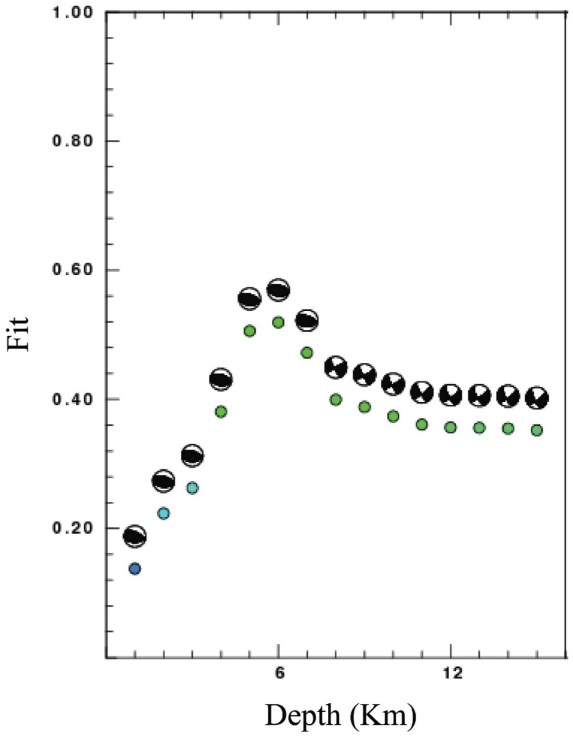

d) Depth sensivity for waveform mechanism

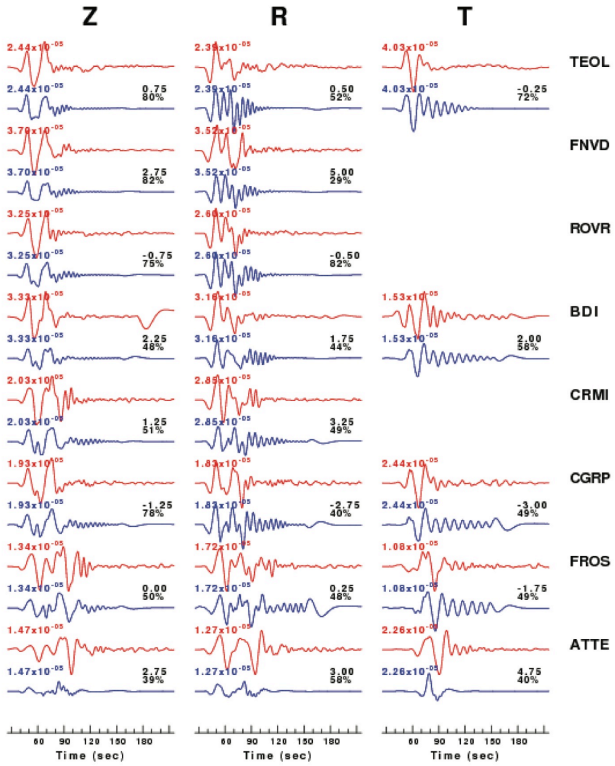

e) Comparison of the observed and predicted waveforms.

The event occurred on 2012/05/29 at 10:55:57.

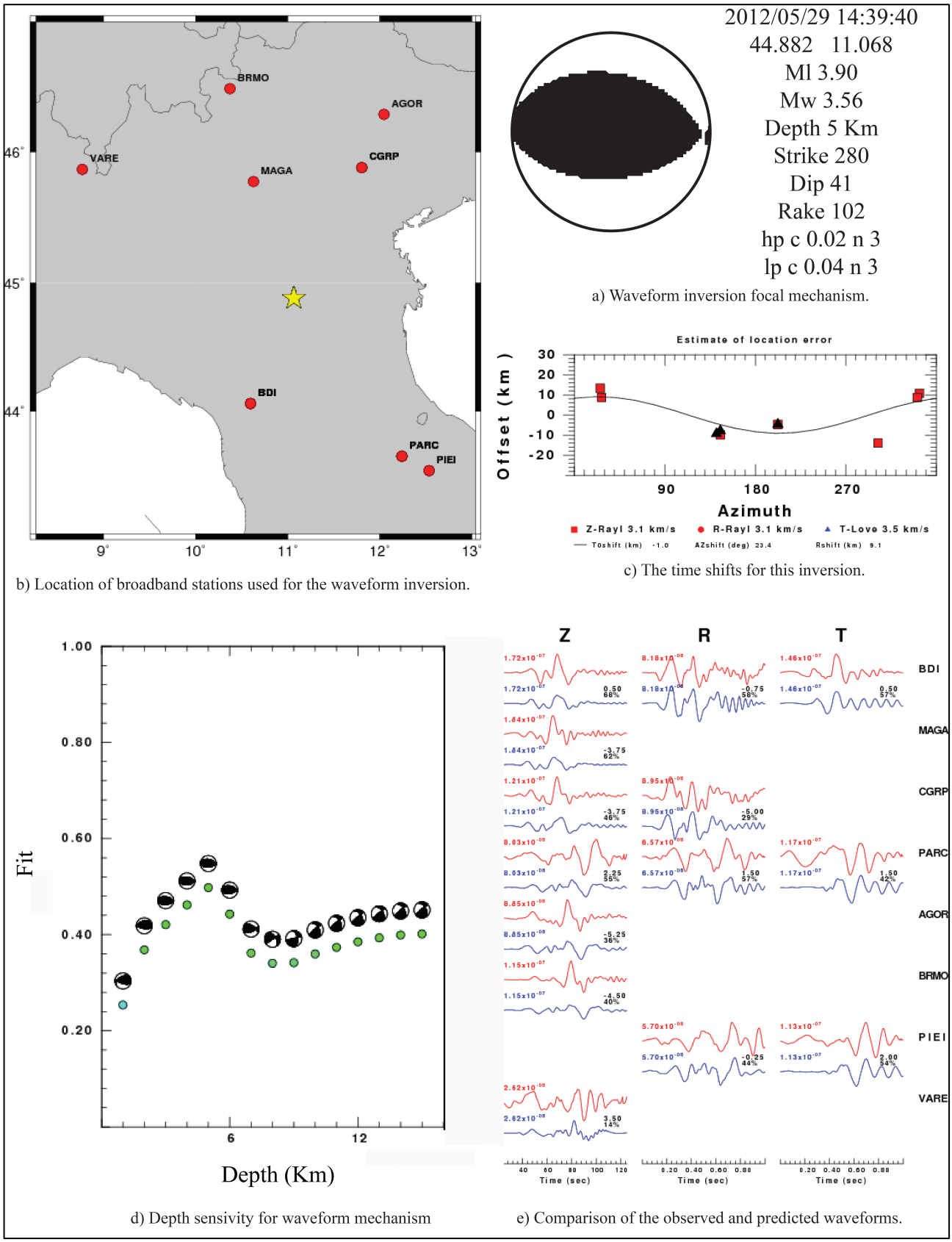

a) Waveform inversion focal mechanism.

b) Location of broadband stations used for the waveform inversion.

c) The time shifts for this inversion.

d) Depth sensivity for waveform mechanism

e) Comparison of the observed and predicted waveforms.

The event occurred on 2012/05/29 at 14:39:40.

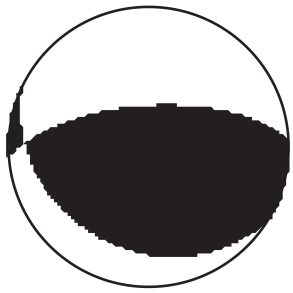

2012/06/03 19:20:43
44.899 10.943
Ml 5.10
Mw 4.61
Depth 10 Km
Strike 265
Dip 65
Rake 75
hp c 0.01 n 3
lp c 0.04 n 3

a) Waveform inversion focal mechanism.

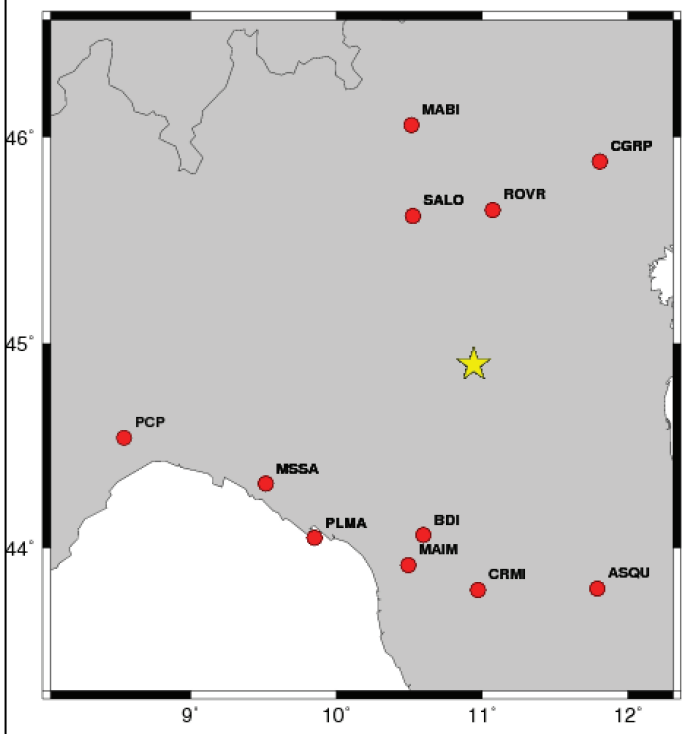

b) Location of broadband stations used for the waveform inversion.

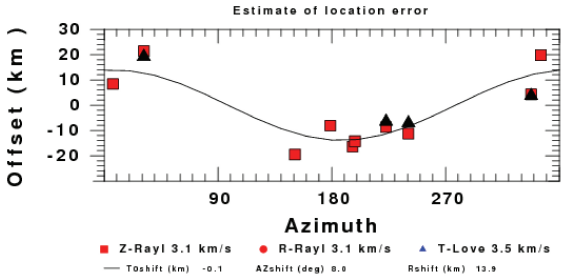

c) The time shifts for this inversion.

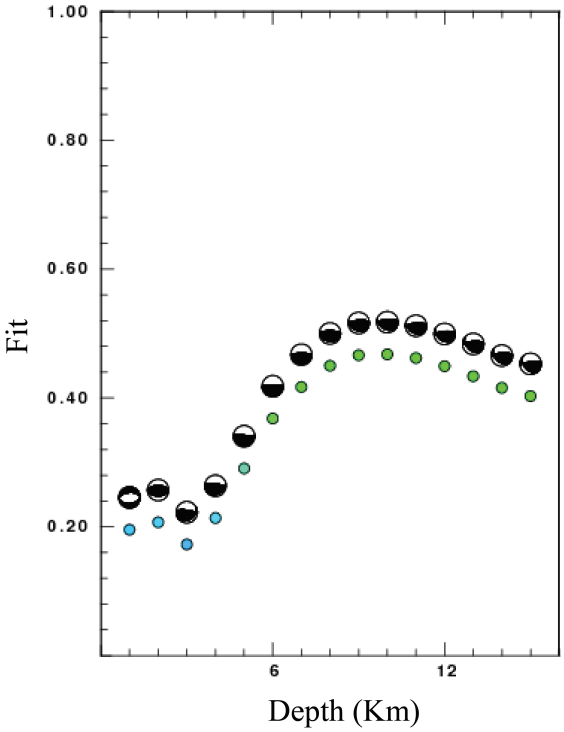

d) Depth sensivity for waveform mechanism

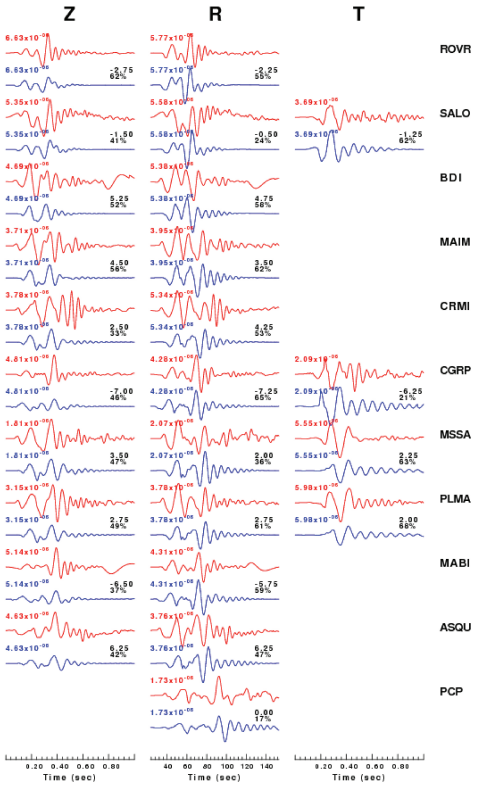

e) Comparison of the observed and predicted waveforms.

The event occurred on 2012/06/03 at 19:20:43.

Abe, K. (1975), Reliable estimation of the seismic moment of large earthquakes, *J. Phys. Earth*, 23, 381-390.

Abercrombie, R. E. (1995), Earthquake source scaling relationship from -1 to 5 M_L using seismogram recorded at 2.5 km depth, *J. Geophys. Res.*, 100, 24015-24036.

Abercrombie, R. E., and J. R. Rice (2005), Can observations of earthquake scaling constrain slip weakening?, *Geophys. J. Int.*, 162, 406-424.

Abercrombie, R. E., A. McGarr, G. Di Toro, and H. Kanamori (2006), Earthquakes: radiated energy and the physics of faulting, *Geophys. Mongr. Ser.*, 170, American Geophysical Union, Washington D. C.

Aki, K. (1966), Generation and propagation of G waves from the Niigata earthquake of June 16, 1965, Part ": Estimation of earthquake moment, released energy, and stress-stran drop from the G wave spectrum, *Bull. Earthq. Res. Inst.*, 44, 73-88.

Aki, K. (1967), Scaling relation of seismic spectrum, *J. Geophys. Res.*, 72, 1217-1231.

Aki, K., and P. G. Richards (1980), Quantitative Seismology, *W. H. Freeman & Co.*

Anderson, J. G., and S. E. Hough (1984), A model for the shape of the Fourier amplitude spectrum of acceleration at high frequencies, *Bull. Seism. Soc. Am.*, 74, 1969-1993.

Anderson, J. G., and Y. Lei (1994), Non-parametric description of peak acceleration as a function of magnitude, distance and site in Guerrero, Mexico, *Bull. Seism. Soc. Am.*, 84, 1003-1017.

Bay, F., D. Fah, L. Malagnini, and D. Giardini (2003), Spectral shear-wave ground motion scaling for Switzerland, *Bull. Seism. Soc. Am.*, 93, 414-429.

Baltay, A., G. Prieto, and G. C. Beroza (2010), Radiated seismic energy from coda measurements and no scaling in apparent stress with seismic moment, *J. Geophys. Res.*, 115, B08314, doi:10.1029/2009JB006736.

Berkhemer, H. (1962), Die Ausdehnung der Bruchii che im Erdbebenherd und ihr Einfluss auf das seismische Wellenspektrum, *Gerland's Beitr. Geophys.*, 71, 5-26.

Boatwright, J. (1980), A spectral theory for circular seismic sources; simple estimates of source dimension, dynamic stress drop, and radiated seismic energy, *Bull. Seism. Soc. Am.*, 70, 1-27.

Boore, D. M. (1983), Stochastic simulation of high-frequency ground motion based on seismological models of the radiated spectra, *Bull. Seism. Soc. Am.*, 73, 1865-1894.

Boore, D. M. (2003), Simulation of ground motion using the stochastic method, *Pure Appl. Geophys.*, 160, 635-676.

Boore, D. M., and W. B. Joyner (1984), A note on the use of random vibration theory to predict peak amplitudes of transient signals, *Bull. Seism. Soc Am.*, 74, 2035-2039.

Brune, J. N. (1970), Tectonic stress and the spectra of seismic shear waves from earthquake, *J. Geophys. Res.*, 75, 4997-5009.

Brune, J. N. (1971), Correction to tectonic stress and the spectra of seismic shear waves from earthquakes, *J. Geophys. Res.*, 76, 5002.

Bürgmann, R., D. Schmidt, R. M. Nadeau, M. d'Alessio, E. Fielding, D. Manaker, T. V. McEvilly, and M. H. Murray (2000), Earthquake potential along the northern Hayward fault, California, *Science*, 289, 1178-1182.

Bürgmann, R., K. H. Chen, R. M. Nadeau, T. Chen, and N. Lapusta (2009), Triggering effect of 2004 M 6 Parkfield event on earthquake cycle of small repeating events, *EOS Trans. AGU*, 90, Fall Meeting Suppl., Abstract S51C-1446.

Burridge, R., and L. Knopoff (1964), Body force equivalents for seismic dislocations, *Bull. Seism. Soc. Am.*, 54, 1875-1878.

Carminati, E., D. Scrocca, and C. Doglioni (2010), Compaction-induced stress variations with depth in an active anticline: Northern Apennines, Italy, *J. Geophys. Res.*, 115, B02401, doi:10.1029/2009JB006395.

Chen, H., and R. Rau (2003), Fault slip rates from repeating microearthquakes on the Chihshang fault, eastern Taiwan, *EOS Trans. AGU*, 84 (46), Fall Meet. Suppl., Abstract T11F-06.

Chen, K. H., R. Bürgmann, R. M. Nadeau, T. Chen, and N. Lapusta (2010), Postseismic variations in seismic moment and recurrence interval of repeating earthquakes, *Earth Plan. Science Lett.*, 299, 118-125.

Chung, W. Y., and H. Kanamori (1980), Variation of seismic source parameters and stress drops within a descending slab and its implications in plate mechanics, *Phys. Earth Planet. Interiors*, 23, 134-159.

Consiglio Nazionale delle Ricerche (1992), Structural model of Italy and gravity map, scale 1:500000, in Progetto Finalizzato Geodinamica, *Quad. Ric. Sci.*, vol. 114, 1 pp., Rome.

Dziewonski, A. M., and D. Anderson (1981), Preliminary reference Earth model, *Phys. Earth Planet. Interiors*, 25, 297-356.

Del Pezzo, E., F. Bianco, S. Marzorati, P. Augliera, E. D'Alema, and M. Massa (2011), Depth-dependent intrinsic and scattering seismic attenuation in north central Italy, *Geophys. J. Int.*, 186, 373–381, doi:10.1111/ j.1365-246X.2011.05053.x.

Dolce, M., M. Nicoletti, A. Ammirati, R. Bianconi, L. Filippi, A. Gorini, S. Marcucci, F. Palma, and E. Zambonelli (2012), The Emilia thrust earthquake of 20 May 2012 (northern Italy): Strong motion and geological observations, *Rep. 1, Dip. Della Prot. Civ., Rome*. [Available at http://www.protezionecivile. gov.it/resources/cms/documents/Report_DPC_1_Emilia_EQSd.pdf.]

Dománski, B. and S. J. Gibowicz (2008), Comparison of source parameters estimated on the frequency and time domains for seismic events at Rudna copper mine, Poland, *Acta Geophys.*, 56, 324–343, doi:10.2478/s11600-008-0014-1.

Doornbos, D. J. (1988), Multiple scattering by topographic relief with application to the core-mantle boundary, *Geophys. Journ.*, 92, 465–478.

Dreger, D., R. M. Nadeau, and A. Chung (2007), Repeating earthquake finite source models: strong asperities revealed on the San Andreas Fault, *Geophys. Res. Letts.*, 34, L23302, doi:10.1029/2007GL031353.

Duda, S. J. (1978), Physical significance of the earthquake magnitude the present state of interpretation of the concept, *Tectonophysics*, 49, 119–130.

Dufumier, H. (1996), On the limits of linear moment-tensor inversion of teleseismic body wave spectra , *Pageoph*, 147.

EMERGEO Working Group (2012), Technologies and new approaches used by the INGV EMERGEO Working Group for real-time data sourcing and processing during the Emilia Romagna (northern Italy) 2012 earthquake sequence, *Annals of Geophysics*, 55(4) doi: 10.4401/ag-6117.

Ellsworth, W. L. (1995), Characteristic earthquakes and long-term earthquake forecasts: Implications for central California seismicity, in Urban Disaster Mitigation: The role of science and Technology, edit by F. Y. Cheng and M. S. Sheu, 1-14, Elsevier Sci., New York.

Eshelby, J. D. (1957), The determination of the elastic field of an ellipsoidal inclusion and related problems, *Proc. R. Soc. London*, 241, 376-396.

European Committee for Standardization (2003), Eurocode 8: Design of structures for earthquake resistance part 1: General rules, seismic actions and rules for buildings, draft 6, Doc. CEN/TC250/SC8/N335, Brussels.

Fantoni, R., and R. Franciosi (2010), Tectono-sedimentary setting of the Po Plain and Adriatic foreland, *Rend. Fis. Accad. Lincei*, 21, suppl. 1, 197–209, doi:10.1007/s12210-010-0102-4.

Frankel, A., and H. Kanamori (1983), Determination of rupture duration and stress drop for earthquakes in Southern California, *Bull. Seism. Soc. Am.*, 73 (6), 1527–1551.

Frankel, A., J. Fletcher, F. Vernon, L. Haar, J. Burger, T. Hanks, and J. Brune (1986), Rupture characteristics and tomographic source imaging of M_L 3 earthquakes near Anza, Southern California, *J. Geophys. Res.*, 91, 12633–12650.

Frohlich, C. (1995), Characteristics of well-determinated non-double-couple earthquakes in the Harvard CMT catalog, *Phys. Earth Planet. Int.*, 91, 213–228.

García, D., S. K. Singh, M. Herráiz, J. F. Pacheco, and M. Ordaz (2004), Inslab earthquakes of central Mexico: Q, Source Spectra, and Stress Drop, *Bull. Seism. Soc. Am*., 94, 789-802.

Geller, R. J. (1976), Scaling relations for earthquake source parameters and magnitudes, *Bull. Seism. Soc. Am*., 66 (5), 1501-1523.

Gephart, J. W., D. W. Forsyth (1984), An improved method for determining the regional stress tensor using earthquake focal mechanism data: Application to the San Fernando earthquake sequence, *J. Geopysic. Res*., 89, 9305-9320.

Gutenberg, B., C. F. Richter (1956c), Earthquake magnitude, intensity, energy, and acceleration, *Bull. Seism. Soc. Am*., 46 (5), 105-145.

Hanks, T., and R. McGuire (1981), The character of high-frequency strong ground motion. *Bull. Seism. Soc. Am*., 71, 2071-2095.

Harmsen, S. (1979), Estimating the diminution of shear-wave amplitude with distance: application to the Los Angeles, California, urban area. *Bull. Seism. Soc. Am*., 87, 888-903.

Hartzell, S. H. (1978), Earthquake aftershock as Green's function, *Geophys. Res. Lett.*, 5, 1-4.

Haskell, N. A. (1964), Total energy and energy spectral density of elastic wave radiation form propagationg faults, *Bull. Seism. Soc. Am.*, 54, 1811-1841.

Herrmann, R. B., H. Benz, and C. J. Ammon (2011a), Monitoring the Earthquake source process in North America*, Bull. Seism. Soc. Am.,* 101, 2609-2625, doi: 10.1785/0120110095.

Herrmann, R. B., L. Malagnini, and I. Munafò (2011), Regional moment tensors of the 2009 L'Aquila earthquake sequence, *Bull. Seismol. Soc. Am*., 101, 975–993, doi:10.1785/0120100184.

Hough, S. E. (1997), Empirical Green's function analysis: Taking the next step, *J. Geophys. Res*., 102, 5369–5384.

Hutchings, L., and F. T. Wu (1990), Empirical Green's functions from small earthquakes – A waveform study of locally recorded aftershocks of the San Fernando earthquake, *J. Geophys. Res.*, 95, 1187–1214.

Ide, S., G. C. Beroza, S. G. Prejean, and W. L. Ellworth (2003), Apparent break in earthquake scaling due to path and site effects on deep borehole recordings, *J. Geophys. Res.*, 108 (B5), 2271, doi:10.1029/2001JB001617.

Ide, S., and G. C. Beroza (2001), Does apparent stress vary with earthquake size?, *Geophys. Res. Lett.*, 28, 3349-3352.

Igarashi, T., T. Matsuzawa, and A. Hasegawa (2003), Repeating earthquakes and interpolate aseismic slip in the northeastern Japan subduction zone, *J. Geophys. Res.*, 108 (B5), 2249, doi:10.1029/2002JB001920.

Izutani, Y. (2005), Radiated energy from the mid Niigata, Japan, earthquake of October 23, 2004, and its aftershocks, *Geophys. Res. Lett.*, 108 32, L21313, doi:10.1029/2005GL024116.

Jeon, Y. S, and R. B. Herrmann (2004), High-frequency ground-motion scaling in Utah and Yellostone*, Bull. Seism. Soc. Am.*, 94, 1644-1657.

Jost, M. L, and R. B. Herrmann (1989), A student's Guide to and review of moment tensors*, Bull. Seism. Soc. Am.*, 60, 37-57.

Kanamori, H. (1977), The energy release in great earthquakes, *J. Geophys. Res.*, 82, 2981-2987.

Kanamori, H., and D. Anderson (1975), Theoretical basis of some empirical relations in seismology, *Bull. Seism. Soc. Am.*, 65, 1073-1095.

Keiles-Borok, V. (1959), An estimation of the displacement in an earthquake source and of source dimensions, *Ann. Geofis. (Rome)*, 12, 205-214.

Kennett, B. L. N. (1988), Seismic velocity field estimation - strategies for a large-scale nonlinear inverse problem, *Exploration Geophys.*, 19, 297-298.

Kravanja, S., G. F. Panza, and J. Sileny (1999), Robust retrieval of a seismic point-source time function, *Geophys. J. Int.*, 136, 385-394.

Kuge, K., and H. Kawakatsu (1990), Analysis of a deep "non double couple" earthquake using very broadband data, *Geophys. Res. Lett.*, 17, 227-230.

Lay, T., and T. C. Wallace (1995), Modern global seismology, *Academic press.*

Lienert, B. R., E. Berg, and L. N. Frazer (1986), Hypocenter: AN earthquake location method using centered, scaled, and adaptively least squares, *Bull. Seism. Soc. Am*., 76, 771-783.

Li, Y. And C. H. Thurber (1988), Source properties of two microearthquakes at Kilauea volcano, Hawaii, *Bull. Seism. Soc. Am.,* 78 (3), 1123-1132.

Li, Y. G., J. E. Vidale, and S. E. Cochran (2004), Low-velocity damaged structure on the San Andreas fault at Parkfield from fault-zone trapped waves, *Geophys. Res. Lett.,* 31, L12S06, 1-5.

Madariaga, R. (1976), Dynamics of an expanding circular fault, *Bull. Seism. Soc. Am.,* 65, 163-182.

Madariaga, R. (1978), The dynamic field of Haskell's rectangular dislocation fault model, *Bull. Seism. Soc. Am.,* 68 (4), 869-887.

Malagnini, L. (1999), Ground motion scaling in Italy and Germany*, Ph.D Dissertation,* Saint Louis University, Saint Louis, Missouri.

Malagnini, L., R. B. Herrmann, and M. Di Bona (2000a), Ground motion scaling in the Apennines (Italy)*, Bull. Seism. Soc. Am.,*90, 1062-1081.

Malagnini, L., R. B. Herrmann, and K. Koch (2000b), Ground motion scaling in Central Europe*, Bull. Seism. Soc. Am*.,90, 1052-1061.

Malagnini, L., A. Akinci, R. B. Herrmann, N. A. Pino, and L. Scognamiglio (2002), Characteristics of the ground motion in northeastern Italy, *Bull. Seism. Soc. Am*., 92, 2186- 2204.

Malagnini, L., K. Mayeda, R. Uhrhammer, A. Akinci, and R. B. Herrmann (2007), A regional ground-motion excitation/attenuation model for the San Francisco region, *Bull. Seism. Soc. Am*., 97, 843- 862, doi:10.1785/0120060101.

Mayeda, K., L. Malagnini, and W. R. Walter (2007), A new spectral ratio method using narrow band coda envelopes: Evidence for non-self-similarity in the Hector Mine sequence, *Geophys. Res. Lett.*, 34, L11303, doi:10.1029/2007GL030041.

Mayeda, K., and L. Malagnini (2010), Source radiation invariant property of local and near-regional shear-wave coda: Application to source scaling for the M_w 5.9 Wells, Nevada sequence, *Geophys. Res. Lett.*, 37, L07306, doi:10.1029/2009GL042148.

McGuire, R. K., A. M. Becker, and N. C. Donovan (1984), Spectral estimates of seismic shear waves, *Bull. Seism. Soc. Am*., 74, 1427- 1440.

Montaldo, V., E. Faccioli, G. Zonno, A. Akinci, and L. Malagnini (2005), Treatment of ground-motion predictive relationships for the reference seismic hazard map of Italy, *J. Seismol*., 9, 295–316, doi:10.1007/ s10950-005-5966-x.

Morasca, P., L. Malagnini, A. Akinci, D. Spallarossa, and R. B. Herrmann (2006), Ground motion scaling in the Western Alps*, J. Seismol*., 10, 315-333.

Mori, J., R. E. Abercrombie, and H. Kanamori (2003), Stress drops and radiated energies of aftershocks of the 1994 Northridge, California, earthquake, *J. Geophys. Res*., 108 (B11), 2545, doi:10.1029/2001JB000474.

Mueller, C. (1985), Source pulse enhancement by deconvolution of an empirical Green's function, *Geophys. Res. Lett.*, 12, 33-36.

Nadeau, R. M., and L. R. Johnson (1988), Seismological studies at Parkfield VI: moment release rates and estimates of source parameters for small repeating earthquakes, *Bull. Seismol. Soc. Am.*, 88, 790-814.

Nadeau, R. M., W. Foxall, and T. V. McEvilly (1995), Clustering and periodic recurrence of microearthquakes on the San Andreas Fault at Parkfield, California, *Science*, 267, 503-507.

Nadeau, R. M., and T. V. McEvilly (1999), Fault slip rates at depth from recurrence intervals of repeating microearthquakes, *Science*, 285, 718-721.

Nadeau, R. M., and T. V. McEvilly (2004), Periodic pulsing of characteristic microearthquakes on the San Andreas fault, *Science*, 303, 220-222.

O'Neill, M. E. (1984), Source dimensions and stress drops of small earthquakes near Parkfield, California, *Bull. Seism. Soc. Am.*, 71, 27-40.

O'Neill, M. E., and J. H. Healy (1973), Determination of source parameters of small earthquakes from P-wave rise time, *Bull. Seism. Soc. Am.*, 63 (2), 599-614.

Park, J., C. Lindburg, and F. L. Vernon (1987), Multitaper spectral analysis of high-frequency seismograms, *J. Geophys. Res.*, 92, 12675-12684.

Pearce, R. G., and R. C. Stewart (1989), Interpretation of seismic pulse duration in terms of a propagationg rupture: a method and case histories, *Tectonophysics*, 166 (1-3), 115-132.

Pieri, M., and G. Groppi (1975), The structure of the base of the Pliocene-Quaternary sequence in the subsurface of the Po and Veneto Plains, the Pedeapennine Basin and the Adriatic Sea, *Quad. Ric. Sci.*, 90, 409–415.

Prieto, G. A., P. M. Shearer, F. L. Vernon, and D. Kilb (2004), Earthquake source scaling and self-similarity estimation from stacking P and S spectra, *J. Geophys. Res.*, 109, B08310, doi:10.1029/2004JB003084.

Prieto, G. A., D. J. Thomson, F. L. Vernon, P. M. Shearer, and R. L. Parker (2007), Confidence intervals for earthquake source parameters, *Geophys. J. Int.*, 168, 1227-1234.

Prieto, G. A., R. Parker, and F. L. Vernon (2009), A fortran 90 library for multitaper spectrum analysis, *Comput. Geosci.*, 35, 1701-1710.

Purcaru, G., and H. Berckhemer (1978), A magnitude scale for very large earthquake, *Tectonophysics*, 49, 189-198.

Raoof, M., R. B. Herrmann, and L. Malagnini (1999), Attenuation and excitation of three-component ground motion in Southern California, *Bull. Seism. Soc. Am.*, 89, 888–902.

Radulian, M., and M. Popa (1996), Relative methods to set out the seismic source parameters, *Rev. Roum. Geophysique*, 37, 29–40.

Reches, Z. (1987), Determination of the tectonic stress tensor from slip along that obey the Coulomb yield condition, *Tectonics*, 6, 849–861.

Richter, C. F. (1935), An instrumental earthquake magnitude scale, *Bull. Seism. Soc. Am.*, 25, 1–32.

Richter, C. F. (1958), Elementary Seismology, *W. H. Freemen & Co., San Francisco*.

Ripperger, J., and P. M. Mai (2004), Fast computation of static stress changes on 2Dfault from final slip distributions, *Geophys. Res. Lett.*, 31(18), L18610, doi:10.1029/2004GL020594.

Rivera, L. (1989), Inversion du tenseur des contraintes et des mecanismes au foyer a partir des donnees de polatites pour une population de seismes. Application a l'etude du foyer de sismicite intermediaire de Bucaramanga (Colombie), *These de doctorat, Univ. Strasbourg, France.*

Rubinstein, J. L., and W. L. Ellsworth (2009), Precise estimation of repeating earthquake moment: example from Parkfield, California, *Bull. Seism. Soc. Am.*, 100, 1952–1961, doi:10.1785/0120100007.

Sato, T., and T. Hirasawa (1973), Body wave spectra from propagationg shear cracks, *J. Phys. Earth,* 21, 415-431.

Savage, J. C. (1966), Radiation from realistic model of faulting, *Bull. Seism. Soc. Am.,* 56, 577-592.

Scognamiglio, L., L. Malagnini, and A. Akinci (2005), Ground Motion scaling in Eastern Sicily (Italy)*, Bull. Seism. Soc. Am*., 95, 568-578.

Scrocca, D., E. Carminati, C. Doglioni, and D. Marcantoni (2007), Slab retreat and active shortening along the central-northern Apennines, in Thrust Belts and Foreland Basins: From Fold Kinematics to Hydrocarbon Systems, *Frontiers in Earth Sciences*, edited by O. Lacombe et al., pp. 471–487, Springer, Berlin, doi:10.1007/978-3-540-69426-7_25.

Shearer, P. M. (1999), Introduction to Seismology, Cambridge: *Cambridge University Press*.

Sileny, J., G. F. Panza, and P. Campus (1992), Waveform inversion for point source moment tensor retrieval with variable hypocentral depth and structural model, *Geophys. J. Int.,* 109, 259-274.

Sileny, J., and I. Psencik (1995), Mechanisms of local earthquakes in 3-D inhomogeneous media determined by waveform inversion, *Geophys. J. Int.,* 121, 459-474.

Sileny, J., P. Campus, and G. F. Panza (1996), Seismic moment tensor resolution by waveform inversion of a few local noisy records-I. Synthetic tests, *Geophys. J. Int.,* 126, 605-619.

Silva, W. J., N. Abrahamson, G. Toro, and C. Costantino (1997), Description and validation of the stochastic ground motion model, Final Report, *Brookhaven National Laboratory*, Inc. Upton, New York.

Steketee, J. A. (1958), Volterra's dislocations in a semi-infinite medium, *Can. D. Phys.*, 36, 192-205.

Stucchi, M., C. Meletti, V. Montaldo, H. Crowley, G. M. Calvi, and E. Boschi (2011), Seismic hazard assessment (2003–2009) for the Italian building code, *Bull. Seismol. Soc. Am.*, 101(4), 1885–1911, doi:10.1785/ 0120100130.

Taira T., P. G. Silver, F. Niu, and R. M. Nadeau (2009), Remote triggering of fault-strength changes on the San Andreas fault at Parkfield, *Nature*, 461, doi:10.1038/nature08395.

Thomson, D. J. (1982), Spectrum estimation and harmonic analysis, *Proc. IEEE*, 70, 1055–1096.

Thurber, C., H. J. Zhang, F. Waldhauser, J. Hardebeck, A. Michael, and D. Ederhart-Phillips (2006), Three-dimensional compressional wavespeed model, earthquake relocations, and focal mechanisms for the Parkfield, California, region, *Bull. Seismol. Soc. Amer.*, 96(4), S38-S39.

Tibi, R., C. H. Estabrook, G. Bock (1999), The 17 June 1996 Flores Sea and 9 March 1994 Tonga-Fiji earthquakes: source processes and deep earthquake mechanisms, *Geophys. J. Int.*, 138, 625-642.

Tucker, B. E., and J. N. Brune (1973), Seismograms, S-wave spectra and source parameters for aftershocks of the San Fernando earthquake; in San Fernando, California earthquake of February 9, 1971, *NOAA Special Report*.

Udias , A. (1999), Principles of Seismology, *Cambridge University Press.*

Uchide, T., and S. Ide (2010), Scaling of earthquake rupture growth in the Parkfield area: self-similar growth and suppression by the finite seismogenic layer*, J. Geophys. Res.*, 115, B11302, doi:10.1029/2009JB007122.

Vidale, J. E., W. L. Ellsworth, A. Cole, and C. Marone (1994), Variations in rupture process with recurrence interval in a repeated small earthquake, *Nature*, 368, 624–626.

Yadz, M. R. S. (1993), Ground motion studies in the Southern Great Basin of Nevada and California*, Ph.D. Thesis*, Saint Louis University.

Yoo, S. H., J. Rhie, H.-S. Choi, and K. Mayeda (2010), Evidence for non-self-similarity and transitional increment of scaled energy in the 2005 west off Fukuoka seismic sequence, *J. Geophys. Res.*, 115, B08308, doi:10.1029/2009JB007169.

Yoo, S. H., J. Rhie, H. S. Choi, and K. Mayeda (2011), Coda-derived source parameters of earthquakes and their scaling relationship in the Korean Peninsula, *Bull. Seismol. Soc. Am*., 101, 2388–2398, doi:10.1785/0120100318.

Yoo, S. H., and K. Mayeda (2012), Validation of Non-Self-Similar Source Scaling using ground motions from the 2008 Wells, Nevada, Earthquake Sequence, *Bull. Seismol. Soc. Am*., 103, 2508–2519, doi:10.1785/ 0120120327.

Zoback, M. L. (1992), Firts- and second-order patterns of stress in the lithosphere: The world stress map project*, J. Geophys. Res.,* 97, 11703-11728.

The key to Random Vibration Theory (RVT) analysis is the prediction of peak time domain motions from the Fourier Amplitude Spectrum (FAS) representation of the motion and its duration. Parseval's theorem and extreme value statistics (EVS) are used to relate the ground motion in the frequency domain to the peak motion in the time domain. EVS was first used in seismology by Hanks and McGuire (1981) to predict peak ground acceleration (PGA) from the *rms* (root-mean-square) acceleration, a_{rms}. Parseval's theorem is used to compute a_{rms} from the FAS, and a RVT-derived factor is used to relate a_{rms} to the peak ground acceleration.

Before application to earthquake motions, let us consider any time history $x(t)$ with its associated FAS, $X(f)$. The *rms* value of the signal (x_{rms}) is a measure of its average value over a given time period, T_{rms}, and it is computed from the integral of the time series over that time period using:

$$x_{rms} = \sqrt{\frac{1}{T_{rms}} \int_0^{T_{rms}} \left[x(t)\right]^2 dt} \tag{1}$$

Parseval's theorem relates the integral of a time series to the integral of its Fourier Transform, such that Equation (1) can be re-written in terms of the FAS of the signal:

$$x_{rms} = \sqrt{\frac{2}{T_{rms}} \int_0^{\infty} \left|X(f)\right|^2 df} = \sqrt{\frac{m_0}{T_{rms}}} \tag{2}$$

where m_o is defined as the zero-th moment of the FAS. The n-th moment of the FAS is defined as:

$$m_n = 2\int_0^{\infty} (2\pi f)^n \left|X(f)\right|^2 df \tag{3}$$

The peak factor *(PF)* represents the ratio of the maximum value of a signal (x_{max}) to its *rms* value (x_{rms}), such that if x_{rms} and PF are known, then x_{max} can be computed using:

$$x_{\max} = PF \cdot x_{rms} \tag{4}$$

Based on the description of Parseval's Theorem and EVS above, the following information is required to compute the peak time domain value of a signal (x_{max}):

• Fourier Amplitude Spectrum, $X(f)$

• Ground motion duration, T_{rms}

RVT and Ground Motion Simulation

Random vibration theory was first used in seismology by Hanks and McGuire (1981) to predict peak ground acceleration (PGA) from the *rms* acceleration, a_{rms}. This work was followed by the landmark papers of Boore (1983) and McGuire et al. (1984) that demonstrated the power of RVT to predict various ground motions parameters (PGA, peak ground velocity, spectral acceleration). These works generally use the Brune (1970, 1971) omega-squared (ω^2) point source spectrum to describe the FAS of earthquake motions and single-degree-of-freedom oscillator transfer functions are applied to this FAS to describe spectral accelerations and spectral velocities. Boore (1983) compared peak estimates of ground motion from RVT with values computed from time domain simulations and showed that spectral values developed by RVT compared well with median values from the time domain simulations. McGuire et al. (1984) compared RVT-predicted spectral velocities with those from recorded motions from the 1971 San Fernando (Mw = 6.6) earthquake. The RVT-simulated spectral velocities agreed well with the recorded data. The work by McGuire et al. (1984) is considered a milestone paper because it provided the most convincing evidence that RVT could be coupled with a seismological source spectrum to develop estimates of earthquake ground motions consistent with observations, despite the various RVT assumptions violated by earthquake ground motions (e.g., non-stationary, non-Gaussian, etc.). The application of RVT to ground motion simulation has evolved since the early 1980's, as summarized in Silva et al. (1997) and Boore (2003). These studies have considered the appropriate descriptions of the FAS of motion (e.g., point source vs. finite source, single corner frequency vs. multiple corner frequency) and the appropriate values of ground motion durations.

Ground Motion Duration and Characteristics of Bandpass filters

Each band-pass filters consists of a lowpass 8-pole Butterworth filter with corner frequency at $\left(f_0/\sqrt{2}\right)$ Hz, followed by a 8-pole highpass Butterworth filter with corner frequency at $\sqrt{2}f_0$ Hz.

The filtered seismograms is squared and integrated, starting from the onset of the S-waves. At the time when the integral reaches a plateau, the integrated energy is normalized to unit value. The duration of the significant part of the seismograms, T, relative to the central frequency, f_0, is then defined as the time window bracketing the 5% - 75% of the integrated energy. Duration is referred to the portion of the time series that follows the S-wave onset.

RVT Equations

Given the *rms* value of a windowed random time history, its peak value is a function of the number of maxima present in the time window (Cartwright and Longuet-Higgins, 1956). Using the Parseval's theorem, we can obtain the *rms* value of a windowed time function from its squared spectral amplitude. If the time series is characterized by a dominant frequency (i.e., if the signal is filtered in a narrow frequency band centrered at a particular frequency f_0), the number of peaks in the time history, N, is two times the duration T times the central frequency:

$$N = 2f_0T \tag{5}$$

Cartwright and Longuet-Higgins (1956) demonstrated that:

$$a_{peak} = \eta_{\max} a_{rms} \tag{6}$$

where:

$$\eta_{\max} = \int_{-\infty}^{+\infty} \eta \frac{d}{d\eta}\left[1-q(\eta)\right]^N d\eta \tag{7}$$

$q(\eta)$ is the cumulative probability of η exceeding a given value; $\eta_{\max}$ is the expected peak value for the time history. In general, *N* depends on the spectral moments, as well as does the probability distribution of the peaks:

$$p(\eta) = \frac{d}{d\eta}\left[1 - q(\eta)\right]^N \tag{8}$$

The *k*-th spectral moment can be written as:

$$m_k = \frac{1}{\pi}\int_0^\infty \omega^k \left|A(\omega)\right|^2 d\omega \tag{9}$$

The spectral moments can also be used to estimate the dominant frequency of a time history and consequently *N*, the number of extrema (Cartwright and Longuet-Higgins, 1956):

$$f_0 = \frac{1}{2\pi}\left(m_4 / m_2\right)^{\frac{1}{2}} \tag{10}$$

$$N = 2T\frac{1}{2\pi}\left(m_4 / m_2\right)^{\frac{1}{2}} \tag{11}$$

Also, note that:

$$a_{rms} = \left(\frac{m_0}{T}\right)^{\frac{1}{2}} \tag{12}$$